Climate Response to a Variable Gravity-Wave Source

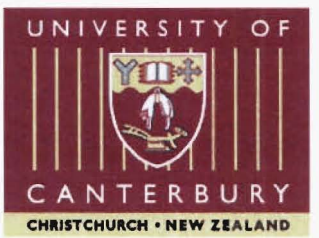

A Thesis Submitted in Partial Fulfilment
of the Requirements for the Degree of
Doctor of Philosophy in Physics
at the University of Canterbury

Scott M. Osprey

2002

Acknowledgements

I would first wish to thank my friend and supervisor Bryan Lawrence for his guidance and perseverance throughout the course of this thesis, without whom I am convinced I would still be labouring over little bits of badly coloured paper, in between organising social events for friends. While I am at it, I would also like to thank Dr's Darlene Heuff and Don Grainger for their role in supervising me, albeit briefly, over the last year or so.

Many thanks must also go to Sam Dean for the many hours of mindless tomfoolery he and I have had to endure in the office. Also to all the other office mates; Mohar Chattopadhyay, Jelena Ajtic, Trevor Carey-Smith, John Grant and in the early days Adam Dunford. To other graduates, friends and colleagues in the Department; Mike Hyslop, Andreas Wurl, Gareth Thomas and Juern Schmelzer, thanks especially to you. Without whom I would have completed this thing ages ago. To Tim Woodward, Stu Dunford, Steve Van Grunsven and Andy Falconer, I hope you fair better without me in indoor cricket.

On matters of science, I appreciate all the input (and code) from Alexander Medvedev and Chris Warner, without whom I would still be grinding away putting pen to paper

I am also grateful for assistance from the University of Canterbury in helping to support me over these years and the Marsden Fund and Royal Society of New Zealand, for help in funding a couple of 'trips' over to Oxford and Nice. Also, to the Rutherford Appleton Laboratory for kindly allowing me to use their resources while madly trying to finish up.

Finally, I give special thanks to my family, who have supported me through all the good times and bad.

Abstract

An investigation examining the response of numerical models containing one of several gravity wave parameterisations to changes in a prescribed tropospheric gravity wave source has been completed.

It has been found that the unique interaction between orographic waves and those comprising a broad spectrum, exhibit tell-tale features in an offline environment. The response to these from within the confines of a mechanistic computer model persist and show a significant effect about the southern winter stratosphere.

Offline comparisons of the three parameterisations has highlighted significant differences between two of the schemes (Doppler Spread Parameterisation, Medvedev and Klaassen) and the Ultra-Simple Spectral Parameterisation. These are due to; (1) the way in which the latter models wave dissipation and (2) the makeup of the source used. These cannot be resolved by an adjustment of tunable parameters. Comparisons inside a mechanistic model indicate the shortcomings of these offline analyses, as those schemes which showed little difference previously, now differed significantly.

The modelled climatic response to changes in the boundary source of gravity waves was largely predictable; warmer/cooler winter/summer polar mesosphere with a reduction in the stratospheric wind jets during times of solstice. These were attributable to circulation changes caused by differing amounts of mesospheric wave drag. However, the extent of the sensitivity of the southern hemisphere winter circulation was unexpected. Other dynamical differences seen included changes in resolved large-scale wave propagation, which in turn affected the nature of sudden warmings and the onset of final warmings.

The modulation of a source of vertically propagating gravity waves by stationary planetary scale winds was seen to force similarly sized planetary scale winds within the mesosphere. The modulation of this tropospheric source of gravity waves appears linked with the Tibetan Low during the Asian monsoon season. Similar anomalous winds have been seen in observations and just such a mechanism has been proposed to help explain the existence of these. This has been the first study where such a result has been forced without the introduction of a contrived signal in the source below.

Contents

Figures

Chapter 1

Introduction

In recent years, much has been learned about the atmosphere from the increase in number and sophistication of atmospheric instruments - satellites (namely UARS (Upper Atmosphere Research Satellite), airborne and ground based lidars, balloons and atmospheric radars (e.g. Birdlings Flat[1]). Data retrieved from these have helped to give insight into the nature of a number of atmospheric phenomena.

However, even though the atmospheric sciences have recently seen unprecedented coverage of the atmosphere, there still remain large gaps in our knowledge from regions not covered adequately by either land or 'air-borne' instrumentation. Also, the resolution of the data gathered is often too course in either temporal or spatial extent. Land-based radars, for example, are generally excellent in their temporal resolution, however are restricted to a localised geographic location. Satellites have (generally) an extensive area of coverage, but suffer due to data from different locations being taken at different times. Such effects generally require complicated assimilation techniques to interpolate the information to a common time (*Swinbank and O'Neill* (1994)). Also, due to matters of expense, the resolution of these instruments usually means that processes occurring at comparatively small scales (e.g. gravity-waves) are difficult, if not impossible, to detect (directly) at present over a large coverage area. However, gravity-waves are routinely detected using localised, line-of-sight equipment at low heights and have been recently detected at higher levels using satellite data (*Fetzer and Gille* (1996); *Wu and Waters* (1996a,b)).

Issues of resolution arise in the running of large-scale global climate models too. As these models are only privy to processes which occur at scales greater to their grid point spacing[2] or highest order Fourier truncations, processes such as small scale gravity-waves have to be parameterised. That is, instead of solving in time a set of differential equations, basic sub-scale physics must be invoked to predict the atmospheric response to the influence of these processes (using parameters which have already been found using more conventional methods e.g. temperature and wind fields).

Problems such as these - data which is too coarse to extract suitable information and models which operate at scales which cannot resolve processes on a smaller scale, have

[1] a variety of ground-based radars run by the University of Canterbury, Christchurch, New Zealand

[2] To resolve wave-type processes, several grid points are generally required.

hindered a deeper understanding of 'real' atmospheric gravity-waves. The former has resulted in a rudimentary understanding of a climatology of the global tropospheric source of gravity waves. While both, inhibit an understanding of the exact nature of their interaction with the background winds. Recently however, sophisticated parameterisations have become available (*Hines* (1997a); *Medvedev and Klaassen* (1995); *Warner and McIntyre* (1999)), giving valuable insight into the dynamics of these waves and their effects within models. It is hoped that as our knowledge of gravity wave climatology grows, greater insight may be gained about their role in affecting climate. Only when computer power becomes sufficient to investigate processes on these scales and a clearer idea of a global source is achieved will the need for these parameterisations go.

The second chapter sets out to explain recurrent concepts discussed throughout this thesis. These include concepts such as geostrophic approximation, thermal wind, large-scale planetary waves and the residual mean circulation. Following this, chapter 3 introduces the idea of gravity waves - the subject of this work, starting from first principles as laid out in Appendix B and discussing their behaviour under generalised atmospheric conditions. Chapter 4 continues this theme, introducing the various sources thought to be important in producing these waves. It describes four gravity wave schemes; one developed to quantify the strength of a particular type of these waves over mountains (orography) and three more attempting to describe, in different ways, the behaviour of a vertically propagating spectrum of waves. Section 5.1 sets out to explore the significance of the interaction between two special sources of gravity wave and examine the similarities and differences between three gravity wave parameterisation introduced earlier. Both of these are done using columns of atmospheric variables representing the mean atmospheric state at various times and geographic locations. In a similar manner, but using 3-dimensional fields of UKMO (Met Office) assimilated data, chapter 6 extends this technique and explores how a rudimentary prescribed global source of gravity waves, originating from just above the ground, is affected by large scale structures in the atmosphere. The two chapters preceding the summary and discussion examine how a simulated climate is influenced by systematic changes in the strength of a global source and the use of different schemes utilising the same source.

Thus, it is the intention of this work to gain insight into the possible impact of gravity waves on climate, from examining the model atmospheric response to a perturbed gravity-wave source. By using modern, sophisticated parameterisations it is hoped that a common climatic response can be found, independent of whatever scheme is used.

Chapter 2

Dynamics

2.1 Climatological Features

The atmosphere is a complicated system dominated by dynamical and chemical processes which occur on a variety of scales - from molecular to planetary. In the context of climate, not only can large scale processes be influential, small-scale ones can have a significant effect. Ozone chemistry plays a dominant role in the middle atmosphere resulting in the dynamically static stratosphere through thermal heating. Gravity waves, although small in scale compared with some other waves, significantly alter the appearance of the upper mesosphere during times of solstice (mid summer/winter) - reversing the poleward temperature gradient and thus causing upwelling and downwelling of air over the poles via a north-south (meridional) movement of air.

Starting from the ground, the atmosphere steadily decreases in both pressure and temperature as air which is warmed near the ground rises and cools adiabatically (an expanding gas will cool as it expends energy pushing against surrounding air). Large convective cells can be generated over areas of significant warming, thoroughly mixing the (generally) moisture laden air. Cumulus cloud is formed from these processes and is an indication of the scales at which such processes can operate (although cumulus is not always associated with convection). Because the air near the equator is warmer than air at higher latitudes, winds form climatological (large-scale, quasi steady-state) jet structures in response to this poleward temperature gradient. This response is due to *thermal wind* (section 2.3). These winds are used extensively in air travel and are known as the jet-streams. This part of the atmosphere is known as the troposphere.

At heights above ~10-15 km temperatures begin to increase because of ozone related chemical processes heating the air. Even though ozone concentration diminishes with increased height, solar radiance increases. The net result is a heating maximum at the *stratopause* (~50 km). This vertical increase in temperature produces a stable stratification of air. This *static stability* is witnessed by air parcels oscillating about their equilibrium positions when displaced in the vertical. It is for this reason that air tends to remain at these heights for long periods. Once vertically displaced, an air-parcel will only remain so if the displacement is slow enough so that it comes into thermal equilibrium with its new surroundings, or if there is any latent heat exchange through water changing

phase. This is unlikely in these regions due to the air being stably stratified (air-parcels will quickly return to equilibrium positions) and dry (no latent heat exchange). Because of this layered structure, this part of the atmosphere is known as the *stratosphere*. Again, associated with the gradient in temperature at these heights, jet structures are seen most prominently during times of solstice. However, these are of opposing sign in the two hemispheres and coincide with differential solar absorption - the summer hemisphere receives more sunlight than the winter one (figure 2.1). These jet stratospheric jets change direction every six months.

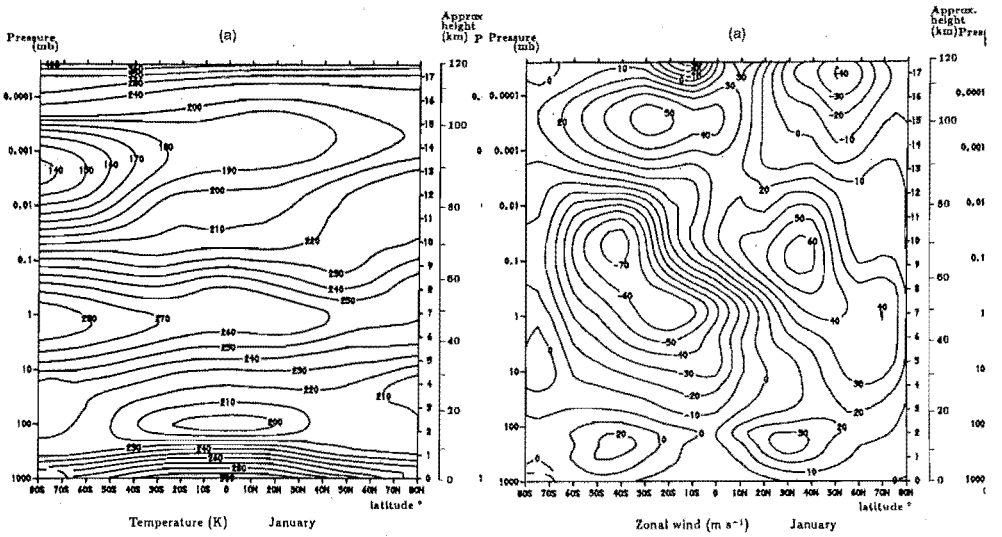

Figure 2.1: Atmospheric thermal wind structure. Distinctive jet-structures appear associated with horizontal differences in temperature. It is noticed that a third jet-structure appears at heights above 90km. This is believed to be in response to the direct effects of atmospheric forcing due to breaking gravity-waves (as opposed to thermal wind response due to differential heating). Similar profiles are seen in July, with a reversal of the wind jets and the latitudinal temperature gradient. [From *Fleming et al.* (1990)]

With diminishing levels of molecular ozone above ~50 km temperatures start to decrease again. This height heralds the start of the *mesosphere*. It is at these heights where small-scale gravity-waves and the larger atmospheric solar tides have a greater influence on the background state. This is because their amplitudes increase with decreasing air density. Jet structures are also seen in this part of the atmosphere during times of solstice. However, they are opposite in sign as compared to stratospheric winds lower down. It is the drag imposed by the *breaking* of these small-scale waves which is thought to produce these differences. Associated with these reversed wind jets is a reversed meridional (north-south) temperature gradient - cool summer mesosphere, warm winter mesosphere. This is a consequence of the thermal wind arising from the aforementioned dynamical driving (Fig. 2.2) and an associated ascent/descent of air over the poles.

Finally, as the air becomes sufficiently rarefied with height and photodissociation cou-

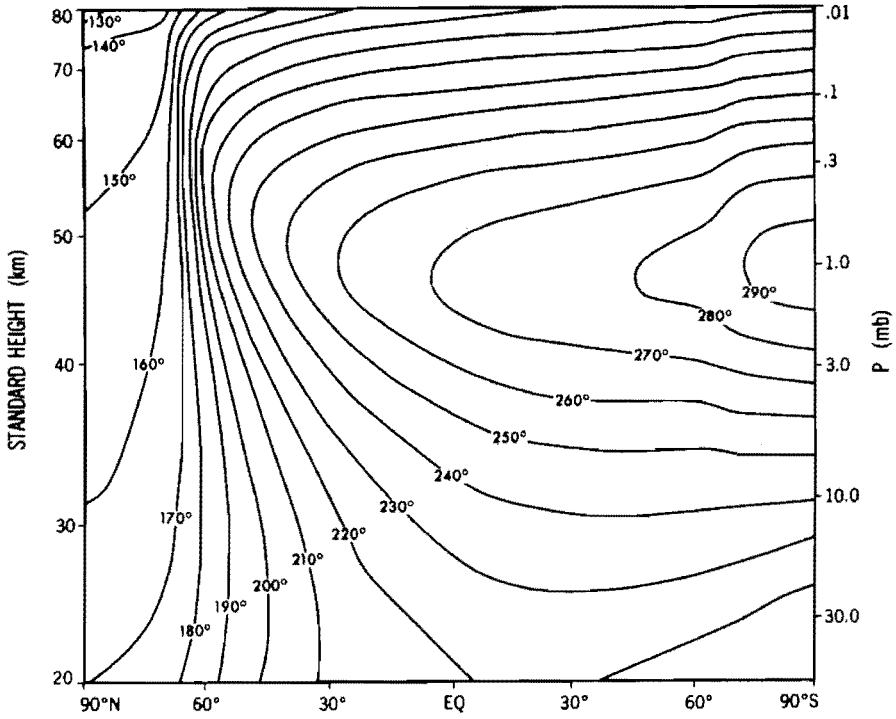

Figure 2.2: Zonal-Mean Vertical Profile of a Radiatively Determined Atmosphere. Model-produced global temperature profiles. Radiative, chemical (ozone) and convective processes are used, with a bottom boundary prescribed using seasonally varying zonal-mean values. Dynamical adjustment due to breaking small-scale gravity-waves has been ignored [From *Fels* (1985)].

pled with an increase in time between molecular collisions, causes electromagnetic effects to become significant. Different molecular species start to separate in concentration according to their respective scale-heights and temperatures start to increase with height again. The dynamics of this new region, the *thermosphere*, is appreciably different from the layers below. At still greater heights, the atmosphere becomes increasingly intertwined with the solar-wind and geomagnetic effects dominate.

2.2 Primitive Equations

Modern state-of-the-art computer models rely on two ways of representing the effects of real processes occurring in the atmosphere. The first deals with time-stepping a set of partial differential equations describing the atmosphere's state forward in time. Generally, these equations cannot be solved analytically and so numerical solutions must be sought. The second attempts to derive the effects of processes which occur at temporal or spatial scales beyond the resolution of the computer models which try to represent them. This process, called a *parameterisation*, uses what is already known about the process

in question and manually adjusts the appropriate fields in accordance with the current understanding of the effects of these processes. The treatment of gravity-waves is a good example of this. Until computer power is able to probe the scales at which these waves operate there will remain a need for such (gravity-wave) parameterisations.[1]

The former method deals with a set of equations called *prognostic* equations - ones which can be used to predict a future atmospheric state. These originate from a set of five *primitive* equations. These differential equations encompass both resolved and unresolved forces, issues of continuity and mass conservation, energy conservation and hydrostatic balance.

The first three primitive equations relate to the forces on a body in a fluid. Basically, a body experiencing an imbalance of body forces must move. Thus gradients in pressure result in fluid movement. Gravity, obviously must be taken into account and in fact features in a third momentum equation, which simplifies down to the hydrostatic balance equation (for flows considered in this thesis). Furthermore, any fluid which has a velocity gradient encounters viscous forces through diffusive type processes. Within a rotating frame, pseudo-forces operate. These include the well known centrifugal and Coriolis forces. In practise one generally uses a simpler set of equations, once scale analysis has been done (ignoring smaller scale terms in the equations). Recasting the equations in spherical coordinates and introducing non-conservatives forces from both resolved and unresolved waves, the momentum equations take the following form *Andrews et al.* (1987):

$$\frac{Du}{Dt} - \left(f + \frac{u \tan\phi}{a}\right) v + \frac{\Phi_\lambda}{a \cos\phi} = X, \tag{2.1}$$

$$\frac{Dv}{Dt} - \left(f + \frac{u \tan\phi}{a}\right) u + \frac{\Phi_\phi}{a} = Y, \tag{2.2}$$

$$\frac{\partial \Phi}{\partial z} = \frac{RT}{H}. \tag{2.3}$$

The D/Dt derivative notation denotes the total derivative, f is the Coriolis parameter (rotating reference frame), Φ the geopotential, a the earth's radius. X, Y are non-conservative frictional forces from both small-scale processes (e.g. gravity-waves) and larger scale ones (e.g. planetary waves).

For conservation of energy the total derivative of potential temperature must equal net heating, Q, or in terms of absolute temperature;

[1]It is of interest to note that some present-day working computer models, most notably the GFDL SKIHI Model have an operational resolution where it is thought that some of the dynamical effects resulting from model resolved gravity-waves can be represented without the necessity of any parameterisation [*Hamilton et al.* (1995)]. However, there is some debate whether certain effects produced in the model are attributable to model resolved waves. This question is the subject of part of this work.

$$\frac{DT}{Dt} + \frac{\kappa T w}{H} = \frac{Q}{c_p}, \tag{2.4}$$

Finally, conservation of mass is required;

$$\frac{\left[\frac{\partial u}{\partial \lambda} + \frac{\partial}{\partial \phi}(v \cos\phi)\right]}{a \cos\phi} + \frac{\frac{\partial}{\partial z}(\rho_0 w)}{\rho_0} = 0. \tag{2.5}$$

where the vertical coordinate z, is the log pressure height ($z \equiv -H \ln(p/p_s$, where p_s is a reference pressure). It is these five equations (2.1-2.5), in finite difference or spectral form, which form the basis of most atmospheric models.

2.3 Geostrophic Approximation

The foregoing section's equations encapsulate most of the major physics in the atmosphere. In practise however, source terms in the equations, notably subgrid-scale processes or unknown boundary and initial conditions, like the radiation input in the thermodynamic equation, make any firm predictions of a future atmospheric state impossible. This sensitivity to initial conditions is an inherent characteristic of the nonlinear nature of the equations themselves. This may prove fatal for computer simulations in the context of getting an accurate forecast. However, many features (e.g. tropospheric jets) persist in simulations without the requirement for accurate boundary data. The objective of forecasting therefore changes to an estimate of the probability of an event happening. Such a philosophy relies on carrying out many simulations, differing only in small deviations of initial conditions from some mean state. This is called carrying out an *ensemble* of runs.

Scale analysis is used to simplify the primitive equations by justifiably ignoring terms which are smaller in magnitude as compared to others. For the two horizontal momentum equations, the two largest terms are the horizontal gradients in pressure and the Coriolis torque terms. Leaving only these terms in the momentum equations yields the following geostrophic equations;

$$fv = \frac{\partial \Phi}{\partial x}, \; -fu = \frac{\partial \Phi}{\partial y}. \tag{2.6}$$

This approximation only holds outside the tropics and where the Coriolis parameter is non-vanishing. A useful dimensionless parameter used to check for geostrophic conditions is the Rossby number (Ro). It is defined as the ratio of the horizontal advection term with the Coriolis term from the momentum equations,

$$\frac{u}{fv}\frac{\partial u}{\partial x} \equiv Ro. \tag{2.7}$$

If this number is less than 0.1 then the approximation is assumed to be formally valid. Values above this, suggest such the approximation is not appropriate. It is noticed that near the tropics, where the Coriolis term is small, this approximation cannot be used. In such circumstances, it is often convenient to approximate tropical flow by finding the meridional derivative of the meridional momentum equation, giving;

$$u = -\frac{1}{a^2\beta}\frac{\partial \Phi}{\partial \phi} \tag{2.8}$$

Terms above are as defined in appendix A.

Another diagnostic equation can be derived from the primitive equations above. By combining the hydrostatic equation (2.3) with the zonal geostrophic wind expression (2.6) one obtains the *thermal wind* equation,

$$\frac{\partial u}{\partial z} \approx -\frac{R}{fH}\frac{\partial T}{\partial y}\frac{\partial v}{\partial z} \approx -\frac{R}{fH}\frac{\partial T}{\partial x} \tag{2.9}$$

This relation has important consequences for the large-scale atmospheric thermal and wind structure. Essentially one notices that differential heating over the latitudes leads to vertical wind gradients and associated jet structures. These features, as already stated, dominate both the lower and middle atmosphere during solstice periods.

2.4 Potential Temperature and Static Stability

On occasions it is convenient to re-express the above equations in other coordinate systems. In the horizontal plane it is often useful to use local Cartesian coordinates in place of spherical ones. This often simplifies the underlying equations. Generally, a simple Taylor's approximation is made to the coordinate system - in the atmospheric sciences this is known as the f and β-plane approximations. In the vertical, many atmospheric parameters like pressure and geopotential are one-to-one functions of height. Because of this, these parameters can be and generally are used in place of *geometric* or log-pressure height. Such a change can lead to a simplification of the equations.

One other example of an atmospheric parameter being used as a vertical coordinate is potential temperature. This parameter is defined as the temperature a parcel of *dry* air would attain if it were to descend (generally) adiabatically to some other height, usually taken to be ground level (to standard temperature and pressure). Such a change can be found by noting that the first law of thermodynamics, namely

$$dq = c_v dT + p d\alpha \tag{2.10}$$

where dα, dT and dq are differential changes in volume, temperature and net heat respec-

tively. Re-expressed in pressure coordinates and assuming adiabatic processes (dq=0), becomes,

$$0 = c_p d\ lnT - Rd\ p. \tag{2.11}$$

For a finite change in height, and so pressure ($P \rightarrow P_s$), the air parcel's temperature will change from T to T=θ via a trivial integration to,

$$\theta = T\left(\frac{p_s}{p}\right)^{R/c_p} \tag{2.12}$$

As a consequence of this definition, flow undergoing adiabatic motion or simply short-scale processes, travel along surfaces of constant potential temperature. It is this which makes this quantity an important diagnostic tool.

Potential temperature also lends itself to the derivation of another important atmospheric property. Taking the log of 2.12 and differentiating with height one obtains,

$$\frac{1}{\theta}\frac{\partial\theta}{\partial z} = \frac{1}{T}\frac{\partial T}{\partial z} - \frac{R}{pC_p}\frac{\partial p}{\partial z} \tag{2.13}$$

where upon substitution of the hydrostatic equation 2.3 and subsequent rearranging yields,

$$\begin{aligned}\frac{T}{\theta}\frac{\partial\theta}{\partial z} &= \frac{\partial T}{\partial z} + \frac{g}{C_p} \\ &= \Gamma - \Gamma_d,\end{aligned} \tag{2.14}$$

where Γ and Γ_d are the temperature and adiabatic lapse rates respectively (see Appendix A). It is noticed that if the potential temperature does not change with height then the change in temperature of a fluid parcel Γ_d, matches that of the surrounding air with changing height, Γ. However, if the vertical change in θ is greater than zero, implying $\Gamma < \Gamma_d$ then an upwardly displaced air parcel will be cooler and more dense than the surrounding air resulting in a downward restoring force. The converse is true for a downward displacement. Such conditions are typical in the stratosphere where there is the general trend of an increase in temperature with height. This is known as static stability. If $\Gamma > \Gamma_d$ then the atmosphere is said to be statically unstable resulting in convective motions.

A convenient measure of static stability is the *buoyancy frequency, N*. This parameter is the frequency of oscillation of a parcel of air within statically stable surrounds. Often expressed squared, it is defined as,

$$N^2 \equiv g\frac{\partial \ln\theta}{\partial z}. \tag{2.15}$$

It is seen that N^2 can assume negative values if potential temperature drops off with increased height. This is associated with statically unstable conditions. The theory associated with this definition can be found in most standard texts (c.f. pages 53,54 *Holton* (1992)).

2.5 Vorticity

The concept of angular momentum conservation is a useful one when considering processes in the atmosphere. However, due to the earth's rotation and the atmosphere being a continuous fluid such a concept becomes more subtle. As such, vorticity - the infinitesimal measure of rotation of a fluid parcel about its own axes, needs to be defined. From it comes particularly useful conserved quantities which prove invaluable in the description and analysis of a variety of atmospheric processes, most notably, large-scale atmospheric waves.

Mathematically, rotation in fluid flow is defined as a non-vanishing curl of the flow field. In fact the *vorticity equation* is defined by taking $\frac{\partial}{\partial x}(2.2)$ and subtracting this from $\frac{\partial}{\partial y}(2.1)$. This is the vertical component of vorticity, as only motion in the horizontal is wanted (a fair approximation). Doing this yields,

$$\frac{D\zeta}{Dt} = -f\left(\frac{\partial u_a}{\partial x} + \frac{\partial v_a}{\partial y}\right). \tag{2.16}$$

Equation 2.16 is known as the vorticity equation. ζ represents the total vorticity and is composed of the sum of two terms - vorticity associated with our rotating planet (planetary) and that which is seen as viewed in the ground based frame (relative). This expression has been simplified considerably by using scale analysis to remove extra terms and local Cartesians have been used, so the f-plane approximation has been used in place of the Coriolis parameter[2]. It is noticed that the presence of the divergence term on the right, serves to either create or destroy vorticity. Because of this non-conservation of vorticity (i.e. the total derivative does not necessarily equal zero), quasi-geostrophic vorticity does not prove to be a useful quantity.

A change to isentropic coordinates (where potential temperature is used in place of the geometric height as the vertical coordinate) and using a quantity known as *Ertel's Potential Vorticity*, one obtains an expression which *is* conserved in most short-lived atmospheric processes. This vorticity has the form,

[2]In localised Cartesian coordinates it is often convenient to re-express the Coriolis parameter as either the first or first two terms of a Taylor expansion about some point. This is known as the *f-plane* and *β-plane* approximations, respectively.

$$\frac{\tilde{\zeta}}{\sigma} = \frac{f - \frac{\frac{\partial}{\partial\phi}(u\cos\phi)}{a\cos\phi} + \frac{\partial v}{\partial\lambda}\frac{1}{a\cos\phi}}{\sigma}. \tag{2.17}$$

σ is the isentropic density and is defined as the mass contained in a unit isentropic volume bounded between two heights of differing potential temperature (see Appendix A). The advective derivative of this quantity is proportional to the sum of the Jacobians of X, Y, q. For frictionless, adiabatic flow (i.e. $X = Y = q = 0$) this implies that these terms must be zero, suggesting that this form of vorticity is conserved. Because of this, contours of constant potential vorticity are used extensively as an atmospheric tracer - air will tend to move along these contours over short time scales (a few days).

2.6 Rossby Waves

Unlike other kinds of waves, Rossby waves are not characterised by air parcels returning to equilibria via the action of buoyancy (e.g. gravity waves) or pressure (e.g. sound waves). They are large-scale disturbances, where Coriolis effects dominate and provide a restoring force. These waves can be found to be forced or *free-mode*, bound about low latitudes or unbound, travelling with respect to a ground based frame or fixed in phase to the ground (stationary). For this thesis, special attention will be paid to the latter type.

Stationary modes can be forced by topography or the thermal contrast between land and ocean. As a consequence it is found that these waves appear stronger in the northern hemisphere where there is both a greater land mass and azonal distribution.

Like much of the description of the atmospheric state, the mathematical description of Rossby waves is normally quite complicated. *Charney and Drazin* (1961) were among the first to undertake a detailed study of quasi-geostrophic waves. They used the geostrophic potential vorticity equation using the beta-plane approximation to investigate the vertical structure of steady waves forced at a lower boundary. Using an idealised atmosphere having constant zonal wind and static stability (as measured by the buoyancy frequency, N) they obtained an important result which remains valid in more detailed analyses;

$$0 < \bar{u} < \beta[(k^2 + l^2) + f_0^2/4N^2H^2]^{-1}. \tag{2.18}$$

Where $\bar{u}$ is the zonal mean wind, k and l are the meridional and zonal components of wavenumber, while f is the Coriolis parameter, β its meridional gradient, N static stability and H scale height. This inequality suggests that the vertical propagation of stationary planetary waves is dependant on both the strength of the overlying wind and the scale of the wave. These waves will not propagate up through easterly winds or strong westerly winds. As a consequence of this, Rossby waves are seen to propagate vertically up through the stratosphere during winter but not summer. More sophisticated analyses

(*Matsuno* (1970); *Schoeberl and Geller* (1977); *Lin* (1982)) incorporating more realistic atmospheric features (e.g. a varying zonal wind and damping terms in the underlying equations) affirm the above result of *Charney and Drazin* (1961) and predict that only the largest scale waves - wave one and two, can propagate vertically into the stratosphere.

Other large scale waves also exist which arise from amplification of small instabilities. Baroclinic waves arise through instabilities which develop because of the thermal difference between the equator and polar regions. Convection carries heat away from the equator to the poles. Consequently, currents of air move toward the equator from higher latitudes. This meridional transport is modified by the Coriolis force which acts to move the air zonally. The pressure gradient associated with the poleward differences in temperature are thus counter-balanced by the Coriolis force. This hinders the flow of heat to the poles. Instabilities can develop because of this which can grow to planetary scales. These are seen as the mid-latitude synoptic high and low pressure systems. These wave-like disturbances can transport heat away from low latitudes faster than convection which is hindered by the Coriolis force. A poleward gradient in the zonal wind can also lead to the creation of another set of waves through *Barotropic* instability. These are more likely to occur if the poleward gradient of potential vorticity changes sign.

Not only do baroclinic waves occur in the troposphere they have also been linked with planetary sized waves at mesospheric heights. The *two-day* wave has been studied extensively (*Harris and Vincent*, 1993; *Randal*, 1994, e.g.) and has been recently associated with baroclinic instabilities. *Norton and Thuburn* (1996) using a modified version of the UK Global Atmospheric Modelling Programme (UGAMP) general circulation model (*Slingo et al.*, 1994) generated a two-day-wave in the northern summer mesosphere of their model. They linked this to gravity wave drag on the background flow causing a reversal of the latitudinal temperature gradient via circulation changes. Associated with this drag was a noticeable change in sign of the meridional gradient in potential vorticity. They concluded that the existence of this wave was probably due to the presence of a baroclinic instability aided by the forcing of the flow by breaking gravity waves.

2.7 The Residual Mean Circulation

Large scale flow in the atmosphere is not only confined in a zonal (east-west) direction, comparable flow occurs meridionally (north-south) as well. However, this is mostly associated with eddies (vortex-like structures which, like waves, carry energy and momentum) and tend to disappear, when averaged over large timescales. In the troposphere, non-zonal circulation occurring in the tropics is associated with differential heating about the equator and creates large circulating *Hadley* cells which rise over areas of maximum heating to heights of about 10-15 km and descend poleward and down at higher latitudes.

These circulations are responsible for surface winds directed toward the equator within the tropics and have been known for many years as the trade winds. At higher latitudes, the circulation is directed in an opposite sense to those about the tropics. Ferrel cells make up this circulation and are associated with baroclinic waves which are the most conspicuous synoptic structure at these latitudes.

However, about the extratropics, large scale, largely time independent meridional flow is hindered by the fact that there exists a large gradient in planetary angular momentum at these latitudes - the planet is large, spherical and rotating. Such flow is hindered in that one must conserve angular momentum and unless flow is driven by an external source, such flow is limited. In the (winter) stratosphere though, there exists a largely poleward *residual* meridional circulation which is seen to transport tracers like ozone from their source in the tropics, towards the poles. In order for this to occur, large scale forcing must occur - this is achieved mostly by breaking of large scale eddies called Rossby waves which can propagate into the middle atmosphere during wintertime. Higher still, in the mesosphere, pole-to-pole circulation is observed. This is thought to be driven by small scale gravity waves which *force* the background flow when they are thought to break down, akin to waves on a beach, when the air becomes too rarefied to support their motion.

Associated with this wave driven meridional circulation is vertical motion over the poles. This arises simply due to continuity considerations - the air must go somewhere and the fact that cold air descends. Thus rising motion is associated with meridional motion away from the pole and descent is linked with convergence of air on the pole.

An important result explored by *Haynes et al.* (1991) concerns the relationship between the momentum carried by atmospheric waves (namely gravity waves) and the mean circulation. If it is assumed these waves break somewhere in the atmosphere, the circulation at a particular height would be proportional to their total momentum and its associated latitudinal derivative, namely;

$$\bar{\omega}^{\star} = \frac{-1}{a\cos\phi}\frac{\partial}{\partial\phi}\left(\frac{\overline{u'w'}\cos\phi}{2\Omega\sin\phi}\right). \tag{2.19}$$

Where $\overline{u'w'}$ is a time average of the horizontal and vertical winds associated with the waves averaged over one wave cycle. This expression represents the vertical flux of horizontal momentum associated with the waves and $\bar{\omega}^{\star}$ is the resultant mean vertical motion. This result is independent of where above the waves eventually break. This will be instructive when diagnosing circulation patterns as seen from output of simulations discussed later in the thesis.

Chapter 3

Gravity Wave Theory

Gravity-waves are defined by the forces which act around them - those being buoyancy[1] and gravity. Examples of a type of gravity wave are surface water waves. Unlike these surface waves, *internal* gravity waves are not restricted to move along media boundaries, but can propagate through a stably stratified medium. Like planetary waves they show increased amplitude with height and as such tend to be the dominant part in fluctuations of the background wind at mesospheric heights (figure 3.1). They are also produced predominantly in the troposphere by a variety of processes such as convection, flow over mountains and meteorological fronts, whereby they transfer momentum to higher parts of the atmosphere.

Their mathematical description comes from making a number of simplifications to the primitive equations 2.1-2.4 and solving for wave-like solutions. As laid out in Appendix B, a linearisation of the primitive equations yields equations B.2-B.3, in Cartesian coordinates. Solving for these, yields a wave-equation B.11 and dispersion relation, B.12;

$$\hat{w}_{zz} - \left(\frac{N}{\bar{u}-c}\right)\hat{w} = 0, \qquad c \equiv \omega/k. \tag{3.1}$$

$$m^2 \equiv \frac{N^2}{(\bar{u}-c)^2} \Rightarrow \frac{m^2}{k^2} = \frac{N^2}{\tilde{\omega}^2}. \tag{3.2}$$

Here, the gravity wave is denoted by fluctuations about the mean vertical wind, w. The horizontal phase-velocity of the wave is defined as the ratio of the angular frequency ω, to the horizontal wavenumber k and the vertical wavenumber is denoted by m. Other parameters have their definitions in Appendix A and B. The dispersion relation relates the gravity-wave frequency to the horizontal and vertical wavenumbers. This particular dispersion relation precludes the largest scale waves ($>$ 1000 km), which are influenced by Coriolis effects.[2] The sign for the vertical wavenumber is chosen so as to allow positive

[1] The origins of the buoyancy *force* is gravity

[2] All three gravity wave schemes studied in this thesis use this simpler dispersion relation.

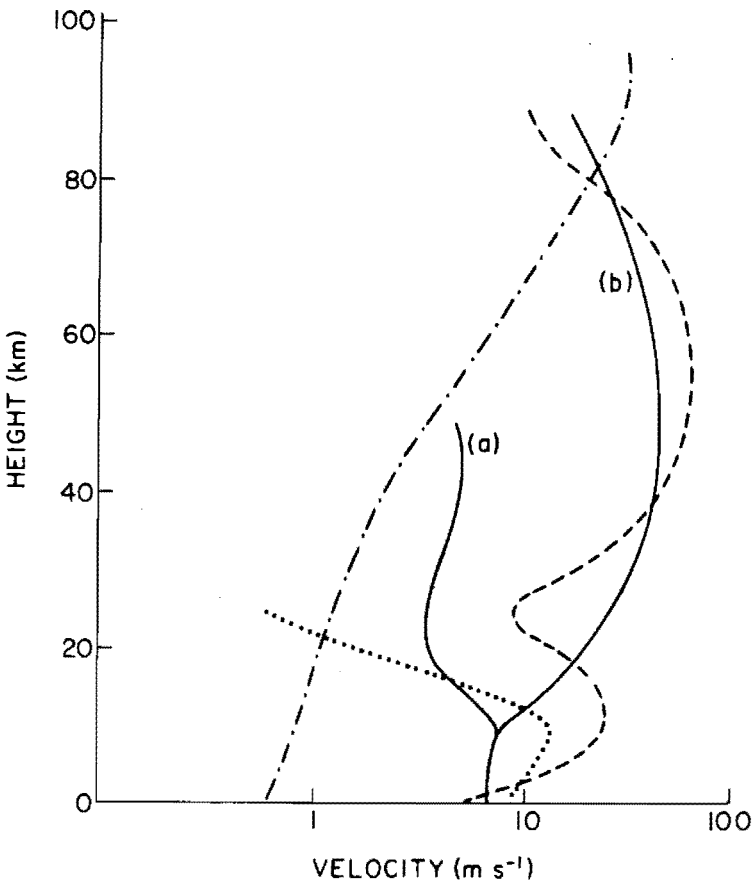

Figure 3.1: vertical profile of different waves' wind amplitudes. Comparison between the horizontal wind amplitude of a number of atmospheric waves. Solid line: planetary waves (a) summer, (b) winter; dashed: zonal mean; dotted: synoptic scale; dotted-dashed: gravity-waves (from *Andrews et al.* (1987)).

values for $\partial\omega/\partial m$ - which is required if energy is to be directed upward (a fair assumption if one is assuming that these waves originate from sources in the troposphere). Doing this restricts the form of the dispersion relation to $m = -Nk/\omega$. On examination of this, one sees that the phase velocity of these waves is directed opposite to the direction of wave energy propagation (group velocity). Unlike some other atmospheric waves, the propagation of gravity waves is not restricted to the direction of the mean background flow or to particular geographic locations.

Observationally, gravity waves are seen as fluctuations of wind or temperature about the mean. With the exception of waves generated over mountains, gravity waves are most often observed as composing a broad spectrum. This spectrum comprises waves having a wide range of vertical (O(10-1000m)) and horizontal scales (O(10-1000km)). Their related power spectra (expressed as a function of vertical wavenumber) display a characteristic form at high vertical wavenumbers. This form has been shown to be independent of both geographic location and time of year. This form has been explained in terms of

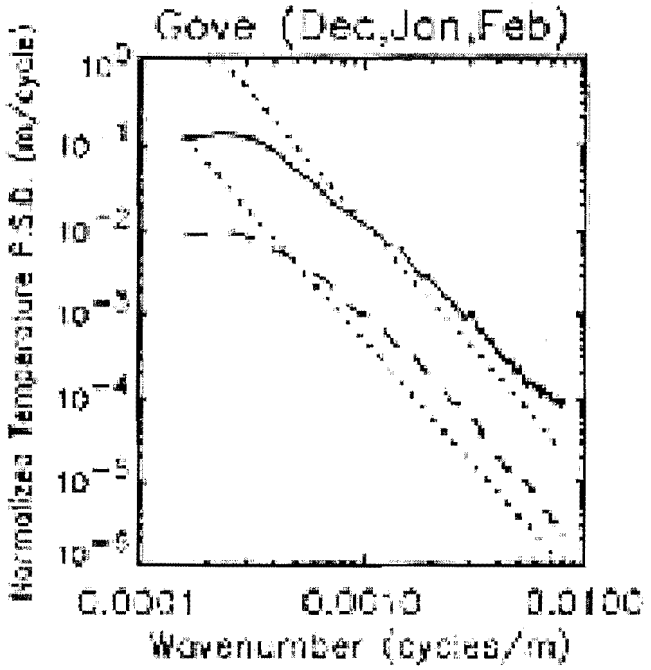

Figure 3.2: Normalised temperature power spectra density of two vertical temperature profiles at Gove during summer (DJF). An example showing the universal slope of wave perturbation power spectra at high vertical wavenumber. The dashed curve represents power spectra at tropospheric heights, whereas the bold line is taken over a height interval in the lower stratosphere. The dotted lines are theoretically predicted power spectra (courtesy of *Allen and Vincent* (1995)).

saturation processes which limit the growth of the smaller scale waves as they propagate in the vertical (*Allen and Vincent*, 1995).

There have been a number of mechanisms proposed for the existence of this *universal* shape in the vertical wavenumber power spectra (*Fritts*, 1989). It is still unclear, however, as to the relative importance of each of these mechanisms. The first of these is classed as linear instability. This states that the amplitudes for these wave perturbations is restricted by the state of the background atmosphere - in the absence of other waves. Convective instability is thought to result when the presence of a gravity wave field reduces the stability of the mean background state;

$$\sigma_z = \bar{\sigma}_z + \sigma'_z = 0, \tag{3.3}$$

where the subscript denotes differentiation in the vertical, σ denotes potential temperature, while overbars and primes represent mean and perturbed quantities, respectively. When this condition is met, further growth of the wave is thought to be hindered by the production of turbulence. A second mechanism for saturation is thought to occur

when the intrinsic frequency of the wave approaches the inertial (Coriolis) frequency [3]. This cannot happen under the assumptions made in the dispersion relation (equation 3.2) because its formulation specifically neglected the effects of rotation (Appendix B).

Other mechanisms proposed to explain saturation include the effect of nonlinear interactions between waves within the spectrum. The three different gravity wave schemes described and used in the following chapters combine the effects from both the spectrum of waves and the background state through which they propagate.

Using the dispersion relation one can derive qualitatively the effect of a spectrum of waves incident from tropospheric heights. If one were to assume a spectrum of waves with no preferred direction propagating up through the middle atmosphere, one would expect on examination of the above dispersion relation, that waves having velocities and directions comparable to the mean flow would break as their intrinsic velocities (defined as the mean wind minus the ground based velocity of the wave, $\bar{u} - c$) are Doppler shifted to zero, with an accompanying diminution of its vertical scale. Under solstice conditions, zonal mean winds in the middle atmosphere are generally westerly in the winter hemisphere and easterly in summer. Only waves having phase velocities in excess the strongest winds will survive (in the direction of the mean wind). However, waves travelling in the opposite directions will be unaffected and in fact Doppler shifted to larger vertical scales. As it is uncertain where in the troposphere most of these waves are generated, filtering by tropospheric winds must be viewed with caution. Thus, a distinctly anisotropic *spectrum* of waves will remain at mesospheric heights. Waves entering the mesosphere will tend to carry horizontal momentum opposite to the direction of the underlying wind fields. On encountering critical levels, these waves will break and reduce the magnitude of the underlying jets and reversing their sign. This is seen in observations and cannot be explained by radiative processes alone.

Associated with these waves is a wave pseudo-momentum flux, τ.

$$\tau_u \approx \frac{1}{2}\frac{\rho N}{\tilde{\omega}} u'^2 \tag{3.4}$$

This quantity is conserved for steady undamped motions (see *Eliassen and Palm* (1961) for details). That is, barring critical layer processes[4], the divergence of this is zero. A bookkeeping of the amount of wave-momentum deposited when these waves are breaking is found by noting differences in τ between different heights. Namely,

$$F_u = -\frac{1}{\rho}\frac{\partial \tau_u}{\partial z} \tag{3.5}$$

[3]intrinsic frequency is defined as the frequency observed for a gravity wave as measured in a reference frame travelling with the wind

[4]those processes which lead to dissipation of gravity waves

It is this expression which is used in parameterisations to monitor the force on the background flow. This is equivalent to Newton's second law of motion which is usually described by a time rate of change in momentum.

It is usually desirable to remove the condition that $\bar{u}$ and $\bar{T}$ do not vary with height. However, analytic solutions to equation B.11 are generally not possible. Only approximate solutions are possible if one assumes that the mean fields vary less than the perturbations associated with the waves themselves. Such solutions are often called WKBJ approximations and are generally employed by most operational parameterisations.

Chapter 4

Gravity-Wave Sources and Schemes

4.1 Tropospheric Sources

As stated in chapter 3, gravity-waves are produced when air flow is forced to deviate from an equilibrium position in the vertical - possible mechanisms include: orographic, frontal (colliding air-masses), wind-shear or convection. Recently, attempts have been made to extract information of wave momentum fluxes (and energies) from convection using precipitation data (*Chun and Baik*, 1998), such information can then be readily used as input in models (*Bossuet et al.*, 1998). However, the simplest process for source generation is from topographic obstacles. Conceptually, this mechanism is the easiest to visualise and has been studied extensively (*Bacmeister*, 1993; *Bacmeister et al.*, 1994; *Gregory et al.*, 1998; *Hines*, 1988; *McFarlane*, 1987; *Palmer et al.*, 1986). In general, any treatment of these (and indeed any) waves must address such source mechanisms along with issues of propagation and dissipation. Accordingly, for this work, source quantification, from topography, has been addressed separately (*Bacmeister*, 1993; *Bacmeister et al.*, 1994) from propagation and wave dissipation (*Hines*, 1997a,b; *Medvedev and Klaassen*, 1995; *Warner and McIntyre*, 1999). The offline coupling of orographic forcing from the Bacmeister scheme, with the spectral schemes is one of the new elements of this work.

4.1.1 Source Quantification - Bacmeister

A comparatively simple scheme quantifying the strength of topographically generated gravity-waves (mountain waves) was put forward by Bacmeister (*Bacmeister*, 1993) to address the issue of the effects planetary waves on the modulation of upwardly propagating mountain waves. He noted that the amount of mountain wave momentum flux[1] surviving to mesospheric heights was significantly affected by the strength of the planetary waves below. Notably, it was found that an enlarged Pacific Aleutian high produced critical level filtering of gravity-waves along the Rockies. This resulted in the amount of southern hemisphere mesospheric drag being comparable to that in the northern hemisphere, even with the lack of topographic obstacles in the south.

[1]It is intended that this be abbreviated from vertical flux of horizontal momentum, with no loss of generality.

The scheme relies on the determination of mean topographic parameters from a sub-grid-scale dataset. In the original study, a resolution of 2.5°-2.5° was constructed from the NCAR 5'-5' naval dataset[2] (for this study, a resolution of 5.0°-5.0° was used). In that study, two topographic parameters were used together with the daily 18-level global wind and temperature analyses from the NMC climate analysis centre to construct a 'ground-level' momentum flux source. The analysis extended through a height range of 1000mb to 0.4mb (approx. 0-60km).

For this study, the topographic dataset was first interpolated into boxes of size 500km - 500km containing 60 × 60 points. This corresponds to a 5.0°-5.0° sized 'block' area about the equator. Each latitude had a box centred at 2.5°E with even 5.0° increments along each line of longitude. The southern-most latitude had its block-centres at 87.5°S. Because of sphericity an increase in the number of grid-points in the high resolution dataset are admitted into each of the boxes as the poles are approached. Because of this, a suitable interpolation is made for each line of latitude. In the original paper, the effects of curvature were ignored within each analysis box, however for this study (where a 5°x5° resolution is used) curvature effects were taken into account. This action was done so as to standardise the distance between adjacent analysis boxes. Before this was done, all points of the original topographic dataset having negative elevation were set to zero and a five and eleven point smoothing was passed over the data, separately.

The results from the five point filtering were then subtracted from the eleven point one, this created a topographic deviance field. The sized filters were chosen so as to retain only those geographic features thought able to generate mountain waves able to penetrate past the tropopause and contribute significant momentum fluxes. Physically these scales were taken to be between $\approx 50 - 100\ km$.

Next, in order to isolate the dominant ridges within each analysis box all negative valued points in the topographic deviance were set to zero. Next, the highest 25% deviances within each box were set to a value of one, while the remainder were set to zero - this was termed the skeleton topography. Following this, a three point filter was then passed over, with the result subtracted from the skeleton topography, creating a skeleton deviance. The orientation of the dominant ridges in a given grid-box was found using a set of ridge functions - R(x,y,θ). For a given point (x,y) in a field (e.g. the skeleton deviance) the action of the ridge function was to multiply the value of the field at some point by the sign of the value of the field at some surrounding point at some angle, θ (see 4.1). Thus if one were to sum the result of the ridge functions on the field over all points x,y in a box one would observe a maximum (roughly) along a ridge (or trough!). The distance between the two points must, however, be greater than the minimum size introduced by the filtering (noting that the resolution of the naval data-set is ~8.33km at the equator,

[2]refer to http://dss.ucar.edu/datasets/ds759.1/

giving a geographical range in scale after filtering of 50-100km). In the original analysis (and here also), the function was defined for 18 possible orientations. However, for this study the range was taken to be between 45° and -45°, instead of 90 ° and -90° in the original study. These directions relate to the line of a ridge. The direction perpendicular to this is what is important in calculations and in fact two possible directions are possible - each 180° apart. Also the direction the local wind is blowing will determine which of these is used in any calculations.

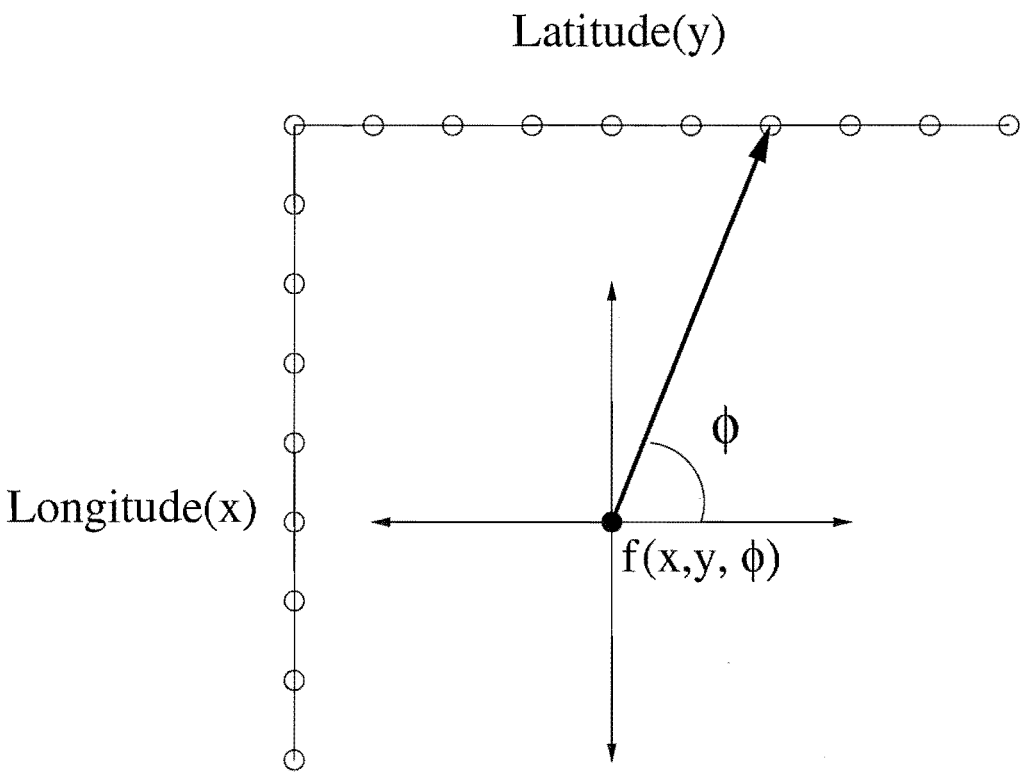

Figure 4.1: Ridge-Function Definition. The two sided stencil is passed over each point in each analysis box. A comparison is then made between the centred point and the points on the stencil, generally $\zeta_{cen} - \zeta ste$. This produces a function dependent on orientation, $\zeta(x, y, \theta)$.

The action of the ridge-functions on the skeleton deviance gave a quantity, f_r. This indicated the level of *ridginess* of a feature within a box. A second quantity, a_r, representing the mean absolute topographic deviance of a box feature was found by acting the absolute value of the ridge-function on the absolute value of the topographic deviance. In the original study, the highest values of a_r attained within each box were typically a factor of 20 smaller than the actual heights of peaks themselves. Basically, this parameter indicated the degree of *corrugation* about the ridges.

Finally, a quantity, abs($f_r a_r$) was constructed, indicating the topographic grain within an analysis box. In both the original and this study this parameter was highly dependent on ridge orientation, θ_{max}. The results of this can be seen in figure 4.2.

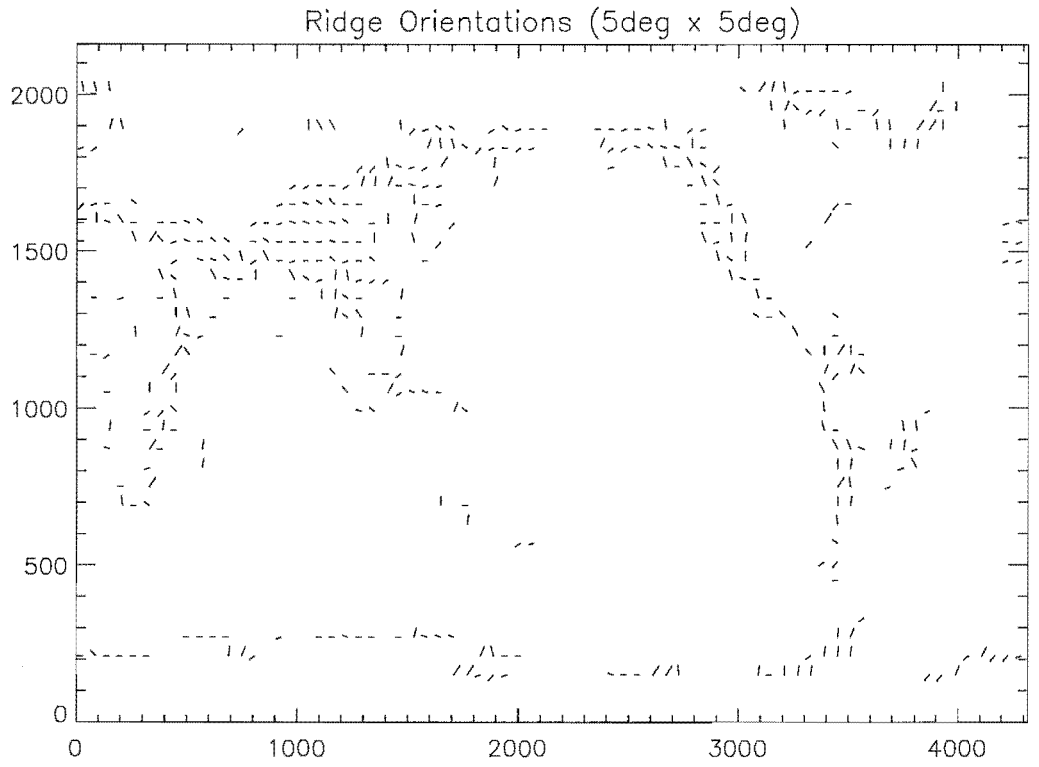

Figure 4.2: Global Distribution of Ridges. The parameter abs($f_r a_r$) produces a satisfactory distribution of the major mountain ranges, at a resolution of 5°x5°. Axes display arbitrary units.

It was noted in the original formulation that to approach the problem using Fourier analysis would have limited the angular resolution of the resulting ridges. Bacmeister explains this happens as '...the ridge-like features of interest, 50 to 100km, were an appreciable fraction of the width of the analysis boxes used in the ridge determination...'. He continues, '...thus the features of interest tended to show up in the lowest two to three wavenumbers of the Fourier transform'. He also cites that smaller more periodic features may show up more prominently than larger, more isolated ones. The fore-mentioned algorithm, although convoluted, gave satisfactory results.

Once a global set of ridge orientations and deviances have been calculated, a global orographic gravity-wave source can be approximated using an overlay of temperature and wind fields. The fields used were UKMO assimilated wind and temperature data. Unlike the original analysis no interpolation was needed to superpose the geographic and UKMO fields. In order to determine the direction of any gravity-waves produced by the ridges, one had to first find the projection of the wind to the normal presented by the ridges. Any waves are thought to propagate upwind from the ridge (although their phase-velocities are zero).

It is of interest to note that different terrain configurations produce differently ori-

ented waves. For example, in assuming an isotropic terrain, *Hines* (1988) found that the momentum flux directed away from a 'mountain' was directed principally in *two* directions flanking the background wind (Fig. 4.3). Only ridge-type topographical features have been dealt with in this work.

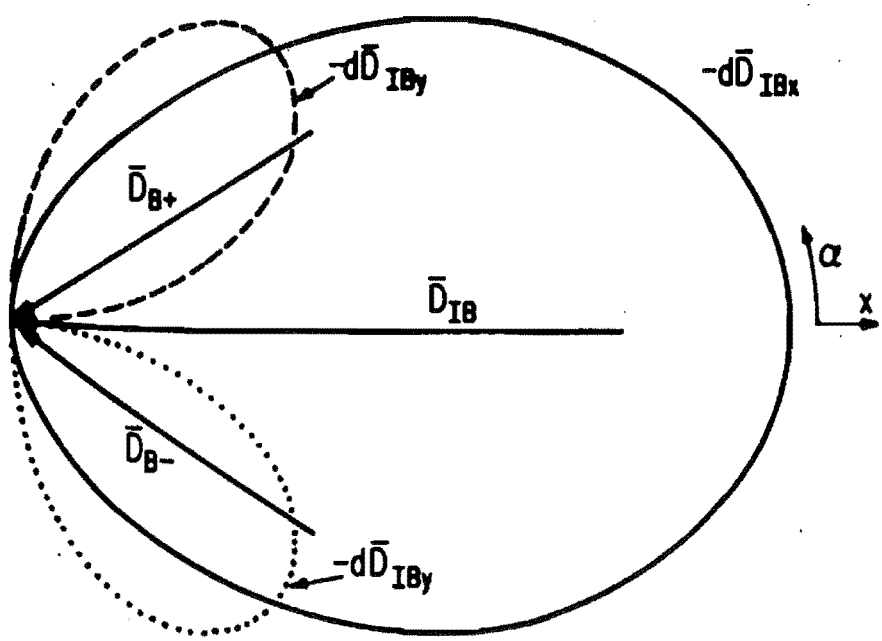

Figure 4.3: Direction of GW Momentum Fluxes from Isotropic Terrain. Lobes of momentum flux lie at an angle of 32.5° from the upwind direction (from *Hines* (1988)).

One simplification made by this gravity-wave scheme, is to assume saturation of wave amplitudes over all ridge. In the original study a launch height corresponding to 850 HPa was assumed, but for simplicity, this was taken as the bottom-most level of the UKMO dataset - 2000 m. Doing this, allows for a straight-forward calculation of wave-amplitude, $\delta = U_{rdg}/N$. Where U_{rdg} is the ridge normal wind projection and N is the local stratification frequency. According to linear WKBJ theory, wave momentum is conserved (with increased height) until wave amplitudes reach values stated above *Lindzen* (1981). However, as saturation suggests, further wave growth is prevented by certain dissipative processes. These may include wave-wave interactions whereby the energies of waves of small scale are *transferred* to waves of larger scale. Also '...small-scale instabilities initiated during wave breaking are assumed to act through an enhanced eddy diffusivity to maintain wave amplitudes at the saturation limit' (*Bacmeister*, 1993). Once a wave deviance has been found, the momentum flux can be derived using;

$$F_r = \Phi N V \delta^2 \rho R / L \tag{4.1}$$

Here, the momentum flux projected upwind normal to a ridge, F_r, is dependent on factors such as; proportion of a given area covered by a ridge (and so wave) or intermittency in time of a gravity-wave source (*Webster*, 1997), Φ, stratification frequency, N, ridge-normal wind projection, V, wave-deviance δ^2, atmospheric density ρ and ridge shape and width, R and L, respectively. The ridge shape is a 'geometric' factor and has a value of $\sim$1.5 for the original study. Essentially another fudge-type factor, this takes on a value of π when assuming sinusoidal topography (*Pierrehumbert*, 1987). Again assuming sinusoidal type terrain, L represents the wavelength of the geographical undulations. A value of 100km was assumed.

As a wave propagates upward its amplitude must increase to conserve wave-momentum due to the decrease in atmospheric density. While saturation is not occurring the wave-variance (or wind-variance, depending on which is used in calculations) changes according to;

$$\delta^2_{prov} = \delta^2_{prev}(\rho_{prev} N_{prev} U_{prev}/\rho NU)^{1/2}, \tag{4.2}$$

where subscripted quantities refer to a height of some *previous* level below the current height of the wave. This equation is found simply by equating momentum fluxes between these two heights (wherever conservative propagation is occurring). δ^2_{prov} refers to a *provisional* value for the wave (wind) variance. It becomes the true value at some height whenever it is less than that predicted for a saturated wave, namely, U/N. Otherwise the saturated value is used.

One final point regarding the source concerns the available area covered by waves from a ridge. Instead of attributing all out-of-scale effects into some fudge factor, the previous ridge analysis provides the average topographic deviance parameter a_r for this. The fractional area assumed to have vertically propagating mountain waves is given by S_w

$$S_w = \begin{cases} 0, & \text{if } a_r < 30\text{m} \\ 0.5(a_r/100m), & 30\text{m} \leq a_r < 100 \text{ m} \\ 0.5, & \text{if } a_r \leq 100 \text{ m}. \end{cases} \tag{4.3}$$

The factor of one half in the above equation refers to the fact that in the original analysis it was assumed that about one half of a given grid box could be covered by mountain waves. As the grid box in the current analysis is twice the (linear) size of that used in the 1993 paper one could assume this factor to change in some way. However, given the uncertainties held by the other fudge-factors already, it has been chosen to leave this unmodified. The 100 m limit corresponds to saturation being achieved for topographic heights of over $\sim$1000 m (remembering that the deviances are of the order

of 10-20 times smaller than peaks within the analysis boxes). This S_w factor enters into the calculations only after any wind tendencies from wave-breaking have been determined from whichever deposition scheme is being used. It is seen that only over regions in the Andes and Himalayas does this factor reach 0.5 (Fig. 4.4). This result differs from that obtained in the 1993 paper, as one would expect - a larger box must encompass a greater proportion of terrain which is flat, thus bringing down any average therein.

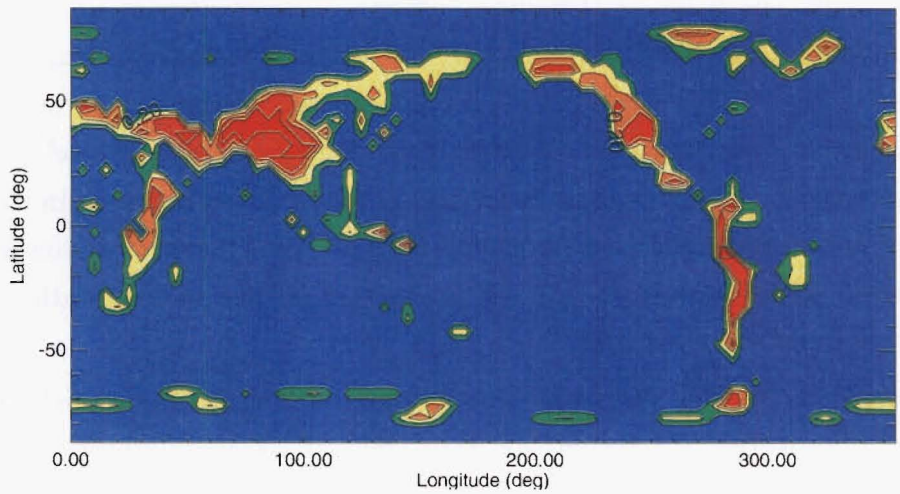

Figure 4.4: Global Topographic Deviances. A global distribution of the parameter S_w indicated areas of significant topographic roughness. Values range between 0.15 and 0.5. The latter indicating regions where saturated ground momentum fluxes ought to propagate.

4.2 Doppler Spread Theory

The Doppler Spread Theory, as set out by Colin Hines (*Hines*, 1991a,b,c, 1993) and summarised for use in climate models in (*Hines*, 1997a,b), attempts to account for the saturation characteristics of a broad spectrum of gravity-waves in terms of their interaction with other parts of the spectrum. This interaction is encapsulated by the advective derivative, $V \cdot \nabla$, of Eulerian theory. The essence of this interaction, is that gravity-waves are susceptible to the state of the background wind surrounding them. When the spectrum is not saturated, that part of the *background* wind associated with other waves is minor compared with the mean wind. However, when the phase speed of smaller scale waves, which travel the slowest, matches the combined wind deviance of all other waves in the spectrum, non-linear interaction becomes influential and saturation sets in.

The concept of *saturation* has been developed to help explain the observation of the unique spectral shape of power spectral densities of horizontal wind versus vertical wavenumber observed (refer to figure 3.2). For high wavenumbers, this shape takes the form of a slope of ~ -3 and is invariant of geographic position, height or time of

year. Much work has focused on attempting to explain the existence of this shape by a number of people, most notably *Dewan and Good* (1986); *Smith et al.* (1987); *Weinstock* (1990). Each have considered separate mechanisms. With the uncertainties inherent in the approximations made in their analyses, it is difficult to ascribe to any given mechanism greater importance over any of the others. This issue has received much attention (*Gardner* (1996); *Hines* (1998); *Gardner* (1998)). Doppler Spread Theory (DST) also purports to explain the value of this slope, however it is somewhat underestimated at high wavenumbers (*Hines* (1993)). Hines suggests this is due to neglecting vertical wave induced winds in the Doppler-shifting calculations. Further criticism has come concerning the use of the entire spectrum wind deviance in Doppler-spreading those elements within undergoing saturation. The argument concerns the matter of some waves in the spectrum being of an inappropriate intrinsic frequency (higher) to influence the lower frequency waves (*Medvedev and Klaassen*, 1995). Hines says that such an adaptation would not change the fundamentals of the DST.

Before details of the DST can be given, one must first expand upon definition it uses almost exclusively - *introwaves* and *extrowaves*. These are needed for matters determining the sense of mean-flow drag. To illustrate this point, consider a collection of eastward moving waves, as viewed from a ground-based reference frame. It is not the direction of propagation of the waves in this frame which determines the direction of the forcing on the mean-flow, but the direction of propagation of the waves as viewed from a *wind-borne* reference frame. Any mean-flow forcing is done so as to push the flow towards the phase velocity of the breaking waves.

Extrowaves are defined as those waves whose projected velocities in the direction of the background wind (ground reference frame) do not change sense when measured in the wind-borne frame. In contrast, *introwaves* do change their sense of direction. This has implications for modelling, in that if a spectrum of waves is thought to originate from processes where the local background winds are zero, then the waves at some greater height will all be extrowaves. Once defined, a wave can not change wave-type. If such a change were to occur, then by implication, the wave would of survived an approach to a *critical* level where the phase velocity of the wave matches the the velocity of the background wind, in the direction of wave motion. This is not allowed. Such a distinction defines a *critical circle* (see 4.5) dividing in velocity space the two kinds of waves. Generally, waves lying on the circle are obliterated by critical level processes. However, this does not apply to waves with zero phase velocity (those which lie at the origin of 4.5) (ground frame). Orographic waves are in this class and although they have zero magnitude on this diagram, do nevertheless have a direction in the intrinsic (wind-borne) frame. It is this frame which determines where any momentum would be deposited upon obliteration of the wave.

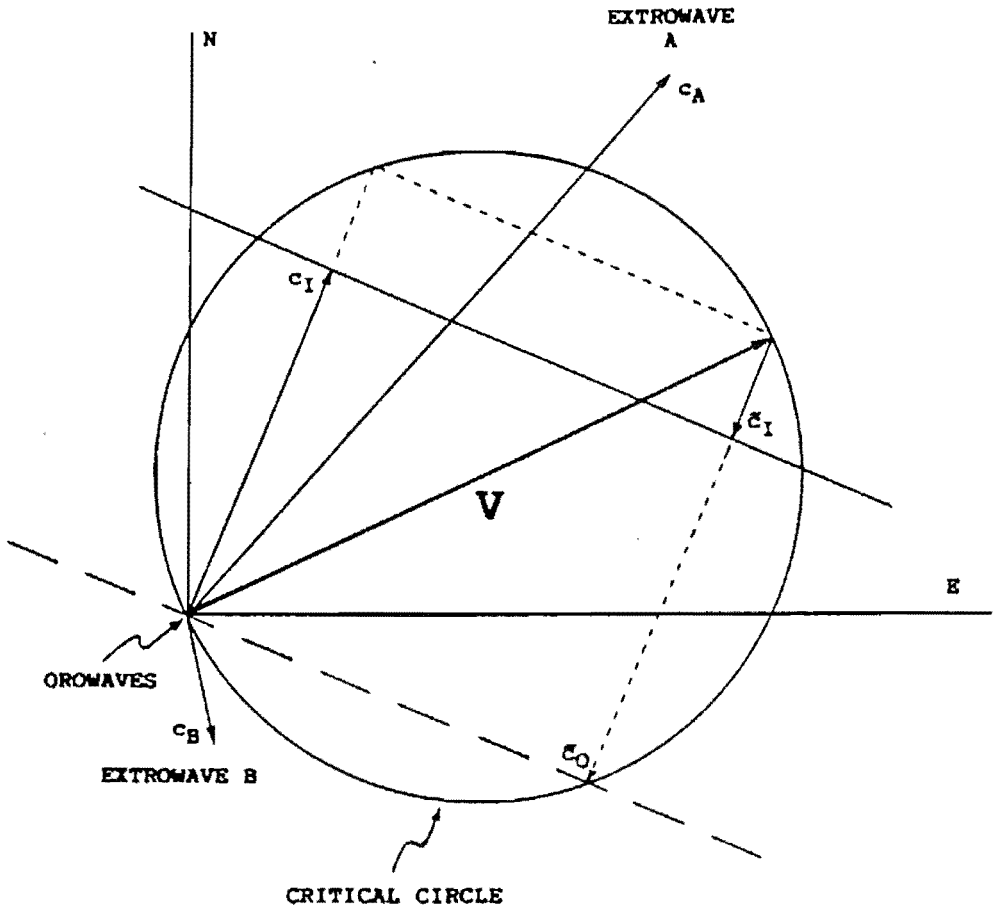

Figure 4.5: Introwaves and Extrowaves. Critical circle in velocity-space separating introwaves and extrowaves. The circle's diameter is determined by the magnitude of the velocity of the background wind (ground based). Vectors c_A and c_B depict extrowaves - those waves whose sense of direction do not change when moving from the ground-based to the intrinsic frame. Wave c_I represents an introwave. Its sense changes between the two frames ($\tilde{c}_I$). Oro-waves are located at the origin of the plot [from *Hines* (1997a).

4.2.1 Broad Spectrum

The DST first assumes a spectrum of upwardly propagating waves whose relative intensities are minor compared with the speed of the slowest waves in the spectrum and with the background wind. This corresponds to the low m end of power spectra where the shape and magnitude of the spectra are not bounded by theory. This incident spectrum is terminated at some wavenumber m_c corresponding to the *knee* of power spectra (that part of the spectrum having the greatest intensity). The magnitude of this part of the spectrum is constrained by observation and is usually taken to correspond to a wind variance of $\sim$1 m^2s^{-2} at tropospheric heights. The shape is somewhat less known. As the low end of the m-spectra corresponds to vertical scales of tens of kilometres, it is more than likely not possible to observe this part of the spectrum within the confines of the troposphere. As such, the slope of this part of the spectrum is taken so as to simplify the

calculations of the DST. Thus slopes of 1,3/2,... are generally used (a slope of 1 is taken for this study). The value for m_c is taken to be,

$$m_{ji} = \frac{N_i}{\Phi_1 \sigma_{ji} + \Phi_2 \sigma_h}, \tag{4.4}$$

where m_{ji} is the initial cutoff wavenumber for the incident spectrum of waves travelling in the jth direction, σ_{ji} is the initial value of the rms wind fluctuation as projected in the jth direction (contributed from waves in non-orthogonal directions), σ_h is the total wave deviance of all waves (of the broad spectrum) travelling in all directions and Φ_1 and Φ_2 are fudge-factors whose values are constrained by the DST. The first term in the denominator of equation 4.4 refers to the action of waves producing a Doppler shift in m of those waves having scales towards the tail of the spectrum where such effects are thought to exist. The second term represents instability in the spectrum as a whole. This can be likened to the instability criterion for monochromatic waves (*Lindzen* (1981)) whereby instability is attained when the rms wind fluctuation of the individual wave is comparable to the speed of the background flow. However, in the DST this instability is not restricted to one wave alone. The values for σ_{ji} and σ_h are,

$$\sigma_{ji}^2 = \sum_{p=1}^{J} \hat{\sigma}_{pi}^2 \cos^2(\alpha_p - \alpha_j), \tag{4.5}$$

$$\sigma_h^2 = \sum_{j=1}^{J} \hat{\sigma}_{ji}^2. \tag{4.6}$$

It has been assumed that a set of spectra are propagating in each of J directions. $\hat{\sigma}_{ip}^2$ represents the fluctuating wing arising from those waves travelling in the jth direction, only. While the angles denote the angular separation of the different *azimuths*.

Probably the most important factor determining the amount Doppler shifting of high m waves is the background wind. At heights above the height of the spectrum's prescription (that height where one arbitrarily assumes the form and intensity of the incident spectrum), the DST introduces a wind term to predict further values of m_c,

$$m_j = \frac{N_i}{\Phi_1 \sigma_j + \Phi_2 \sigma_h + V_j - V_{ji}}. \tag{4.7}$$

where the first V term denotes the background wind (as measured in the ground-based frame) in the jth direction at some height above the initial height i. The value of σ_j (and σ_h) will be determined from the increase in height of the propagating spectrum of waves (which will tend to increase it) and the reduction of the cutoff wavenumber m_j corresponding to a systematic reduction of the incident spectrum as waves having an original m greater than m_j are removed through critical layer processes. The size of σ_j is

given by,

$$\sigma_j^2 = \frac{\rho_i N}{\rho N_i}\hat{\sigma}_{ji}^2 \int_0^{m_j} \frac{\mathcal{M}(m)}{1-(V_j - V_{ji})m/N_i} dm$$

where $\mathcal{M}(m)$ is the power spectral density of the incident spectrum. It is also seen that at a particular height, $\hat{\sigma}_j^2$ is dependent on m_j at the same height, however m_j is dependent on $\hat{\sigma}_j^2$, through the projected wind deviance σ_j. To reconcile this, an iteration to self-consistency must be made to refine the two parameters' values.

Momentum deposition and associated wave heating is calculated from the decrease in m_j at successive heights. Thus the momentum flux remaining in the spectrum propagating in the jth direction is,

$$F_j = \rho_i \hat{\sigma}_{ji}^2 k_j \int_0^{m_{ji}} \frac{\mathcal{M}_{ji}}{m_i} dm_i. \tag{4.8}$$

Where k is the horizontal wavenumber associated with the spectrum. It is taken to be constant with height for each of the waves in the spectrum. For this study it is also constant for different azimuths of propagation. The amount of mean-flow forcing is then determined via equation 3.5.

The rate of intrinsic energy deposition (resulting in wave heating) is taken to be,

$$\frac{d\mathcal{E}}{dt} = -\Phi_5 \sum_{j=1}^{J} \frac{dF_j}{dz}(\Phi_1 \sigma j + \Phi_2 \sigma_h) \tag{4.9}$$

where Φ_5 is another fudge-factor with a value between one and three. It should be noted that this expression differs from that in *Hines* (1997a,b). The correction will lead to a change in the heating rate by a factor of three to five. However, it is doubted whether such an alteration will change an otherwise small heating contribution (*Hines*, pers. com.).

4.2.2 Quasi Monochromatic Waves: Ridge-Type Terrain

As laid out in *Hines* (1997b), the DST uniquely caters for the interaction between monochromatic waves and those within a broad spectrum. As such, one has a setting to investigate whether the two sorts of waves have a significant effect on each other. Other schemes, up until recently, have employed either separate broad spectrum and monochromatic parameterisations, or a combination of the two. The DSP and that of *Medvedev and Klaassen* (1995) (section 4.3) are two schemes which purport to capture some of the physics behind an interaction between the two sets of waves.

As mentioned earlier (section 4.2), gravity-waves generated from flow over topographic obstacles are special in the sense that they lie on the critical circle where such waves would normally undergo dissipation. Their effect on the mean flow is always to produce a drag

(deceleration) and so behave like *introwaves*. Thus their limiting direction of travel in ground based frame is into the upwind half-space (although one must remember that they have approximately zero phase velocity in this frame). Their vertical wavenumber at ground is constrained by the dispersion relation to be,

$$m_g = -\frac{N_g}{V_{Rg}} \tag{4.10}$$

where V_{Rg} is the projection of the background wind in the limiting direction of travel of the wave - so it is necessarily negative. The average upward flux of horizontal momentum takes the form,

$$F_{Rg} = -\Phi_R k_R \delta^2 2_R \rho_g N_g V_{Rg}. \tag{4.11}$$

The form of this equation is dependant on the nature of the terrain generating the waves. To accommodate the variety of terrain types, one is at liberty to alter the factor Φ_R. Values are thought to range from $0.2 \leq \Phi_R \leq 2.0$ for most terrain types. For this study a similar expression for the momentum flux from *Bacmeister* (1993) was used instead. There, Φ_R and k_R are replaced by the parameters α and L, respectively (refer to 4.1 and associated text). Likewise, the topographic variance δ^2 has been approximated as that for saturated values, namely $\delta^2 = V^2/N^2$.

The horizontal wind variance at ground is taken to be,

$$\hat{\sigma}^2_{Rg} = \Phi_R N_g^2 \delta_R^2 \tag{4.12}$$

which is approximately equal to the background wind when one assumes saturated values for δ_R^2. During conservative upward propagation, one obtains an expression for the orographic wind variance from a previous level by equating the momentum flux (which is conserved) between the two heights, obtaining,

$$\hat{\sigma}^2_R = \frac{\rho_i N V_{Ri}}{\rho N_i V_R} \hat{\sigma}^2_{Ri}. \tag{4.13}$$

The i subscripts refer to parameter values at some lower level; either the ground (for atmospheric models), some higher level, or the level at which the wave last diminished through critical layer processes. Such levels are found whenever the wave variance is above some maximum permitted value. Non-interacting monochromatic waves start to dissipate when they become comparable in magnitude to the background wind (in the direction of travel of the wave). In DST, such a level is reduced by the effects of the waves of the broad spectrum (and any *other* oro-waves). Namely,

$$\sigma^2_{RM} = \frac{1}{3}\left(-V_R - \Phi_1 \tilde{\sigma}_R\right)^2. \tag{4.14}$$

σ^2_{RM} represents an upper bound limiting further growth of the oro-wave with increased height. If ridge-type terrain is not used, or if there is some other source of quasi-monochromatic (QM) waves contributing to the number of such waves in a given region, then the presence of this (these) waves(s) predisposes the other waves to instability. The DST accounts for this effect by scaling the above equation by the number of oro-waves located in the same region, reducing the maximum permissible wind variance of each of the waves in the azimuth in question. The second term in the brackets represents that part of the background wind attributable to other waves having an influence in the direction (azimuth) of the wave (although it is not a true wind in the sense of that of the mean flow, but, nonetheless, having a statistical effect on the oro-wave). Thus, $\tilde{\sigma}_R$ is the contribution of wind fluctuations from all non-orthogonal azimuths,

$$\tilde{\sigma}^2_R = \sum_{j=1}^{J+?} \hat{\sigma}_j \cos^2(\alpha_j - \alpha_R). \tag{4.15}$$

The notation (as from *Hines* (1997b)) indicates those contributions from waves - both from the broad spectrum and *other* oro-waves (J+?), to the total wind variance in the R-azimuth[3].

Not only do each of the oro-waves induce instabilities in each other they also act to Doppler shift and destabilise the broad spectrum. As each of these effects are related to σ_j and σ_h respectively, some modification must be made to these. The first is most easily modified by inclusion of the oro-waves variance projected appropriately into the direction under consideration. That is,

$$\sigma^2_j = \sum_{p=1}^{J+!} \hat{\sigma}_p \cos^2(\alpha_j - \alpha_p), \tag{4.16}$$

following again the notation used in *Hines* (1997b). The limit of J+! indicates that *all* contributions from the different waves are to be included. It must be remembered that this parameter is used to determine the amount of Doppler shifting of waves from the broad spectrum in the *jth* azimuth. Unlike QM-waves, waves of the broad spectrum *can* interact non-linearly with other waves in their azimuthal spectrum.

An increase in instability of the broad spectrum is achieved by modulating the the size of Φ_2,

$$\Phi_2 \rightarrow \Phi_2 \exp\left(\frac{\pi}{N^{-2}} m^2_R \hat{\sigma}^2_R\right). \tag{4.17}$$

This expression includes only the contribution from one oro-wave, however, in general one should include a summation of all such waves - achieved in practise by summing

[3]It should be noted that this summation does not include the contribution from the oro-wave under examination. It cannot interact non-linearly with itself and thus induce instability.

subscripted terms above.

For purposes of calculating drag and heating rates, one need only include the contribution for each QM-wave. This is effectively done by adding the waves' momentum fluxes to expressions 4.8 and 4.9. Finally, it should be stated that the value of σ_h should not be altered with the inclusion of any oro-waves. Their effects have already been included 4.17.

The most important aspect of the treatment of oro-waves is that 4.13 should never be allowed to grow greater than 4.14. Once this occurs, 4.14 should be used until either 4.13 should become smaller or until the wave has totally dissipated. It has been mentioned that once 4.14 becomes operative, one could continue to use this expression for the oro-wave's variance. However, as intimated in *Hines* (1997b) and as found in this study, spurious generation of momentum fluxes can and do occur.

4.3 Medvedev and Klaassen

The Medvedev and Klaassen parameterisation of gravity wave saturation and drag attempts to combine aspects of non-linear wave-diffusion as put forward by *Weinstock* (1990) and Doppler spreading effects (c.f. DST). As such, waves of sufficiently high wavenumber lose energy through diffusive type processes, damping their magnitude as they propagate upward. Doppler shifting of the waves is assumed. However, unlike the DST, only those waves of higher wavenumber and thus lower intrinsic frequency than a particular wave in the spectrum, are permitted to do this. This is to be contrasted with the DST which allows the full spectrum to Doppler shift individual waves within. Like DST, it reproduces the saturated *tail* of power spectra from an arbitrary source and also approximates the results of Lindzen (*Lindzen*, 1981) for narrow spectra. One advantage it has over the DST are the number of *tunable* parameters it employs. Like the DST and all other non-orographic schemes it has to approximate the size and makeup of the unsaturated portion of power spectra incident at tropospheric heights. It currently employs (like the DST) a *modified Desaubies* spectrum, having the form,

$$\mathcal{M}(m) = A_0 \frac{\mu^s}{1+\mu^{s+t}}, \qquad \mu \equiv \frac{m}{m_*}. \tag{4.18}$$

Here, μ and m_* are vertical wavenumbers, with the latter being the characteristic wavenumber - indicating that part of the gravity-wave spectrum having the greatest energy (commonly refereed to as the *knee* in power spectra). The value of t is usually put around 3, while s is confined to within the range $0 \leq s \leq 1$ (modified Desaubies, s=1). Unlike the large m tail which is thought to be defined in strength and shape by the process(es) of saturation, the low m end is defined by the processes which go into generating it. The

value of A_0 can be estimated from observations of the saturated large m end using typical tropospheric values of m_* (*Smith et al.* (1987); *Allen and Vincent* (1995); *Tsuda et al.* (1989); *Fritts and Chou* (1987)). An upper bound for vertical scales associated with m_* (at tropospheric heights) is $\sim 2km$. It has just one other tunable parameter[4], that being the horizontal wavenumber of the wave-spectrum. It assumes there to be no variation in this with direction (a valid assumption when considering an isotropic source) and height. However, it is used in most parameterisations to limit (control) the amount of wave-drag.

Once a form for an incident spectrum is chosen, their parameterisation determines the amount of drag (if any) from dissipating waves from the rate of change, with height, of the prescribed power spectral density (PSD), namely,

$$\frac{d\mathcal{M}(m)}{dz} = \left(-\frac{1}{\rho}\frac{\partial \rho}{\partial z} + \frac{1}{m}\frac{\partial m}{\partial z} - \beta\right). \tag{4.19}$$

The first term represents an increase in spectral intensity due to decreasing air density and is equal to $-1/H$. The second gives the effects due to Doppler shifting due to the background wind and waves of smaller scale, while the third attempts to quantify the the interaction of waves in the spectrum with others of smaller scale (producing a damping of the former).

The coefficient for non-linear damping, β, has the form,

$$\beta = \frac{\sqrt{2\pi}N}{\sigma}\exp(-\alpha^2) \tag{4.20}$$

σ denotes those wind fluctuations arising from waves in the spectrum of smaller scale, to the wave under examination and so lower frequency. It found by integrating the PSD across all waves having larger m,

$$\sigma^2 = \int_m^{m_{max}} \mathcal{M} dm'. \tag{4.21}$$

The factor α is flow dependent and is sensitive to changes in the strength of the wave spectrum and the wave's intrinsic velocity, $c - \bar{u}$,

$$\alpha = \frac{N}{\sqrt{2}m\sigma} = \frac{c-\bar{u}}{\sqrt{2}\sigma}. \tag{4.22}$$

The variation in the vertical wavenumber with height can be found by examination of B.12 and takes the form,

$$\frac{N}{m} = \frac{N_i}{m_i} - \Delta\bar{u}, \tag{4.23}$$

where the subscript denotes the values of parameters at some previous height, while $\Delta\bar{u}$

[4]The DST has six.

is the wind shear between those heights.

Once values for $\mathcal{M}(m)$ and $\beta(m)$ have been found for each of the discretised wave components of the spectrum, a profile of wave drag can be worked from a summation of the drag for each of them.

$$a = \sum_{m=1}^{m_{max}} \frac{\mathcal{M}(m)\beta(m)k}{m}. \tag{4.24}$$

This expression for wave drag represents the total contribution of each of the components of the discretised spectrum. A further summation should be done for other wave-spectra propagating in other directions. As can be seen, the horizontal wavenumber k is used to modulate the magnitude of drag.

It should be noted that orographic waves can either be added separately (obeying some Lindzen type parameterisation), or can be introduced easily as one of the waves in the spectrum.

4.4 The Ultra-Simple Spectral Parameterisation

4.4.1 Source spectrum

The Ultra-Simple Spectral Parameterisation (USSP, *Warner and McIntyre* (1999)) considers the vertical evolution of a prescribed spectrum of gravity-waves. It does this by first modelling Doppler-shifting following passage through wind shear, then wave-breaking by imposing an idealised ceiling function - replacing those parts of the spectrum having an energy density (or momentum flux density) greater than that of the function. The scheme has been streamlined for use in GCMs by simplifying the form of the prescribed incident spectrum and the processes thought to limit the growth of the waves with height.

The current scheme assumes hydrostaticity and ignores the Coriolis force. As such, it does not employ the full inertio-gravity wave dispersion relation (e.g. *Holton* (1992)) but a simplified one (3.2). A consequence of this is the preclusion of back-reflected gravity-waves whenever the waves' intrinsic frequency is Doppler shifted toward N. Also, dissipation from critical level processes are underestimated during times where the intrinsic frequency of waves approaches the Coriolis parameter, f. This approximation is also employed by the DSP and *Medvedev and Klaassen* (1995) theories. As such these schemes also suffer from an underestimation of atmospheric forcing under such conditions.

One further drawback of this scheme is the employment of two/three parts for the evolving spectrum. Through regions of positive shear (where the background wind increases in strength with height) it performs favourably as compared with a second scheme employing the full inertio-gravity wave dispersion relation (*Warner and McIntyre* (1999)). However, differences occur in regions of appreciable *negative* shear, where an extension to a third spectral part produces more sensible results.

Following the notation of *Warner and McIntyre* (1999) the initial spectrum has a two-part momentum-flux density given by;

$$\rho \mathbf{F}_p^{(2)}(z_1, m_1, \phi_j) = \begin{cases} 0 & \text{for } m_1 < m_{1cut} \\ \rho(z_1)\beta D(z_1) m_{1X11}^{-s-1} m_1^s \times 2\sin(\Delta\phi/2)\hat{\mathbf{k}}_0 & \\ \qquad \text{for } m_{1cut} \leq m_1 < m_{1X11} \text{ (1st part)} & \\ \rho(z_1)\beta D(z_1) m_{1X11}^{t-1} m_1^{-t} \times 2\sin(\Delta\phi/2)\hat{\mathbf{k}}_0 & \\ \qquad \text{for } m_{1X11} \leq m_1 < \infty \text{ (2nd part)} & \end{cases} \quad (4.25)$$

The subscripted 'one' refers to the values of the relevant parameters at an initial height z_1. The spectrum is assumed to be isotropic (but not necessarily so) and its direction of

propagation ϕ is discretised for parameterisation purposes (j directions). The factor of $2\sin(\Delta\phi/2)$ results from integration over the azimuthal sector $\Delta\phi$ and is centred about the direction denoted by the horizontal unit wavevector, $\hat{\mathbf{k}}_0$. The momentum flux density of the spectrum of waves at this height is a function of wavenumber m and angle. As stated, the spectrum has two parts and employs a small wavenumber cutoff, m_{1cut}. This is commonly used by other gravity wave schemes (e.g. *Hines* (1997b)) and is a result of our poor knowledge of this part of the spectrum. These two spectral parts have been given power law dependencies with the low-m part being linear in wavenumber while the second is given an m^{-3} form (fig. 4.6). These are separated for convenience by the characteristic wavenumber m_{1X11} whose notation will be explained later. The parameters s and t have values 1 and -3 respectively, while β is an empirical constant having the value $1.047\,x\,10^{-1}$. The function $D(z)$ was used in the original study by (*Warner and McIntyre* (1999)) for purposes of normalisation in comparison studies.

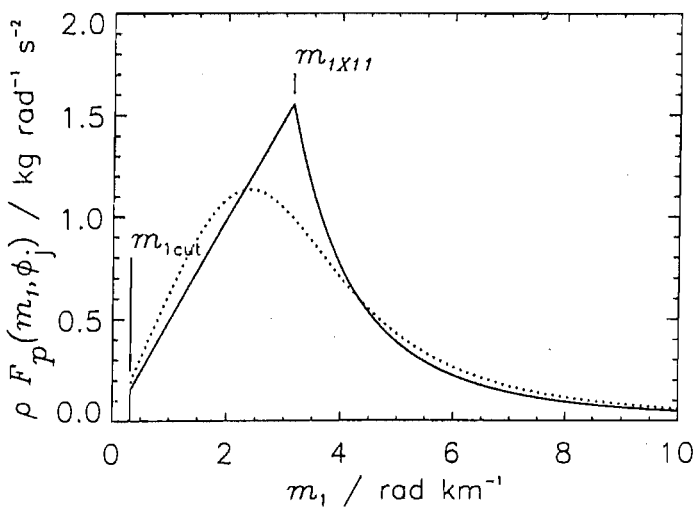

Figure 4.6: Two-part Spectrum. The two-part spectrum of the USSP. The small-m part of the spectrum is linear in m and represents that part of the spectrum propagating upward conservatively while the right-hand most one is constrained by a prescribed saturation spectrum. For comparison the dotted curve shows a spectrum modelled by *Fritts and VanZandt* (1993) (after *Warner and McIntyre* (1999).

4.4.2 Spectral Evolution

The evolution of the spectrum is controlled by conservative propagation and dissipation. The former is calculated using (3.2) and applying a spectral Jacobian, transforming 2D elements from (m_j, ϕ_j) space to (ω, ϕ_j), to the expression of the 2-D momentum flux. Thus,

$$dm = Jdm_1 = \frac{N_1 m^2}{N m_1^2} dm_1, \tag{4.26}$$

giving,

$$\begin{aligned}\rho\mathbf{F}_p^{(2)}(z,m,\phi_j) &= \rho\mathbf{F}_p^{(2)}(z_1,m_1,\phi_j)\frac{dm_1}{dm} \\ &= J\rho\mathbf{F}_p^{(2)}(z_1,m_1,\phi_j) \\ &= \rho\mathbf{F}_p^{(2)}(z_1,m_1,\phi_j)\frac{Nm_1^2}{N_1m^2}. \end{aligned} \tag{4.27}$$

Wave-breaking is then modelled by bounding the calculated momentum flux below some saturated level. That is, a second saturated expression for momentum flux replaces those parts of the spectrum, having a value above this second expression. This second spectrum has the form;

$$\rho\mathbf{F}_{pS}^{(2)}(z,m,\phi_j) = \rho(z)\beta D(z)m_{1X11}^{t-1}m_1^{-t} \;\times\; 2\sin(\Delta\phi/2)\hat{\mathbf{k}}_0. \tag{4.28}$$

Once the conservatively propagated spectrum has been 'chopped', replacing those parts of the spectrum having a value greater than (4.28) with this latter spectrum, one obtains the evolved spectrum at height z. The wavenumber m_{1X11} refers to the *cross-over* between the conservatively propagated part of the spectrum and either the saturated or imposed spectrum part. The lefthandmost subscript refers to the fact that the crossover wavenumber is at the launch height. The 'X' means crossover, while the other two indicate that the left/right parts adjacent to this crossover have a power law dependence at the launch height, respectively. This is important for calculations of momentum flux which require an integration over m (and ϕ_j) of (4.27) and (4.28). One can exploit an aspect of conservative propagation when calculating momentum fluxes at different heights. Imagine a particular 'chunk' of spectrum at one height being completely described by its spectral range in m and its shape (defined using one of either (4.27) or (4.28). After passage to some overlying height and consequent Doppler-shifting (4.23) of its spectral elements, the portion of spectrum will now have a different spectral range in m. However, the portion of spectrum will have the *same* momentum flux at the two heights (assuming no dissipation of the portion has taken place - no part has been replaced by (4.28).) This has the advantage of determining the momentum flux of the Doppler-shifted portion of the spectrum which may not be a simple power law after this process. Also, if part of the spectrum were to undergo dissipation and so be replaced by (4.28) at some wavenumber m_{zX1z} then one can still calculate the momentum flux of the remaining spectral portion by conservatively *back-propagating* the portion back to a height (generally the launch height) were its form is a simple power law and so can be integrated. The notation of the new cutoff wavenumber implies that it is at some height z and that the left/right parts have a power-law relationship at the launch and z heights, respectively.

In regions of positive shear, dissipation will occur continually, resulting in progressively

more of the incident unsaturated portion of the spectrum becoming saturated; or in terms of the USSP, being replaced by spectra having a saturated form at overlying heights. The procedure dealing with the positive wind shear case can be seen in (4.7). Panel (e), referred to as the back-propagated spectrum, is just what would be needed to produce panel (d) after conservative propagation. For this positive shear case the portion of the spectrum to the right of m_{zX1z} of panel (d) is integrated together with that portion to the left of m_{1X1z} of (e). These two wavenumbers refer to cutoff wavenumbers at the z and launch heights, respectively. Also, the $1z$ refers the fact that the portions of the spectrum either side of the cutoff wavenumber have power law dependencies at the launch (left) and z heights, respectively. Panels (d) and (e) have the same areas and so momentum fluxes. For the purposes of calculating these, one needs to find out the position of the cutoff wavenumber at one of these heights. The other can be found using (4.23). For this case calculating m_{1X1z} is faster than calculating m_{1X1z}. The converse is true for the negative shear case.

Through regions of negative shear there may not be dissipation at all (fig. 4.8) as the Doppler-shifted spectrum may be entirely below the imposed saturated spectrum. Also, when dissipation does set in, it may be due in part to decreasing air density resulting in growth of the spectral peak. This can lead to the imposed saturated spectrum *cutting* through the spectral peak. Without resorting to a third spectral part one would calculate an increase in momentum flux. Such an occurrence would correspond to an *increase* in calculated momentum flux. This cannot occur physically as it would imply the resurrection of parts of the spectrum already removed through saturation processes. Therefore in these situations a third spectral portion is adopted (fig. 4.9). The force per unit mass from the dissipating waves on the background air is just the density weighted vertical divergence of the momentum flux, summed over all directions.

$$\mathbf{a}(z) = -\frac{1}{\rho(z)}\frac{\partial}{\partial z}\sum_{j=1}^{n}\rho\mathbf{F}_p^{(1)}(z,\,\phi_j)\hat{\mathbf{k}}_0. \tag{4.29}$$

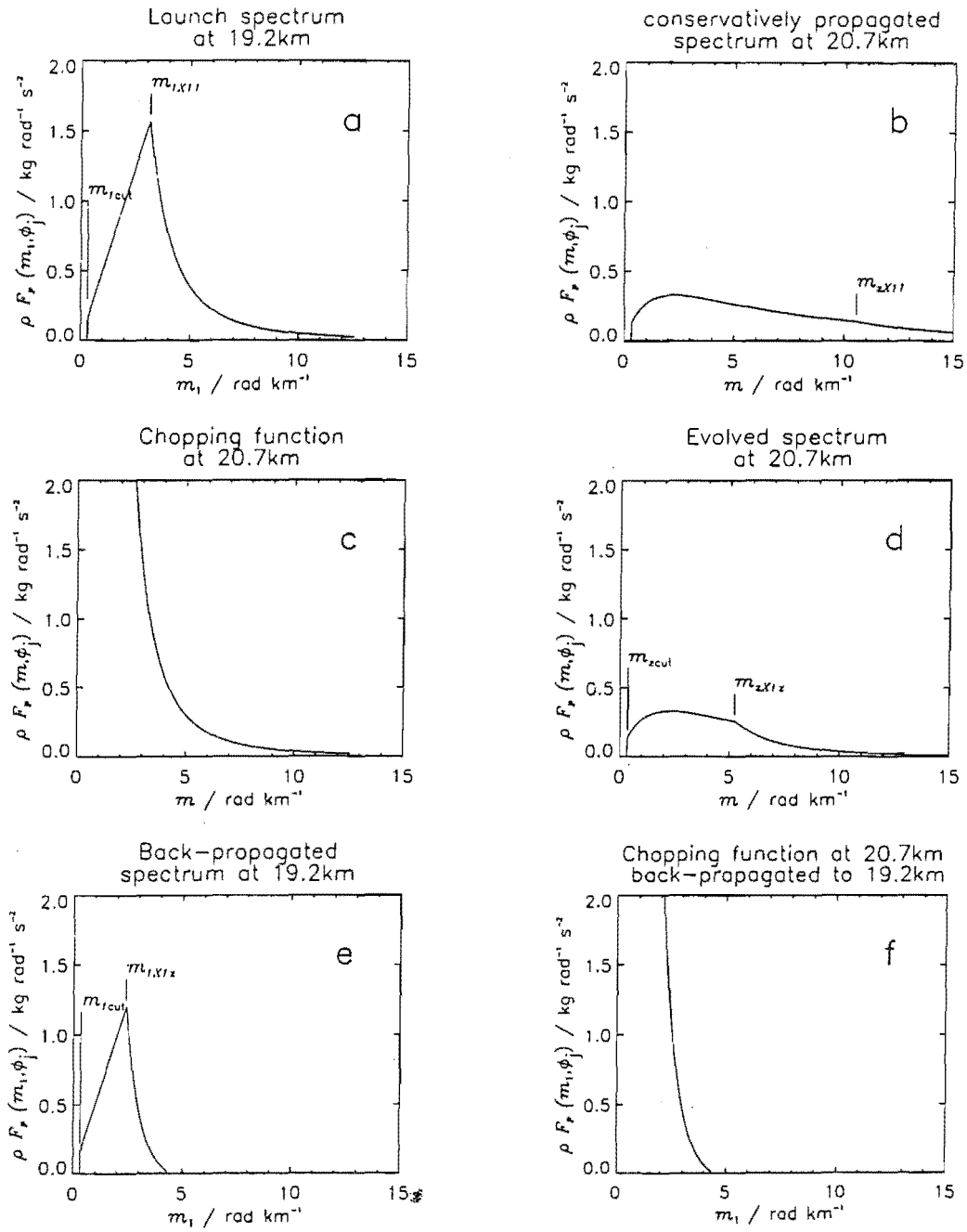

Figure 4.7: Positive-shear Case. Representation of the procedure to compute the spectral evolution of a prescribed set of gravity-waves through a wind shear of 5 $m\,s^{-1}$ (after *Warner and McIntyre* (1999))

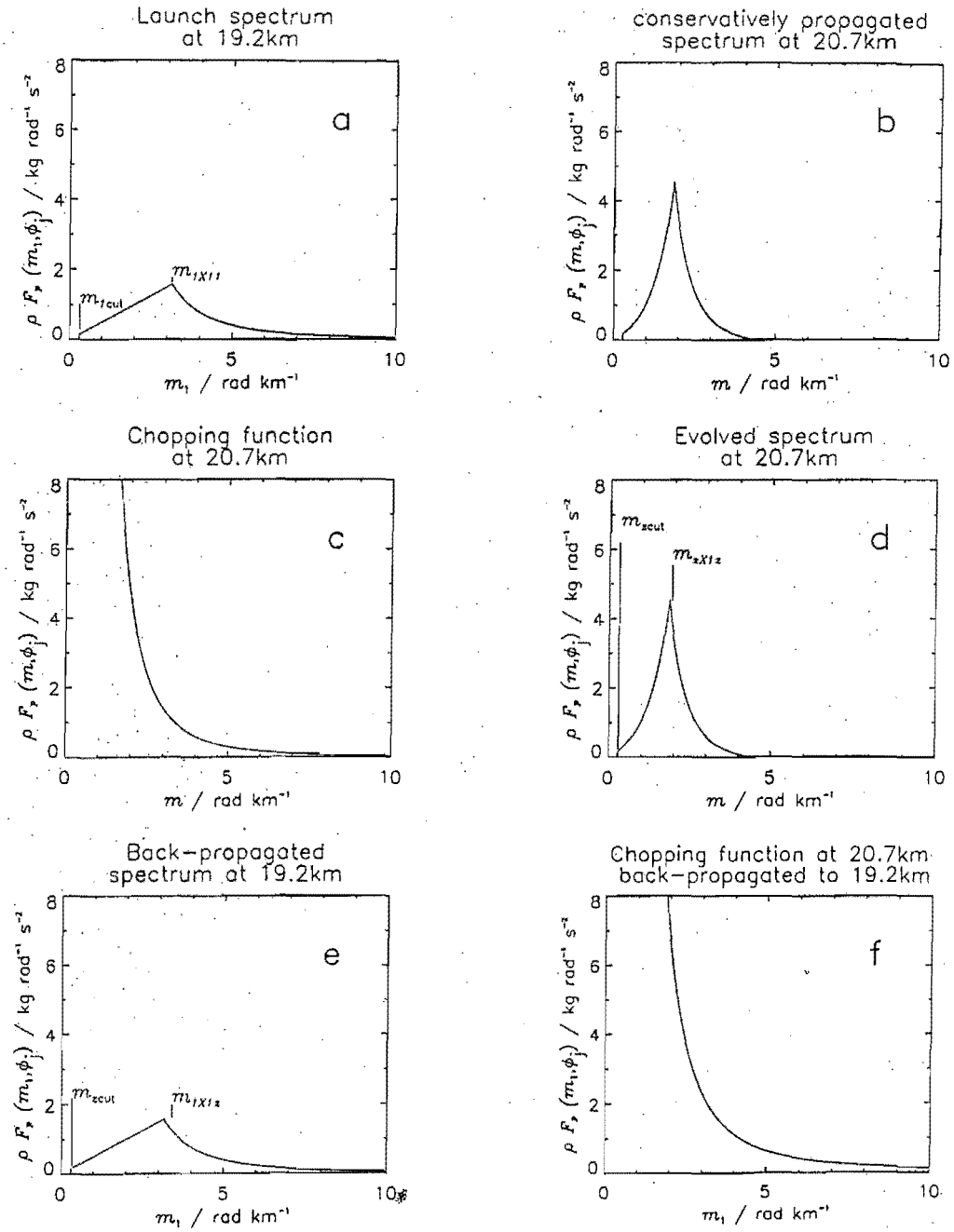

Figure 4.8: Negative-shear Case. Representation of the procedure to compute the spectral evolution of a prescribed set of gravity-waves through a wind shear of $-5\ m\ s^{-1}$ (after *Warner and McIntyre* (1999))

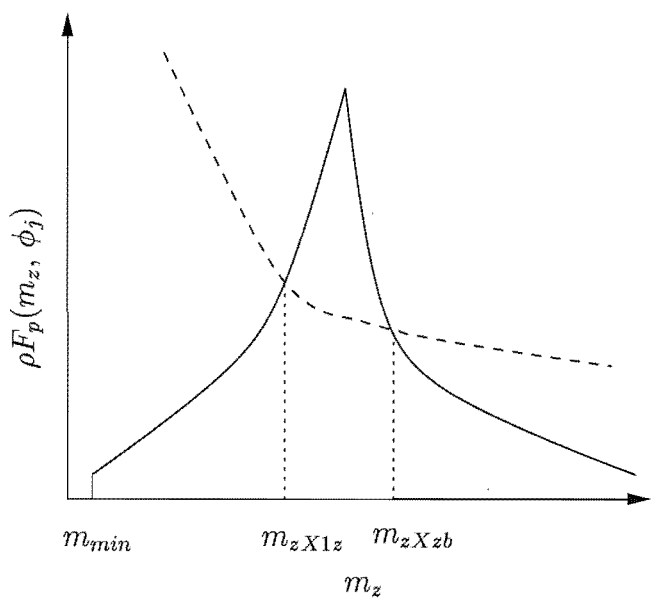

Figure 4.9: Three-part Spectrum. A three-part spectrum is adopted when the peak of the spectrum falls below the imposed saturation spectrum at some height. The two-part procedure predicts a momentum flux which is greater than previous heights to the right of m_{zXzb} (dashed line) where a lower saturation curve from some previous height b should be maintained (bold line).

Chapter 5

Single Column Tests

5.1 The Coupled Hines Scheme

To help gauge the relative importance of the two sources of gravity waves in the DSP (broad spectrum and orographic) and the extent of their mutual interaction, it is instructive to first run them through representative values of atmospheric parameters for different times of the year, in an offline manner. By this it is meant the parameterisation is not connected to an atmospheric model.

Before this is done various DSP parameters must be set. Unless stated otherwise, the source strength of the broad spectrum, denoted by the total wave wind variance σ_h, is taken to have the value 1 $\mathrm{m^2\,s^{-2}}$. The orographic wave is assumed to have a momentum flux of 10^{-4} Pa. This corresponds to a background wind blowing over the topography of 10 $\mathrm{m\,s^{-1}}$. It can be imagined that on occasions a much stronger wind could blow. The characteristic horizontal wavenumber of the broad spectrum is taken to be $2\pi/(900\text{ km})$ and the low m-end spectral shape is assumed to be of a modified Desaubies type with slope, s=1. The spectra employed also have a minimum vertical wavenumber of, $m_{min} = 1/3000$ m. There is much doubt about the composition of this portion of the spectrum and so it is commonly omitted from other implementations of the DSP. Two adjustable parameters which are used in the running of the parameterisation are the factors Φ_1 and Φ_2. These have values of 1.5 and 0.4 respectively.

Figure 5.1 shows typical values of temperature, wind and static-stability during winter and summer at mid-latitudes. The effect of an orographic wave on the waves of the broad spectrum is encapsulated by the term σ_j of the DSP and its inclusion is set out by the relation (4.16). Their effect is to destabilise those waves travelling with and about (but not orthogonal to) the orographic wave in question - thus reducing the magnitude of the cutoff wavenumber of the broad spectrum (equation 4.7).

Figure 5.2 describes the evolution of waves comprising a broad spectrum and an orographic wave during mid-latitude winter.

The orographic wave is taken to originate above some topography (mountain) and is directed westward. The broad spectrum of waves is taken to originate somewhere within the troposphere from some unspecified source. For future evaluation by comparison with online runs using the Stratosphere-Mesosphere Model (SMM), the broad spectrum is

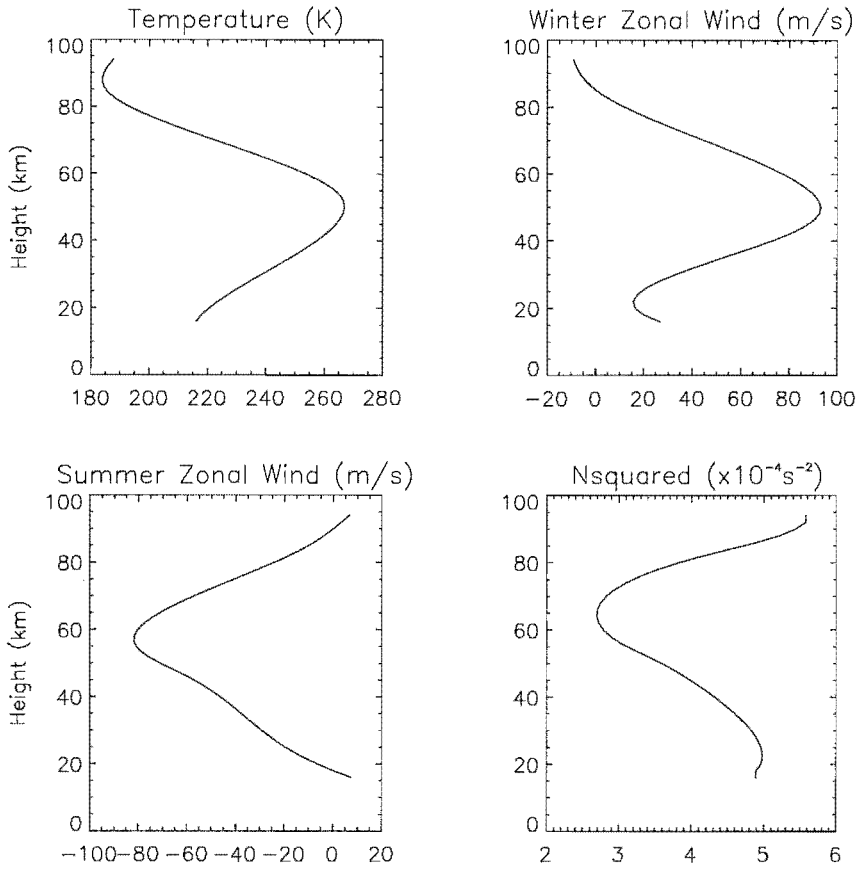

Figure 5.1: Typical mid-latitude values in the vertical of; temperature, wind and static-stability, during winter and summer.

assumed isotropic in direction at 16 km. It is seen that the wind variance associated with the orographic wave rises exponentially to about 65 km where a sudden attenuation of its strength coincides with the wave becoming saturated. The broad spectrum waves start out isotropic in extent about a zonal wind of approximately 28 $\mathrm{m\,s^{-1}}$. The background wind (fig. 5.1) is first seen to diminish and then rise above this value. As such, westward and then eastward travelling waves are dissipated over the next 10 km as witnessed by the broad spectrum zonal momentum flux at these heights. This dissipation of waves seen in the broad spectrum is not readily apparent in the drag profile due to the greater density of atmosphere at those heights. Peaking in magnitude at about the stratopause (50-60 km), the background wind then reduces to levels where more broad spectrum momentum flux is reduced as the remaining westward travelling waves undergo dissipation somewhere above 65 km. This coincides with the orographic wave reaching a critical level and undergoing dissipation. The growth of the oro-wave as witnessed by its wind amplitude, destabilises some of the westward travelling waves of the broad spectrum causing dissipation, as seen in the spike in the drag profile of the broad spectrum at the same altitude. This spike corresponding to a few m/s/day would be swamped by the drag from the orographic

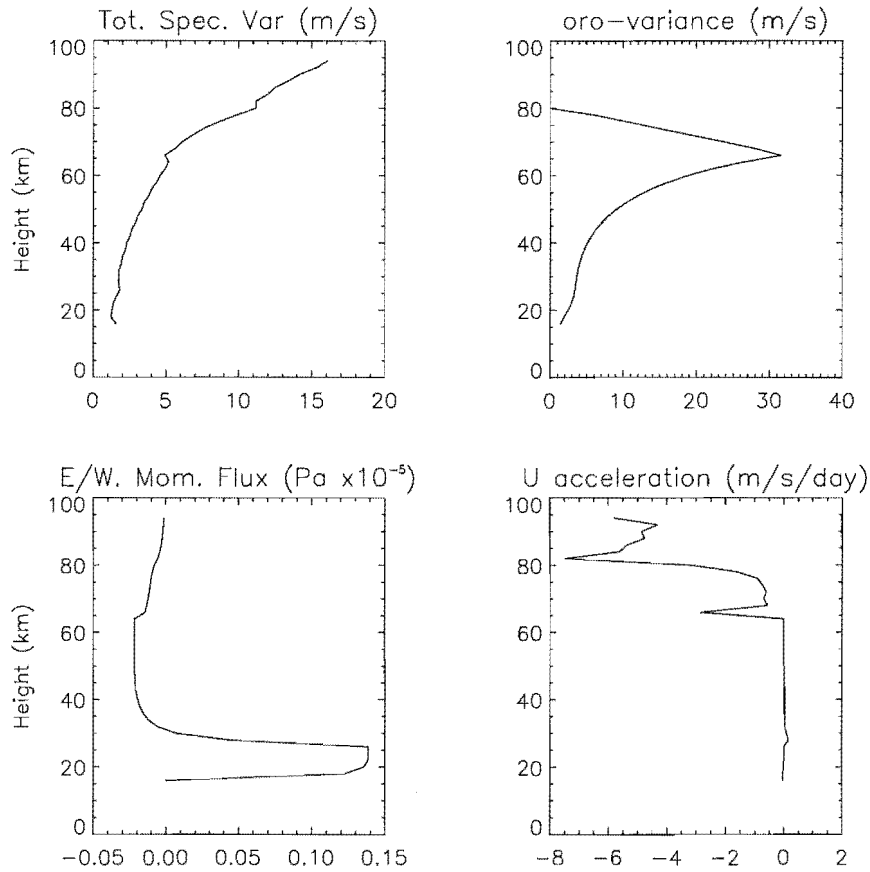

Figure 5.2: Vertical output of: total wind variance, orographic wind variance, zonal broad spectrum momentum flux and drag from the DSP during wintertime.

wave (not shown, but being several hundred to a thousand m/s/day), assuming an initial launch momentum flux of the orographic wave of 10^{-4} Pa[1]. It must be noted that the oro-wave has an equivalent effect on waves of the broad spectrum travelling opposite to it due to the squared cosine term in equation 4.16. Because of this, if the net zonal broad spectrum momentum flux had been directed opposite to the oro-wave, the associated drag would then have been similarly opposed.

Contrasted with this picture is what happens when the interaction is turned off (figure 5.3), which shows no such spike in the broad spectrum drag at 65 km. The change in broad spectrum momentum flux now occurs at heights above 70 km and is concomitant with the rise in drag of about 10 $\mathrm{m\,s^{-1}\,day^{-1}}$ at a similar level. This is solely linked with changes in the background wind, with the decreasing wind eliminating those westward propagating waves left propagating upward.

During summertime no noticeable effect of the coupling is seen. As the background wind reduces in strength and indeed changes sign at about 20 km, the orographic wave is destroyed. This is due to the wave's phase velocity being approximately zero - being

[1]This is calculated using equation 4.1, choosing $N \approx 10^{-2}$ Hz, $v_r \approx 10\ \mathrm{m\,s^{-1}}$ and $\rho \approx 1\ \mathrm{kg\,m^{-3}}$.

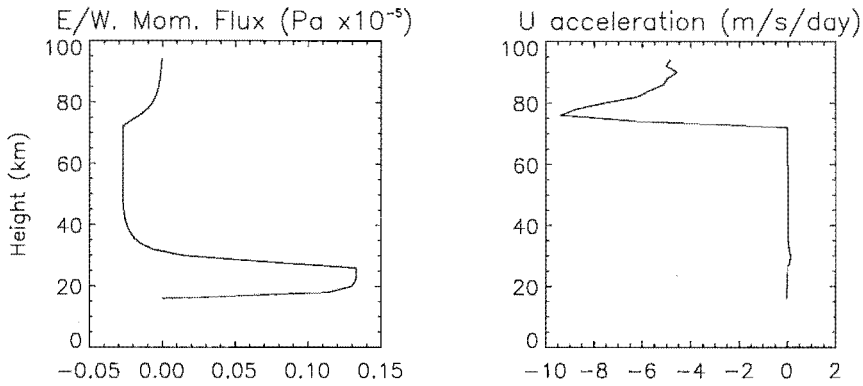

Figure 5.3: Vertical output of zonal broad spectrum momentum flux and drag from the DSP with no orographic interaction, during wintertime.

phase-locked with the topography below. The oro-wave cannot attain the same magnitude of wind amplitude as it could during the winter, where it could grow in response to the decrease in air density. As such, it can only attain a wind amplitude of several $\mathrm{m\,s^{-1}}$. Although the momentum flux of the broad spectrum is weighted heavier for waves travelling more slowly (with a low m-end incident spectral shape, $s = 1$), the oro-wave is still not strong enough to have any *lasting* effect on the distribution of broad spectrum momentum flux (fig. 5.4). Those features which are seen are due to most of the westward travelling spectral waves being removed through critical layer processes, as the background wind sweeps steadily westward from an initial value of about $10\ \mathrm{m\,s^{-1}}$ at 16 km. It should be remembered that the broad spectrum of waves starts out isotropically distributed at this height. A large spike in broad spectrum drag is seen below 80 km associated with a sizable decrease in wind variance from *all* waves of the broad spectrum. This is due to a combination of large total wind variance and positive background wind shear causing dissipation of the remaining eastward travelling waves left in the spectrum.

The negligible effect of the oro-wave on the waves of the broad spectrum during these times is finally confirmed in figure 5.5. No change is seen in zonal momentum flux of the spectra or its density weighted vertical gradient - drag.

Not only does an oro-wave engender instability (via Doppler-spreading) in waves travelling about its limiting direction of motion (refer 4.2.2), it also helps to destabilise *all* broad spectrum waves. This is carried out in the DSP by the vertical change in the parameter Φ_2, where its value is increased to effect greater dissipation of the broad spectrum, via an increase in the second term of the denominator in equation (4.7). Figure 5.6 shows the results of offline calculations where the parameter Φ_2 is varied as described in section 4.2.2 and where it is held constant at a value of 0.4, which would be the case if no oro-wave were present. Wintertime profiles for atmospheric quantities are assumed (so that the oro-wave has some effect on the broad spectrum, at least). It is seen that the parameter

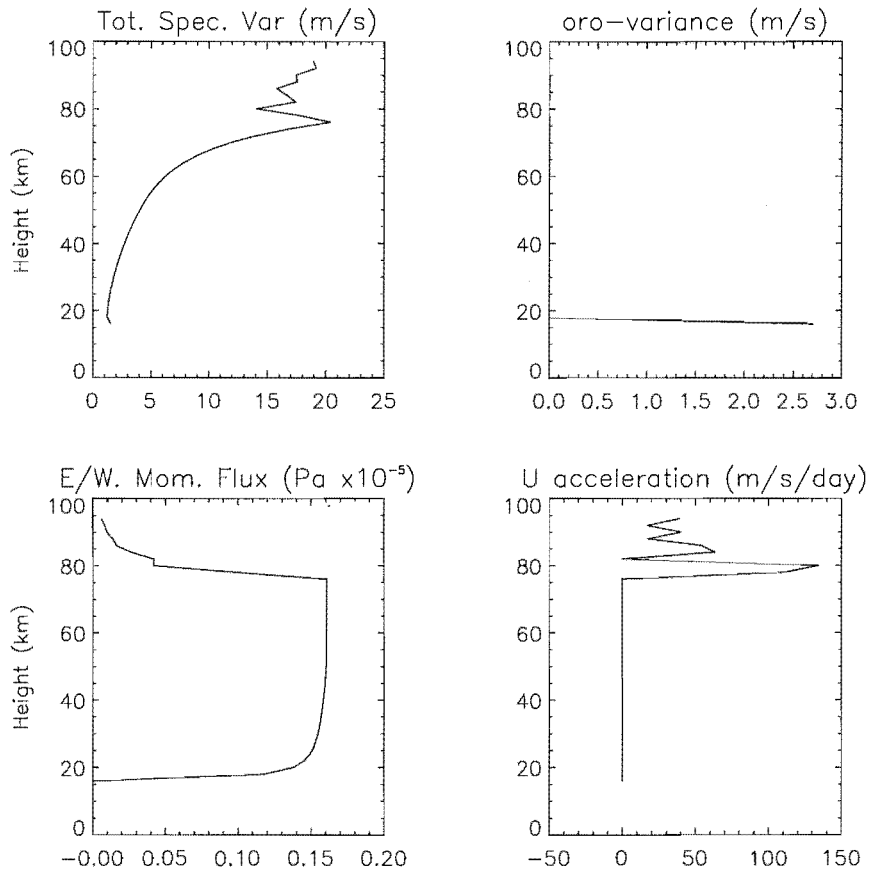

Figure 5.4: Vertical output of; total wind variance, orographic wind amplitude zonal broad spectrum momentum flux and drag from the DSP during summertime.

Φ_2 rises in accordance with the approach of the oro-wave to a critical level (where it is dissipated). The oro-wave's wind amplitude rises appreciably (refer fig. 5.2) and peaks around a height of 65 km where it becomes saturated and dissipates accordingly. This heightened wind amplitude affects the broad spectrum about the height of dissipation of the oro-wave, but does not appear to have any lasting influence on the broad spectrum above this. The extent of this destabilisation is seen by an increase in the broad spectrum drag at 65 km by a factor of about three. The size of this effect would be dependant on how anisotropic the broad spectrum was and also how close the background wind was to dissipating portions of the spectrum - it is the Doppler-shifting due to this which is dominant. These factors will determine whether such changes will compare in magnitude to the breaking oro-wave.

As it is the vertical shear in the background wind which dominates the evolution of both oro-waves and those comprising a broad spectrum, one further set of calculations was undertaken incorporating an idealised atmosphere having no wind shear. So that any oro-wave present would grow strong enough to have a noticeable effect on broad spectrum waves, it was decided not to have a *windless* atmosphere but one in which the size of the

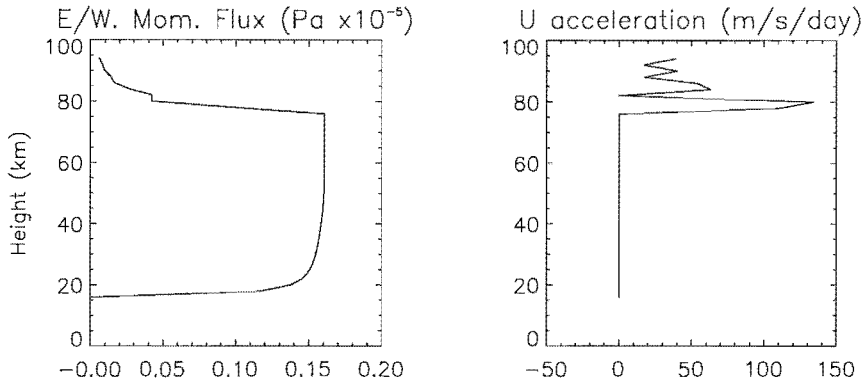

Figure 5.5: Vertical output of zonal broad spectrum momentum flux and drag from the DSP with no orographic interaction, during summertime.

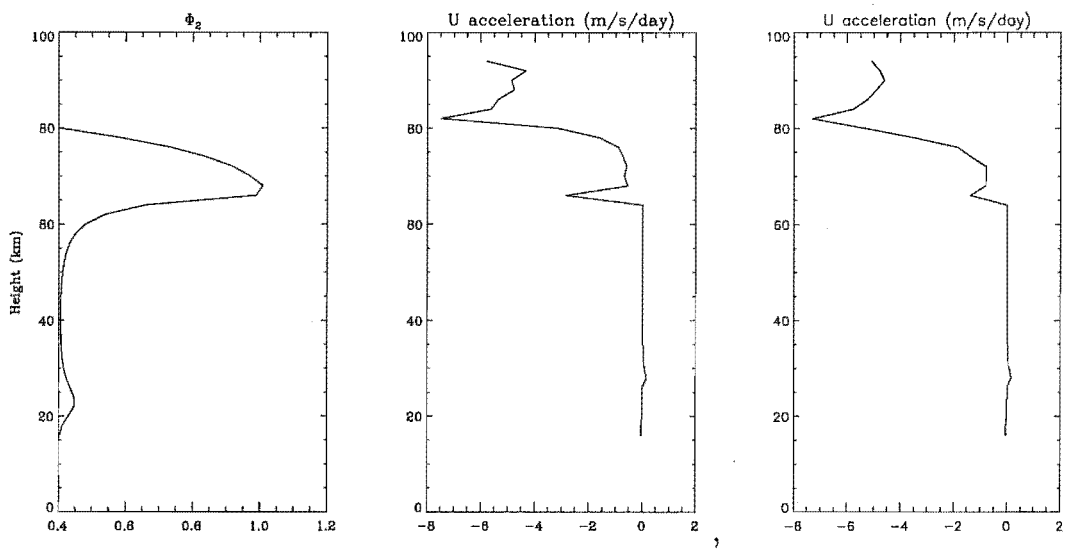

Figure 5.6: Wintertime vertical output of the parameter Φ_2 and broad spectrum drag incorporating a vertically varying/non-varying Φ_2, respectively.

wind would result in dissipation of an orographic wave at a height comparable to those seen for orographic waves during winter[2]. To achieve this, a value of 40 $\mathrm{m\,s^{-1}}$ was taken for the background wind.

Figure 5.7 represents output using an orographic source strength of 10^{-4} Pa and source broad spectrum variance of 1 $\mathrm{m^2\,s^{-2}}$. This corresponds to a momentum flux of the order of 10^{-6} Pa for any one of the 8 spectra isotropically distributed in direction. It is noticed that the difference in stratospheric momentum flux between waves travelling parallel with and orthogonal to the oro-wave is sizable - showing an approximate 30% difference in the lower stratosphere. Spectra in the orthogonal direction do not have any direct interaction with the oro-wave - only indirectly from interaction with spectra in other azimuths. The extent of the oro-waves effect on similarly directed spectral waves can be seen by looking

[2]There would be immediate dissipation of an orographic wave in a windless atmosphere.

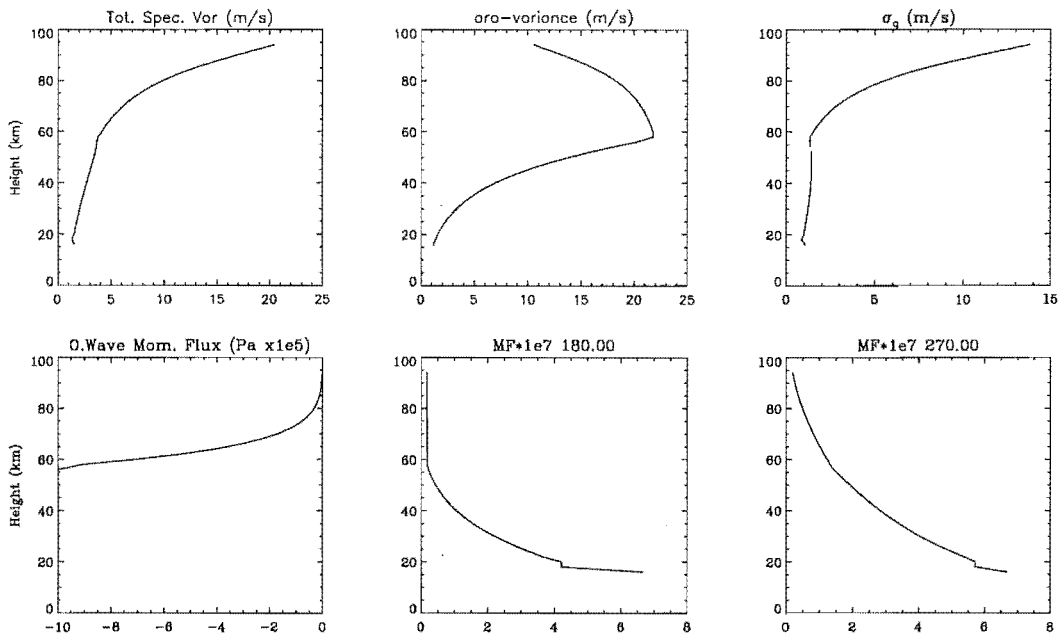

Figure 5.7: Vertical output of; total spectral wind variance, orographic wind variance, σ_q, orographic momentum flux and spectral momentum flux ($x10^{-7}$Pa) propagating parallel (180°) and perpendicular (270°) to the orographic wave, using a broad spectrum source strength of σ_h =1.0 $m^2\,s^{-2}$.

at the wind variance of waves travelling parallel with it - σ_q. This parameter has its origin in equation 4.15 and its magnitude determines the contribution from spectral waves to the orowaves eventual dissipation. Without the effects of wind (or an oro-wave), this should roughly increase exponentially in height. However, it is noticed that this does not occur as the oro-wave appears to restrict such growth. The monochromatic wave breaks down at about 56 km allowing waves from the broad spectrum (as denoted by both the total spectral variance, σ_h and σ_q) to again increase exponentially.

Figure 5.8 differs from the previous case in that a broad spectrum source strength of 4 $m^2\,s^{-2}$ is used. It is immediately noticed that the height of the critical level of the oro-wave is approximately the same as previously seen. This is a direct result of σ_q being restricted in size, even though the momentum flux (of spectra in orthogonal directions) has gone up by an order of magnitude. As before, waves of the broad spectrum are allowed to increase at a greater rate as soon as the oro-wave has dissipated.

Other tests which were undertaken have included reducing the strength of the orographic wave to 10^{-7} Pa; which is equivalent to a reduction in the mean wind blowing over the topography from 10 $m\,s^{-1}$ to 1 $m\,s^{-1}$. The height of dissipation of the oro-wave (not shown) increased to about 90 km. Varying the strength of the broad spectrum as before resulted in a reduction of this height by about 5-10 km. The effect on the broad spectrum was also reduced significantly - with differences in spectral momentum flux reducing to less than 1%.

A final set of tests were conducted using a varying number of azimuths for the broad

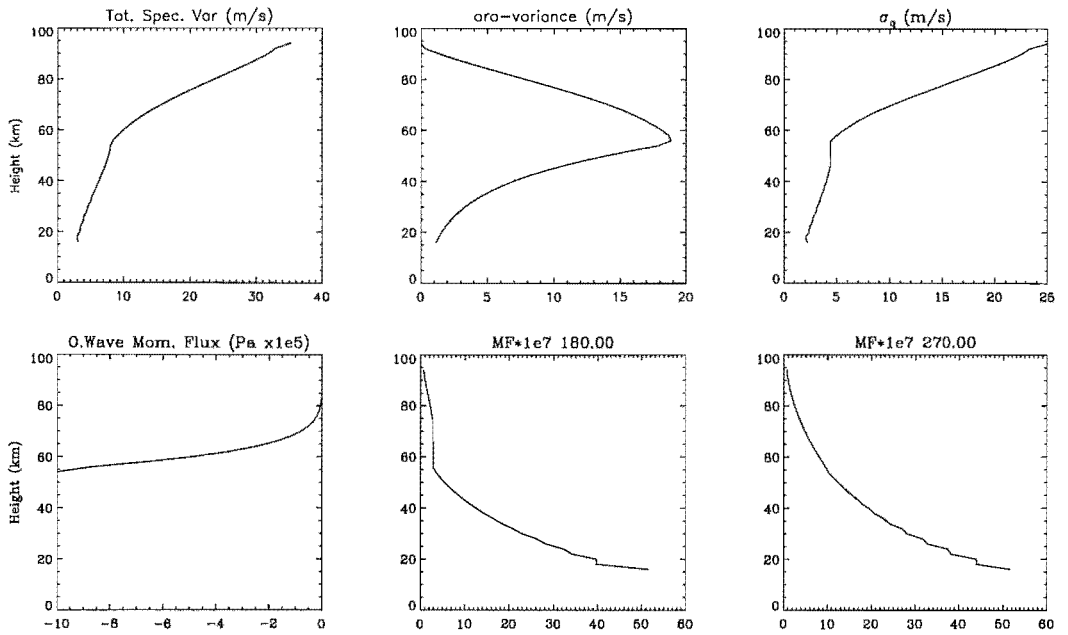

Figure 5.8: Vertical output of: total spectral wind variance, orographic wind amplitude, σ_q, orographic momentum flux and spectral momentum flux ($\times 10^{-7}$Pa) propagating parallel (180°) and perpendicular (270°) to the orographic wave, using a broad spectrum source strength of $\sigma_h = 4.0$ m^2 s^{-2}.

spectrum. The default for this study has been 8. Increasing this to 12 and 16 saw no appreciable difference in the context of these single column offline tests.

5.2 Comparison of Different Schemes

A major concern to modellers, second only to the choice in source, is the choice of which gravity wave parameterisation to use. Any parameterisation must deal with certain aspects of the phenomena they wish to represent and must necessarily emphasise some physics over others. Also, two different parameterisations may try and represent the same physics but may go about it in different ways. For example, two of the three schemes used in this study implicitly assume a continuous and broad spectrum source of waves. However, the third discretises a broad spectrum source. With these considerations in mind it would not be surprising if different schemes gave different results when included in atmospheric models. It is the purpose of this chapter to investigate whether any significant differences exist between the three gravity wave schemes previously described, in an offline environment - outside of an atmospheric model.

So as to associate any differences between the schemes with the physics they purport to represent, one must first construct a common source. With this in mind, representative values of atmospheric gravity wave activity were taken from the study of *Allen and Vincent* (1995). This was in the form of normalised temperature variances and were taken at different times of the year and for different latitudes. Times were taken to correspond

scheme	spectrum	$k_h(\mathrm{km}^{-1})$	$m_{min}(\mathrm{km}^{-1})$	m_{crit}	$\sigma_h(\mathrm{m}^2\mathrm{s}^{-2})$
DSP	continuous	$2\pi/900$	1/3	equation 4.4	1.0
MK95	discrete	$2\pi/900$	1/3	equation 4.4	1.0
USSP	continuous	$2\pi/900$	1/3	equation 4.4	1.0

Table 5.1: A summary of the source that was used for the three schemes; DSP, MK95 and the USSP. The parameters include; the characteristic horizontal wavenumber k_h, low wavenumber cutoff m_{min}, initial high wavenumber cutoff m_{crit} and total wave variance σ_h. The initial vertical wavenumber spectrum was of a modified Desaubies type with shape s=1.

to southern summer, equinox and winter (January, March and July, respectively) and geographic location chosen for tropical and extratropical atmospheric profiles (5°S and 35°S). CIRA86 data were used as representative zonally averaged profiles (Figure 5.9) of the extratropical atmospheric state. Output from the Stratosphere Mesosphere model displaying a *realistic* tropical atmosphere was used for a tropical profile. These temperature variances can be related approximately to wind variances (which are used as source input into the DSP and Medvedev and Klaassen (MK) schemes) by,

$$\bar{T'}^2 \approx \frac{N^2}{pg^2}\sigma_t^2. \tag{5.1}$$

Where N and g represent static-stability and gravitational acceleration, respectively. While σ_t^2 denotes the total gravity wave wind variance and p is a spectrum related parameter used in *Fritts and Lu* (1993). Once the spectral range (smallest and largest waves in the spectrum) and slope (modified Desuabies, s=1) were calculated a total spectral momentum flux can be found - this is used as input into the USSP. The spectra of all three schemes have a low-m (wavenumber) bound corresponding to wavelength scales of about 20 km. An upper-m bound is determined from the DSP (the associated high wavenumber cutoff) which is then *sent* to the MK and USSP schemes. As the DSP can only represent the low-m part of the spectrum (no saturated parts) the other two were necessarily truncated at this wavenumber. All incorporate a characteristic horizontal wavelength of 900 km and eight azimuths of propagation. This was to ensure that some of the nonlinear physics built into the DSP could occur. The MK spectrum was discretised into 100 parts. Table 5.2 shows the makeup of the relative input source spectra for each of the schemes.

An indication of the behaviour of the three schemes in the tropics can be seen during January in figure 5.10. The background wind shows alternating regions of positive and negative shear (increasingly eastward/westward winds) from the launch height (18 km) to about 100 km. The patterns of momentum flux seen for each of the schemes is remarkably similar, with the changing background profile of wind etching its distinctive pattern in the spectral profiles. The pattern displays the spectral momentum flux characteristics of

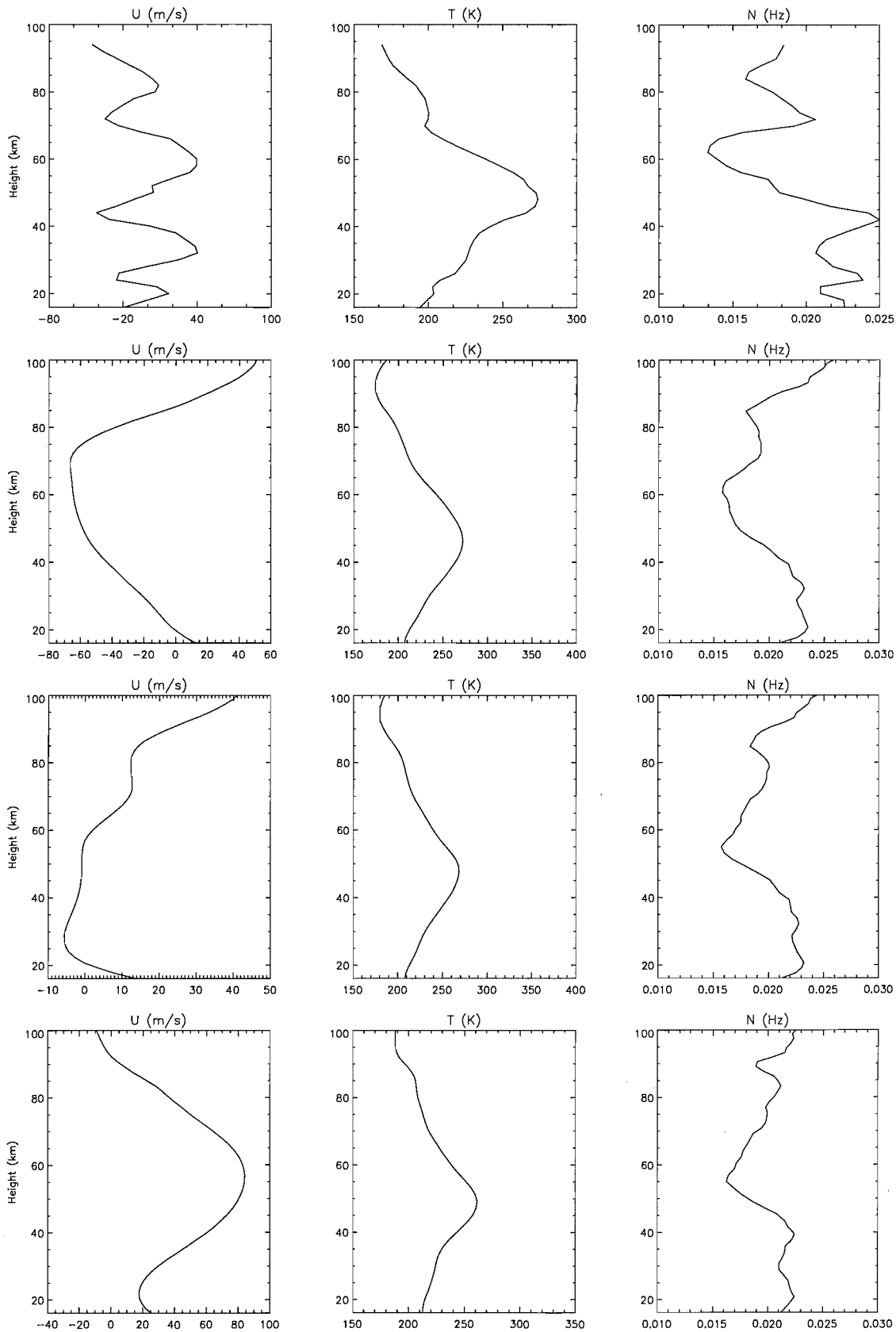

Figure 5.9: Single column profiles of zonal wind, temperature and static stability at latitude $5°S$, as output from the SMM during January (top figures) and at $35°S$ during January, March and July, from the CIRA86 dataset, respectively.

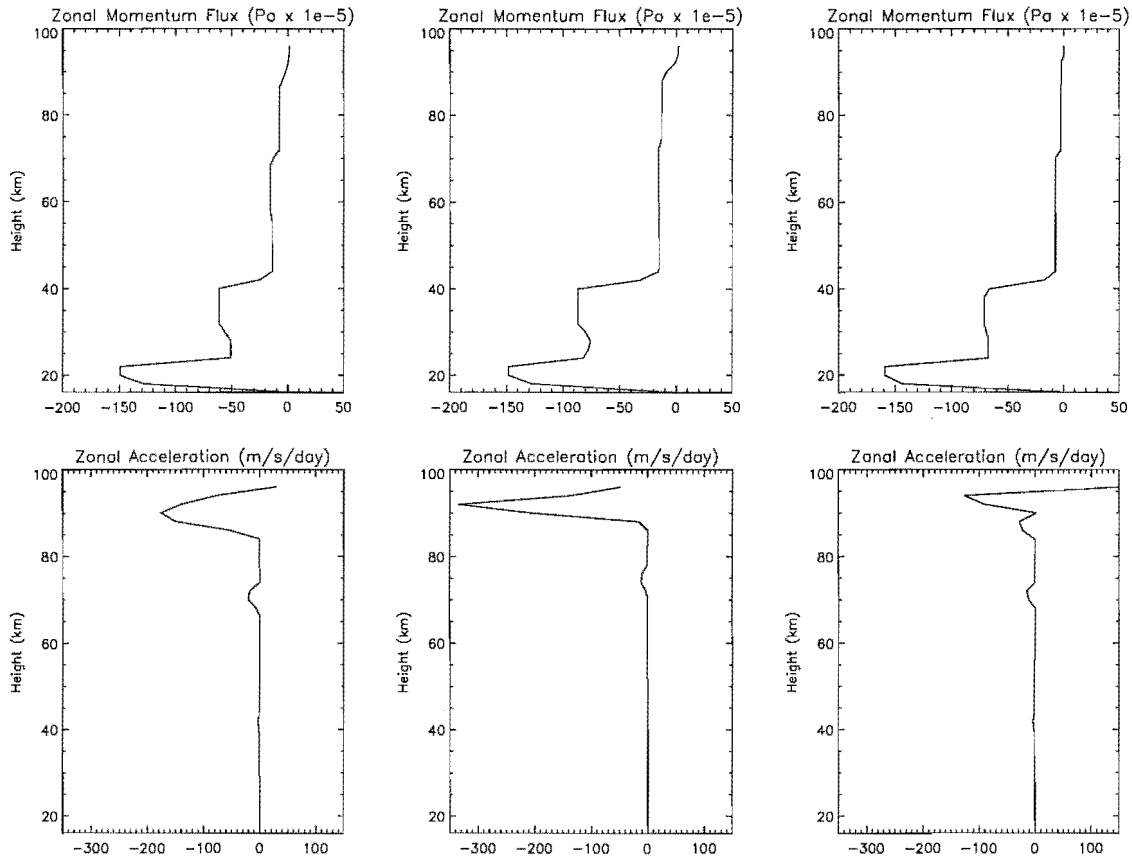

Figure 5.10: Offline vertical output of broad spectrum momentum flux and drag from the DSP, MK95 and USSP gravity wave schemes using a tropospheric source of $\bar{T}'^2 = 5.8 \times 10^{-5}$, during January, at 5°S.

the prescribed source. The momentum flux density is weighted toward the high end of the vertical wavenumber spectrum. Waves here have comparatively low phase speeds and will dissipate first in regions of shear above launch height. Subsequent regions of shear will dissipate less momentum flux as the faster travelling waves which are left carry less.

It is seen in the first region of negative shear, that more westward momentum flux is deposited in the DSP profile, as compared to that from MK95. This can be explained due to the DSP having a stronger wave induced wind within this region of shear. Even though this would be small compared with the Doppler shifting dissipation from the background wind, it is acting on that part of the spectrum with most of the momentum flux - thus increasing its influence. throughout the second region of negative shear (at 40 km), the reverse is seen, more momentum flux is deposited with the MK95 scheme. This can be explained due to those surviving parts of the westward propagating spectrum in the MK95 run (which were removed at similar heights in the DSP profile) now being removed through Doppler shifting from the background wind. However, this explanation would appear to be at odds with the first region of positive shear below. However, in this region the background wind removes more waves within the spectrum, leaving a part of

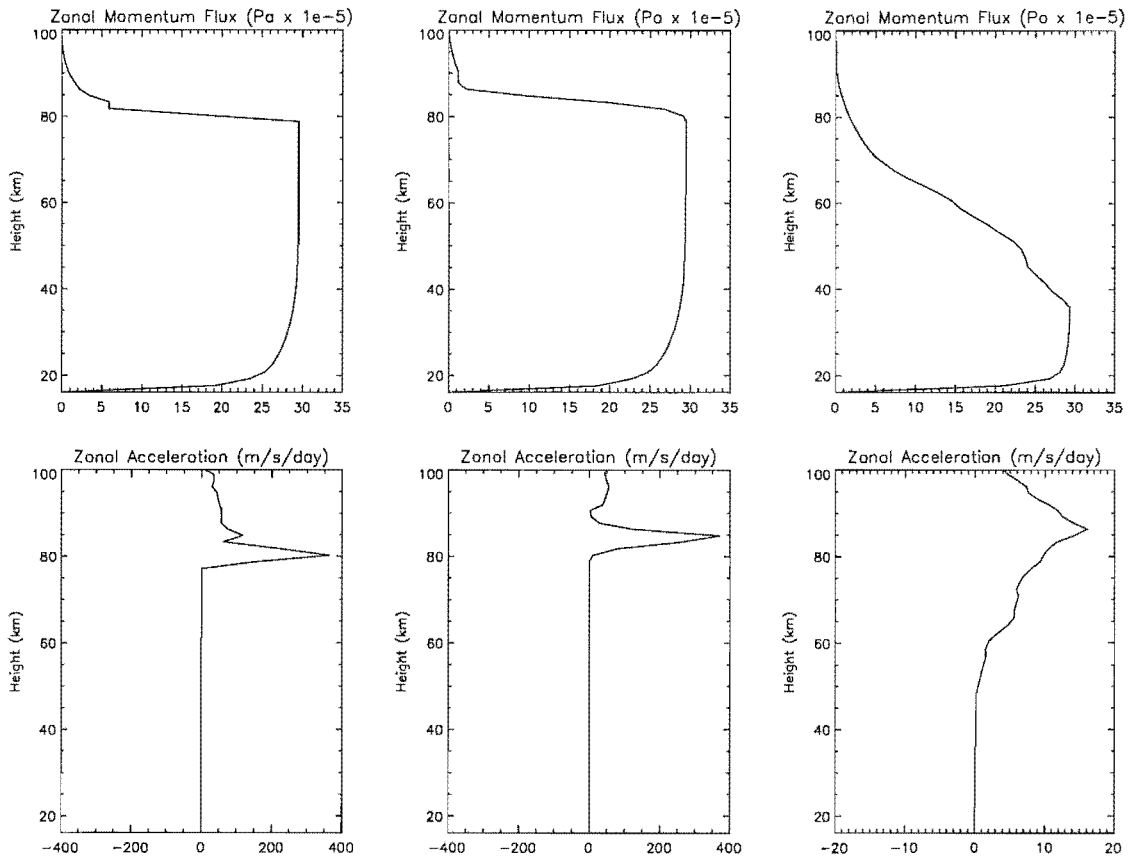

Figure 5.11: Offline vertical output of broad spectrum momentum flux and drag from the DSP, MK95 and USSP gravity wave schemes, using a tropospheric source of $\bar{T}'^2 = 1.5 \times 10^{-5}$, during January, at 35°S.

the spectrum which is less sensitive to small changes in wind.

The USSP behaves in a similar fashion for these particular profiles. Like the other two schemes, it deals with Doppler shifting from the background wind in a similar fashion. Although the amount of dissipation at any particular level is less clear, as this is controlled by the convoluted replacement of the large-m part of the spectrum, after Doppler shifting, by an imposed saturated part.

Translated to levels of drag (change in speed of the background wind), in the mesosphere, there is a factor of three difference. Also from the *change* in momentum flux throughout the height of the profile, one can conclude that there will be subtle differences in forcing in the regions of shear. This may have implications for the success of any modelled circulation there.

Still during January but now for extratropical latitudes (35°S) figure 5.11 indicates a similar corresponding trend. The background wind is westward in sign below 70 km and turns eastward above this. At about 80 km large eastward drag is seen in both the MK and DSP profiles. At this height it should be noted that the wind is still westward and so non-linear effects of other waves in the spectra must necessarily be playing a role in

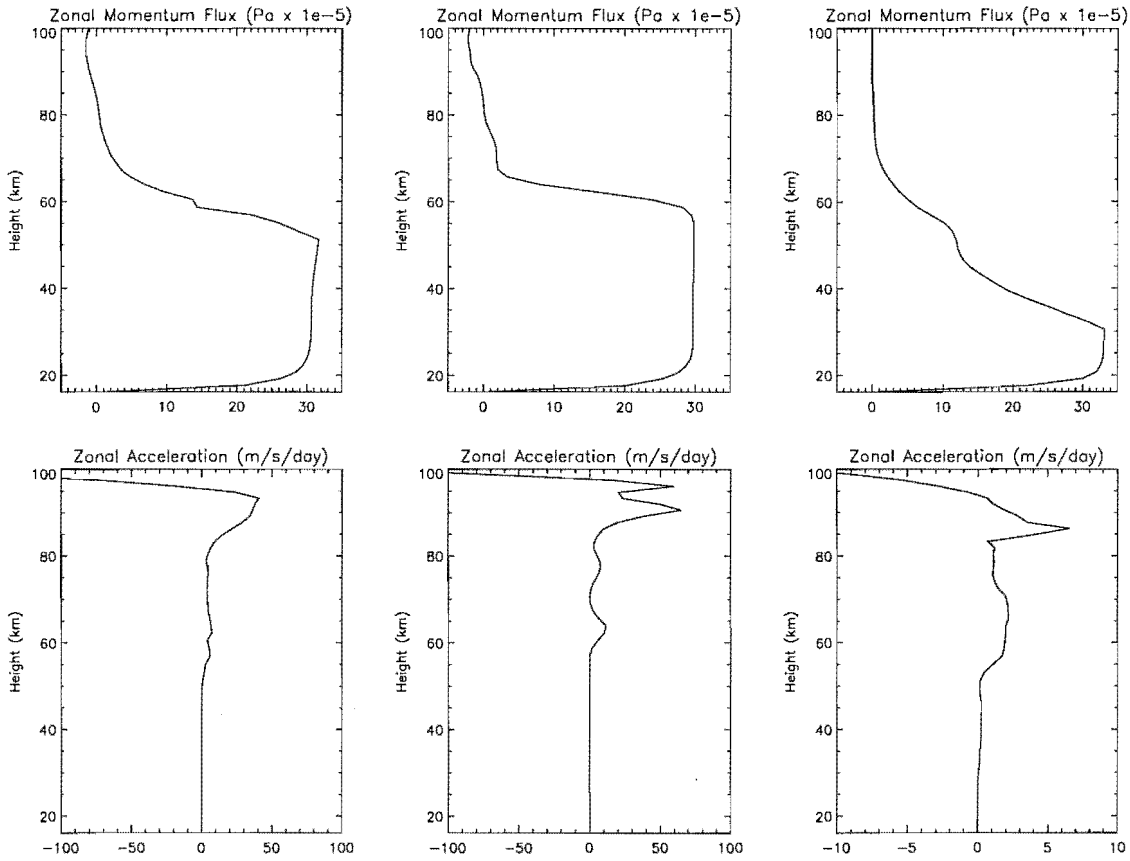

Figure 5.12: Offline vertical output of broad spectrum momentum flux and drag from the DSP, MK95 and USSP gravity wave schemes, using a tropospheric source of $\bar{T}'^2 = 1.7 \times 10^{-5}$, during March, at 35°S.

the onset of the drag. This is quite surprising as the role in the DSP of waves facilitating dissipation is much more pronounced than in the MK scheme (where only those waves having times scales longer than a given harmonics frequency are able to influence it). Although there would appear to be a perceptible difference, albeit a small one. However, a marked difference is seen between the USSP and the other two at a height of 35 km where an indication of eastward travelling waves dissipating in the former scheme reduces the amount of net momentum flux. This feature is seen in all subsequent profiles and is a characteristic of the USSP scheme. All three have sources have been set up so as to engender dissipation from the outset (barring any Doppler shifting effects from the background wind). That is, the large-m end of the wavenumber spectrum is very close to saturation. In an isothermal, windless atmosphere spectral dissipation is a function of altitude (atmospheric density) for all schemes. However, for the USSP, dissipation is a also strongly influenced by the shape of the low-end part of the wavenumber spectrum and the imposed saturated part (refer to 4.4). For these tests, the imposed saturated part has the conventional slope of -3. It is this latter effect which is causing these differences (refer to Appendix C).

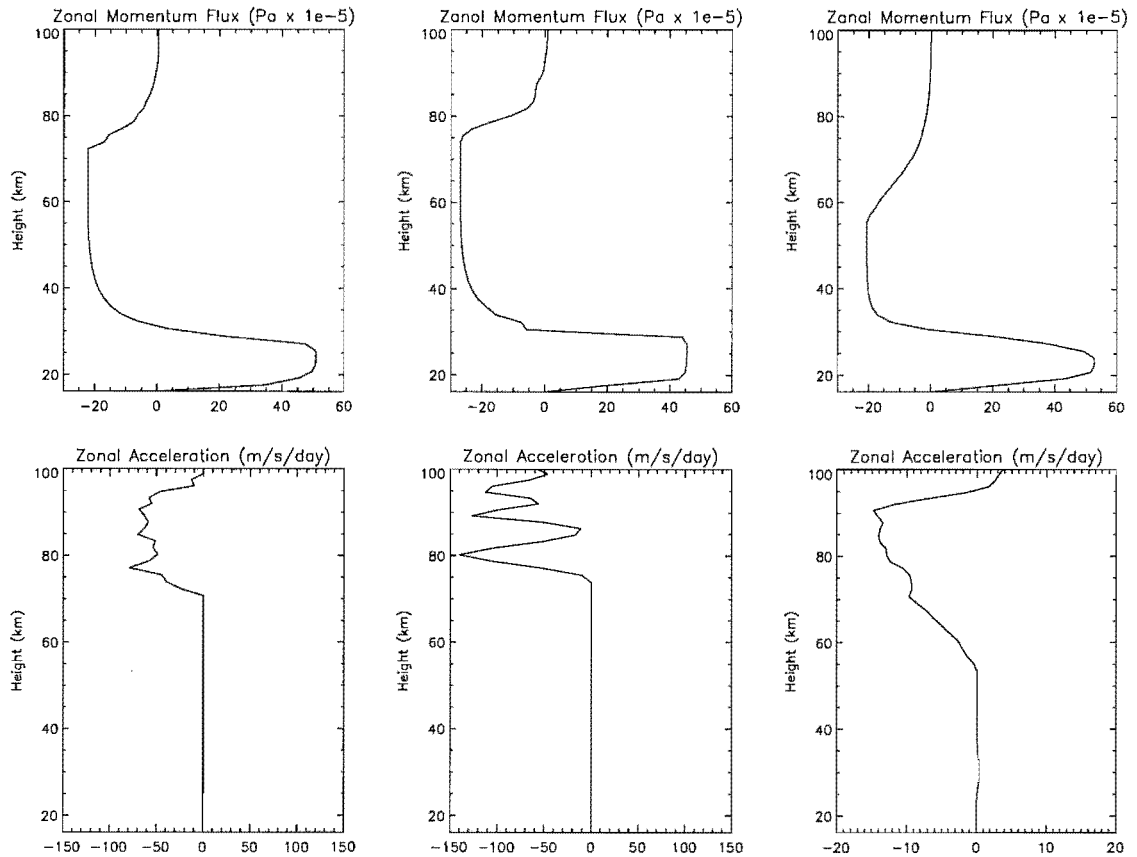

Figure 5.13: Offline vertical output of broad spectrum momentum flux and drag from the DSP, MK95 and USSP gravity wave schemes, using a tropospheric source of $\bar{T'}^2 = 2.9 \times 10^{-5}$, during July, at 35°S.

At equinox, figure 5.12 shows a difference which one would expect between the MK and DSP schemes. The background wind turns to having positive shear at about 30 km. However this reversal to positive shear is weak (when compared to the January background wind) and it would appear that it is this which results in the difference in onset of dissipation (as seen in the momentum flux profiles) between 50 km and 60 km. The higher level of onset as seen with the MK profile results in a larger drag due to lower air density. This reasoning would also be consistent with the slightly larger and highly situated drag seen above 90 km. However, they still continue to have gross features in common. The USSP profiles also share a rough correspondence with the other two, but again, having far lower values of drag.

The winter profiles show the most marked differences between the plots (5.13). Above 80 km, although similar in sign, the MK and DSP schemes show significantly different profiles for drag. It would appear that these arise due to the amount of net westward momentum flux remaining in the in the upper stratosphere/lower mesosphere region. There is more left to dissipate in the MK profile - hence, the greater drag. This difference, though, has its origins just above launch height (16 km) where the background wind is

weakly negative (westward) and slowly turning with height. Thus the wind shear is weak so non-linear effects can be viewed above the effects of Doppler shifting by the backgound wind. The DSP will produce stronger non-linear interactions due to the inclusion of the entire spectrum in the total wave-wind term of equation 4.7. Also, most of the spectral momentum flux resides at the high end of the wavenumber spectrum which will be the first part to dissipate above the level of launch. Thus any nonlinear effects will be magnified because of this. If one were to observe the USSP momentum flux profile at these lower heights one would observe consistently greater net values. This is because the nonlinear effects represented in that scheme (i.e. changes of density and low and large m-end spectral shape) play a greater role then either of the other two schemes during these conditions.

5.3 Discussion

In summary of section 5 it is apparent that the dominant influence on the evolution of orographic gravity waves and those comprising a broad spectrum is the background wind. This should come as no surprise as the nature of the gravity wave interactions are nonlinear and subject to special conditions, more often than not imposed by the background wind.

In the presence of vertical wind shear, the effect of orographic waves on the broad spectrum appears minor and only becomes non-negligible just prior to dissipation of the oro-wave. Furthermore, this effect only becomes noticeable if the oro-wave is able to break relatively high in the atmosphere (probably high-stratosphere and above). Also, the effect on the broad spectrum appears only to occur around the region of dissipation. Such knowledge should be tempered with the fact that about these regions it is likely that any *orographic* drag would most probably swamp any tell-tale signature of such a wave-wave interaction seen in the broad spectrum drag.

As for the relative importance between the oro-wave Doppler-spreading the broad spectrum of waves (as seen by the inclusion of the oro-variance in σ_j (equation 4.16) and it destabilising the spectra as a whole (as tested by varying Φ_2), both appear to have comparable influence, though both are minor.

However, with little or no wind shear the nonlinear interactions of the gravity waves become more noticeable. According to DSP an oro-wave should break lower down in the presence of these other waves. It was found though that for strong orographic waves this effect was effectively nullified. Even for relatively weak orographic waves (and a strong broad spectrum) the difference in breaking height was less than 10 km. Such a feature would be very difficult to identify, as the major factor influencing the breaking height of an orographic wave is its initial wind amplitude (and of course the background wind). Such differences could be significant during times of equinox when winds are generally weaker than at other times of year. This will be investigated further in chapter 8.

With no wind shear, the influence of a quasi-monochromatic wave on the broad spectrum is quite 'noticeable'. However, the effect should not introduce any *net* momentum flux as the waves in counter-propagating directions are affected equally. The result becomes more pronounced with a stronger oro-wave and weaker broad spectrum, though it is difficult to envisage such effects being observed.

The results of these tests indicate that any modelled interaction between the two sorts of waves should be minor. However, as these tests are *off-line*, it remains to be seen whether more subtle responses are captured in a fully interacting model (Chapter 7).

In reference to section 5.2, Doppler shifting also appears to play a dominant role - in two of the schemes studied, anyway. In regions of strong wind shear one would expect similar results from both the MK and DSP schemes when included in an atmospheric model. However, on passage through areas of weak shear, the relative differences between the two schemes become apparent - the DSP having greater scope for nonlinear effects and producing noticeable change.

The third gravity wave scheme (USSP) produces results which are considerably different from the other two. Similarities only become apparent in regions of rapidly changing shear, as seen with the tropical profiles, where all schemes are dominated by Doppler shifting from the background wind. The nonlinear effects from saturation processes (as set out in the theory of the USSP) appear to play as important a role as Doppler shifting (refer to Appendix C). However, in order in achieve the required drag in the mesosphere to close off the solstitial jets, drag of tens of metres per second per day, there seems to be no way to avoid artificially increasing the strength of the parameterised source at the models' bottom boundary. It would seem reasonable to acknowledge that any operational gravity wave model must reproduce effects comparable with others using realistic source strengths. At the time of writing the authors of the USSP were investigating the significance of these findings (pers. com.).

One is limited in gauging the possible significance of differences between schemes without employing a comprehensive 3-d atmospheric model. It is useful in that one can identify possible areas of interest which would be otherwise very difficult to do within a wholly dynamical model. However, one can only truly gauge the significance of such differences in such an environment. These will be investigated further in chapter 8.

Chapter 6

Offline Runs Through UKMO Data

An examination of zonal asymmetries in meridional momentum flux reaching the mesosphere is made using the Hines Doppler spread parameterisation of gravity waves. As expected a general correspondence is seen between wave one wind structures in the stratosphere and wave one signals in gravity wave momentum flux leaving the stratosphere. However, a significant difference is the presence of wave one features in the gravity-wave momentum flux at 56 km and ~70°N during mid-summer which have no corresponding feature in the stratospheric wind field. The prominence of this feature is accounted for by a significant wave one structure in the Brunt-Väisälä frequency at the tropopause amplifying a wave one signal in momentum flux which can then propagate to great heights. Such a feature could result in mesospheric planetary waves which are coupled to the tropopause forcing without intervening planetary wave signals in the stratosphere.

6.1 Introduction

It has long been known that asymmetric gravity wave sources can produce mesospheric planetary waves (*Holton*, 1984). The modulation of zonally symmetric gravity wave sources by the regime through which they propagate can also lead to significant asymmetries in observed gravity wave (GW) variances (*Alexander*, 1998), which lead to planetary scale waves when the waves break.

Observational studies demonstrate that this latter contention is possible: *Smith* (1996, 1997) using stratospheric and mesospheric winds from the High Resolution Doppler Imager (HRDI) dataset showed that late winter mesospheric winds were found to anticorrelate with stratospheric winds. It was proposed that this could be explained by either an upwardly propagating wave turning in phase with increased height or a spectrum of GWs, having been filtered by stratospheric winds, breaking at mesospheric heights. They concluded that the first effect was more likely to explain this anticorrelation in the southern hemisphere while the second was likely to be responsible for those in the northern hemisphere.

In this section, an initial study is carried out using a realistic spectral gravity wave parameterisation *Hines* (1997b) aimed at exploring the effect of realistic wind environments on the propagation of a gravity wave spectrum from the troposphere through to

the mesosphere. Emphasis is put on one feature observed in the results: the production of zonal wave one perturbations in gravity wave momentum flux is not only associated with stratospheric wind filtering, variations in the tropopause temperature structure are important too. We begin with a review of the data sources and parameterisation used and then present the results.

6.2 Theory and method

The key feature of the *Hines* (1997b) parameterisation is that a number of interacting spectra distributed in direction are allowed to propagate with height. Their propagation is controlled by the evolution with height of the parameter m_j - the cutoff wavenumber, whose diminution in height ultimately controls the transition of momentum flux between the spectrum and the background flow:

$$m_j = \frac{N_i}{\Phi_1 \sigma_j + \Phi_2 \sigma_h + \Delta V_j} \tag{6.1}$$

Here, σ_j and σ_h represent the rms wind variations due to the waves of the spectrum in the jth azimuth of propagation, and all directions, respectively. ΔV_j represents the difference in the background wind between the height of interest and some previous height. Φ_1 and Φ_2 are adjustable parameters, while N_i is the static-stability at some lower reference height. For a more complete description of the theory behind the parameterisation refer to section 4.2.

The factors which lead to a decrease in m_j are changes to the static stability (N) and Doppler shifting. Doppler shifting arises when either the background winds change via height (V_j) or from the effect of the waves themselves (via the σ values). This last tendency increases in importance with height as the σ values increase with decreasing density.

It is apparent that if there is a planetary wave signal in the winds through which this parameterisation propagates, it will induce a wave signal in m_j and hence in the momentum flux. If such wave features are not stationary with height, the response is effectively rectified (as m_j can only decrease): signals induced at a lower height would be damped as the opposing winds from the phase-changed waves would reduce the net amount of GW momentum flux. However this effective rectification is modified by the density effect and so planetary scale variations in net momentum fluxes should still be produced in this situation but with lesser amplitudes. Planetary wave signals in any non-zero net momentum flux can also be induced or modified at any height by zonal asymmetries in the local static stability, since at all locations both σ_j and σ_h are also implicitly dependent on the local value of N (equation 3.6, *Hines* (1997b)).

Seven years of daily gravity-wave momentum flux calculations were made on a five degree latitude and longitude grid produced using UKMO assimilated wind and temperature data *Swinbank and O'Neill* (1994). These data were further interpolated onto an equally spaced grid in log pressure from 4 km to 56 km (using log-pressure height) and $H = 6950$ m. For this study, only data since Jan 1 1992 were used. An isotropic source was prescribed for the lower bound using a σ_h of 1.4 m s^{-1} incorporating spectra travelling in eight equally spaced directions.

Daily momentum fluxes were calculated and climatological monthly means produced for the winds, static stability and momentum fluxes. A one-dimensional Fourier analysis in the zonal direction identified the mean wave-one components. It was found that the difference between wave one climatological monthly means and climatological monthly mean values for daily wave one fields were insignificant.

The results presented here are restricted to net values in the meridional (N-S) direction, as the mean zonal component of the mean wind, which varies appreciably with height throughout the year, tended to contaminate any interpretation of the zonal component of GW momentum flux by reducing those spectra in that direction, thus affecting the spectra's response to planetary wave winds. Wave two fields were found to be appreciably weaker than wave one and so have also been excluded from this study.

6.3 Results

A comparison is first made of the morphology of the wave one wind and the calculated momentum flux fields at 56 km - about the stratopause (6.1), as it is believed the momentum flux variations entering the mesosphere could lead to mesospheric planetary waves *Holton* (1984). Broad agreement can be seen during the northern winter at latitudes above 40°N where peak values in both momentum flux variations and winds correspond with the favourable conditions for vertical propagation of zonal wave one planetary waves through a background of predominantly westerly winds.

During the northern summer at ~70°N there is a region of weak wave one wind amplitudes seen in the data. There is a corresponding peak in magnitude in the calculated wave one N-S GW momentum flux at these latitudes. There is also a less prominent peak in the summer momentum flux at ~30°N. A stronger GW signal appears in the zonal component collocated with these N-S features (not shown).

The N-S GW momentum flux at ~70°N in northern summer peaks at ~40% of the magnitude of the peak winter value. If one considers only the 56 km values of the wave one winds, this is a surprising result given the difference between the two seasons.

Although there are differences which will be explored elsewhere, the southern hemisphere shows very good agreement between the wave one N-S wind and momentum fluxes.

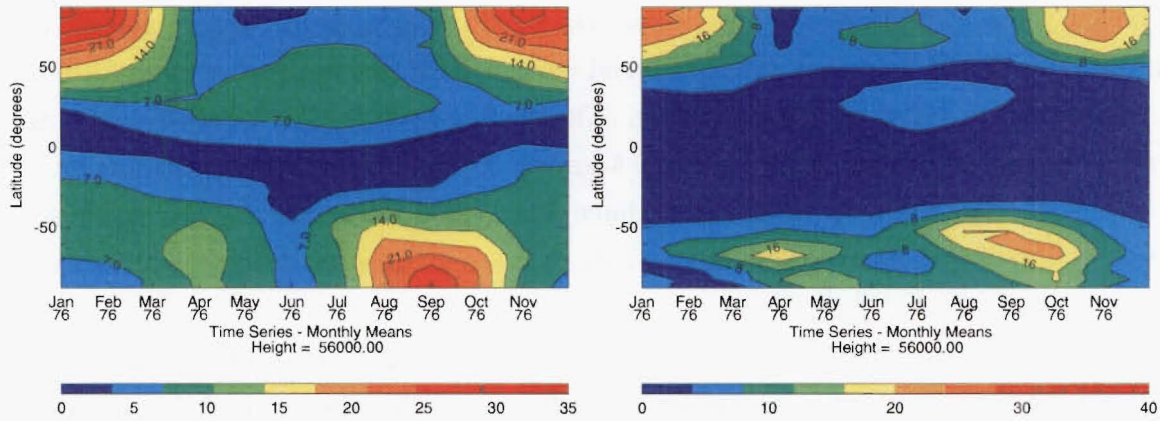

Figure 6.1: Time series of the latitudinal distribution at 56 km of the zonal wave one perturbation in: meridional wind (left, $\mathrm{m\,s^{-1}}$) and calculated momentum flux (right, $\times 10^{-5}$Pa).

The expected double peak in planetary waves during late autumn and early spring (*Randel*, 1988), leads to a double peak in momentum fluxes.

6.4 Discussion

When comparing the 56 km momentum fluxes with the 56 km winds, one needs to be careful: the momentum fluxes represent the integrated effect of the spectrum propagating up through the atmosphere below, whereas the wave one winds are simply a snapshot at one altitude. Reference to equation 6.1 (and equation 3.6, *Hines* (1997b)) also suggests that the momentum flux variations will not only depend on the winds (in all directions) but also on the static-stability as described by the Brunt-Väisälä frequency.

To understand the northern summer feature at ~70°N more closely vertical time-series are constructed of both amplitude and phase of the climatological component of zonal wave one N-S winds (v), the amplitude of the calculated N-S GW momentum fluxes (see figure 6.2) at 67.5°N, and the wave one Brunt-Väisälä frequency.

It is immediately apparent from the momentum flux calculations at 67.5°N that large signals reaching 56 km occur during early northern winter (Nov), northern mid-winter (Jan-Feb) and to a lesser extent northern mid-summer (Jun-Jul). Each of these cases is slightly different: in the Jan-Feb case, we see that the wave one signal in the momentum flux arriving at the top of the model occurs when a strong wave one signal in v is prevalent throughout the stratosphere. In the Jun-Jul case the momentum signal occurs when there is little wind signal in the stratosphere (and only high up), and the Nov case occurs in a similar manner to Jan-Feb, but the signal is reduced in Dec despite the strong wave one signal in v in Dec. It can also be seen that despite little or no climatological wave one signal in the tropospheric v, there is a significant wave one signal in the tropopausal momentum fluxes. It is interesting to point out that the magnitude of the wave one N-S

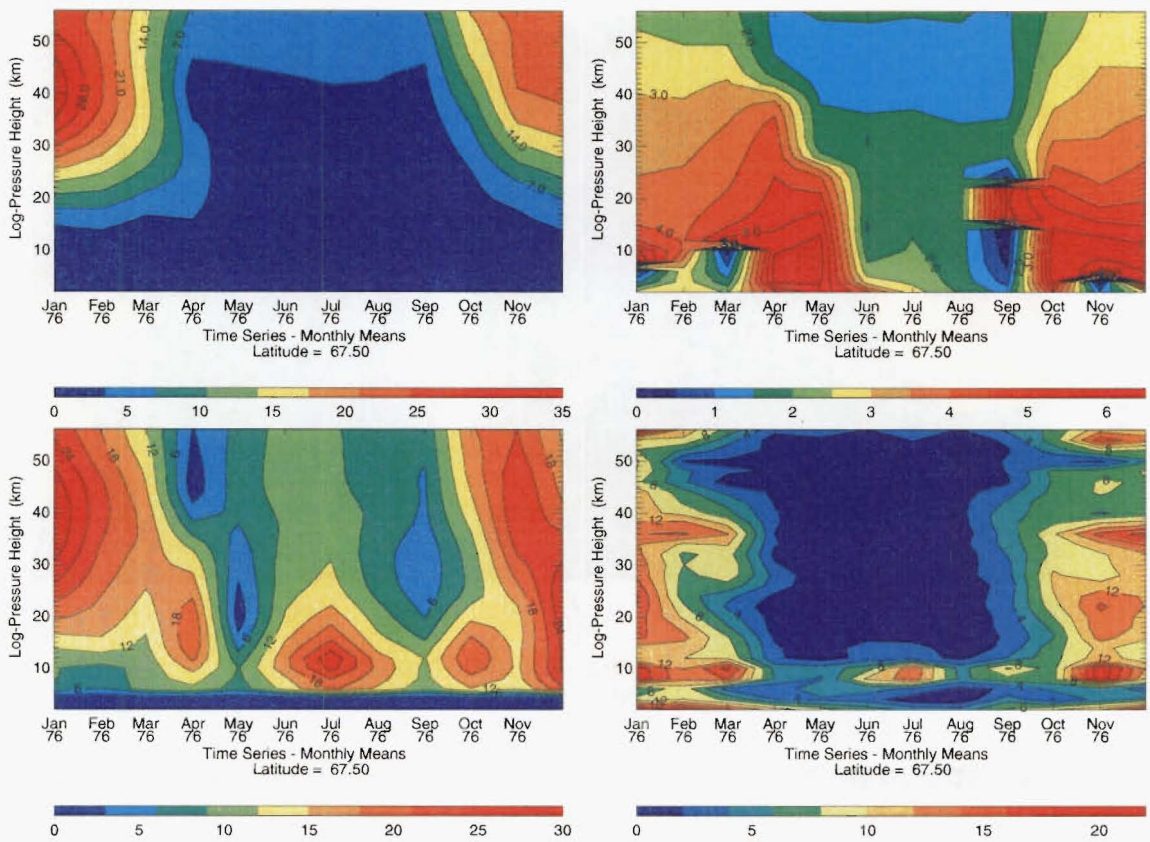

Figure 6.2: Timeseries at 67.5°N of the vertical structure of the zonal wave one perturbations in: observed meridional wind (top-left, $\mathrm{m\,s^{-1}}$), observed phase of the meridional wind (top-right, rad), observed atmospheric static stability (bottom-right, $\times 10^{-4}\mathrm{Hz}^2$) and calculated net meridional momentum flux (bottom-left, $\times 10^{-5}\mathrm{Pa}$).

momentum flux entering the mesosphere was approximately five times greater than the net mean N-S momentum flux (not shown).

The difference between the summer and winter features can be easily understood in terms of the contributing factors to equation 6.1. The tropopausal signal in the summer momentum flux is clearly related to the tropopausal variation in Brunt-Väisälä frequency which leads to an enhancement of wave one momentum flux variations immediately above the tropopause. This signal is able to propagate up to the top of the domain used (56 km) because there is little variation in the wave one winds above, which means that the signal induced in the m_j will remain until the spectrum begins to break in a manner which doesn't preserve the zonal asymmetry.

Tropospheric features of momentum flux occurring during April and October don't appear to be related to either wind or static-stability. However it is the *relative* contribution of both fields which ought to give rise to variation in momentum flux and not necessarily the size of one of the fields. This would also explain why tropopausal features in static-stability during March and November do not give rise to similar features in momentum flux.

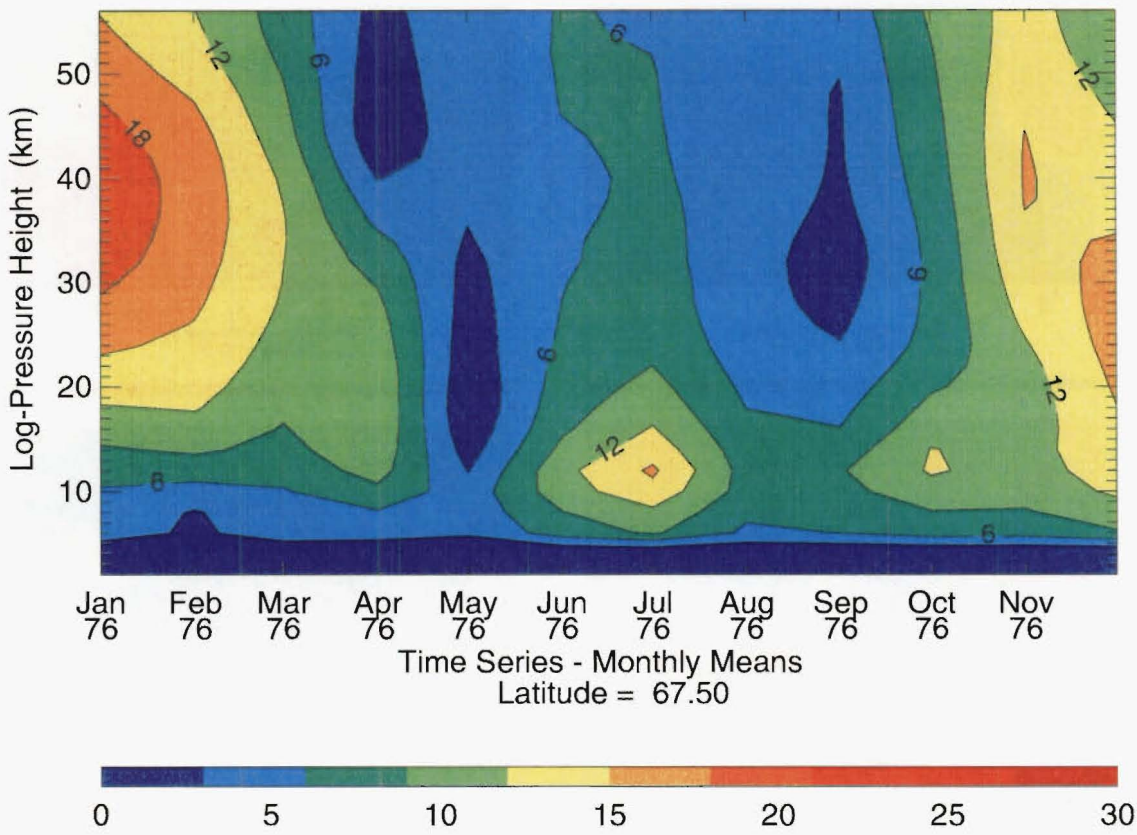

Figure 6.3: Timeseries at 67.5°N of the vertical structure of wave one meridional momentum flux ($\times 10^{-5}$Pa) calculated using zonally symmetric static stability.

In July some of the asymmetry is removed as the gravity wave spectrum propagates up through the lower stratosphere, but much remains to enter the northern summer mesosphere, where the density effect will eventually result in the deposition of this asymmetric momentum field, and the inducement of mesospheric planetary waves. Indeed, preliminary tests using the Stratosphere-Mesosphere Model indicate that planetary waves are generated by this process during summer (section 7.2.3).

To evaluate the significance of the impact of the zonal variations in static stability on the zonal wave one signal in N-S momentum flux one further set of calculations were done after removing the wave-one component from the static stability fields (figure 6.3). Comparison with Figure 6.2 shows the considerable impact of the zonal asymmetry in N on the amplitude of the wave signal in the momentum flux. The remainder of the modulation of the N-S momentum flux which is seen during July, must come from small changes in wave one N-S wind which do not show up due to scaling in figure 6.2.

The non-linear role played by interacting azimuths was also examined. Calculations were made removing the contribution to the wave-parameters in equation 6.1 from those waves travelling in non-parallel directions (6.4). The relative magnitude of the momentum flux decreases significantly from the fully interacting case (Figure 6.2), while the morphol-

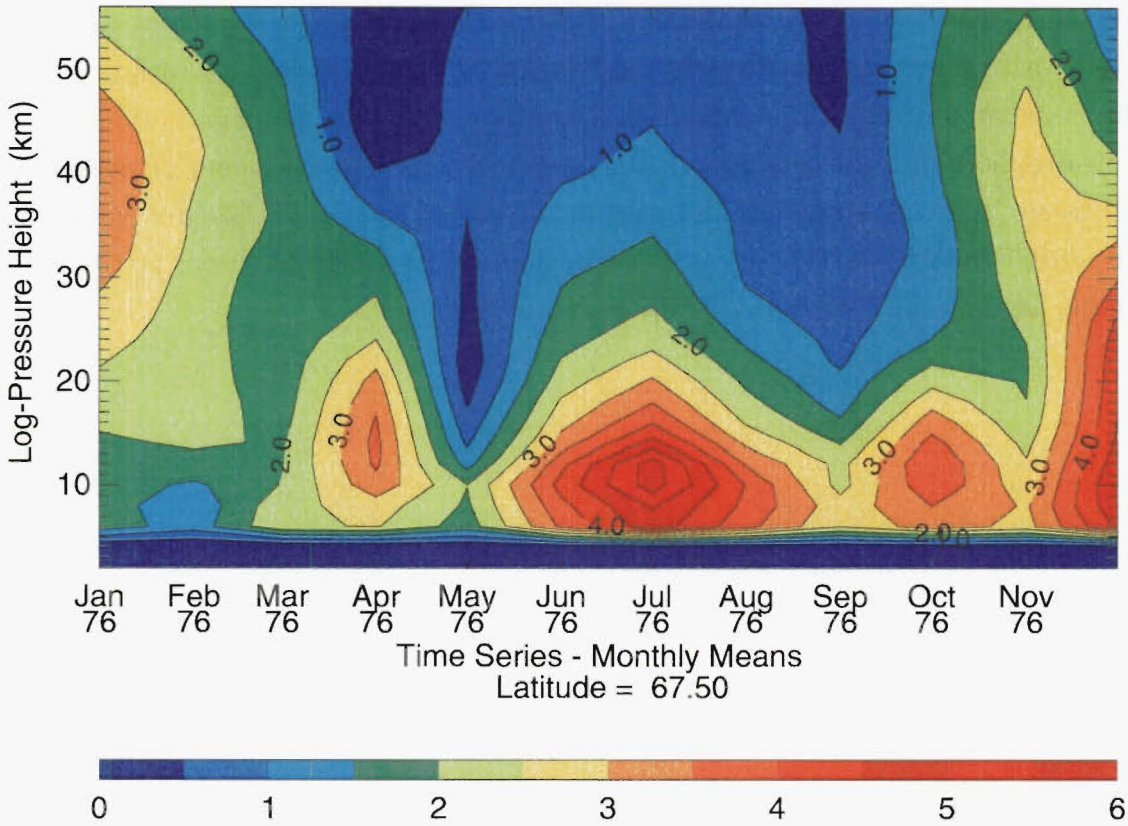

Figure 6.4: Timeseries at 67.5°N of the vertical structure of wave one meridional momentum flux ($\times 10^{-5}$Pa) calculated using non-interacting spectra.

ogy remains largely unaltered. This suggests that such interactions may play an important part in amplifying any signal present and also implies that more basic parameterisations may not be able to reproduce such an effect.

In northern winter the zonal asymmetries in N-S momentum flux are further enhanced by the effect of the zonal perturbations in the winds which lead to large zonal asymmetries in the momentum fluxes via the V_j term in equation 6.1. In December however, this signal is reduced in the upper stratosphere (in comparison with November and January-February). This reduction appears to be due to the change in phase with height of the wave-one signal in v which is much greater in December (which should lead to lesser amplitude response as explained above).

These momentum fluxes leaving the stratosphere are bringing zonally asymmetric momentum fluxes into the mesosphere and this must lead to the forcing of mesospheric planetary waves as discussed by *Holton* (1984) and *Smith* (1996, 1997). Our results are also qualitatively similar to those of *Alexander* (1998) who showed similar filtering effects on a spectrum of non-interacting monochromatic waves. In her work she was concentrating on the observed wave activity, but the filtering effects arose from essentially the same physical mechanisms.

What is new here is the contention that mesospheric planetary waves can also be induced in summer by the effective modulation of the spectrum by variations in the static stability near the tropopause. The spectrum can then propagate unmolested by the stratosphere into the mesosphere where momentum deposition and planetary waves could result. A recent study has also reported observing moderately sized wave one winds in the southern summer 90-120 km height region, whose origin has been attributed to a breaking asymmetric source of GW (*Wang et al.* (2000)).

Chapter 7

SMM Response to a Perturbed Gravity-Wave Source

7.1 The Stratosphere-Mesosphere Model (SMM)

The SMM[1] is a finite-difference mechanistic model of the middle-atmosphere. As such, it does not have a representation of the troposphere, although, to resolve the action of large-scale waves (e.g. Rossby waves), it does require the prescription of model parameters at the models' bottom (temperature, geopotential and horizontal wind). Also, the boundary fields are extrapolated one level below the model bottom.[2] Its vertical extent is normally 16-80 km, however for this study this was extended to 96 km.[3] With discretisation one must represent model parameters on a grid. This is done using an Arakawa-A grid (*Arakawa and Lamb* (1977)) where all model parameters are located at each point within the grid (other grid types have their parameters staggered differently throughout the grid domain). The horizontal resolution is normally 5°x5° (used in this study), however 10°x10° and 3°x3° resolution is also supported.

The dynamic core of the model is the set of primitive equations (2.1-2.4) in finite-difference form. The derivatives contained in these are second-order in the vertical and fourth-order in the horizontal. Time-evolution within the model is achieved using leap-frog integration, with forward timesteps made after each write to disk preventing possible bifurcation of odd/even timesteps during runs. As a consequence of there being the same number of grid points on each line of latitude, convergence of points is seen (in longitude) towards the poles. This can also lead to some dynamic stability problems due to the Courant-Freidrichs-Lewy (CFL) criterion,

$$\left| c\frac{\Delta t}{\Delta x} \right| \leq 1 \tag{7.1}$$

where a reduction of the model time step (usually 240 seconds) would normally be required

[1] version *17e*

[2] This extrapolation has been linked with some dynamic instability thought to arise from a systematically biased advection of the boundary parameters.

[3] It has been found *Lawrence* (1997) that significant differences exist in simulations (employing a 'realistic' gravity-wave parameterisation) run with and without this vertical extension at levels of several scale heights below the extension. One can explain such differences by invoking the principle of *downward control* (see *Haynes et al.* (1991)) on the middle-atmospheric state, by an imposed drag within the domain of the extension.

to maintain the inequality on approach to the poles. However, this is alleviated by a Fourier truncation near the poles of the model fields removing high zonal wavenumbers. For added stability a Shapiro filter is applied over the entire model domain after each timestep *Shapiro* (1970, 1971).

Sub-grid scale processes like small-scale gravity-waves and radiation are parameterised. Several options are at present available to the SMM for the former. The effects of wave drag (due to gravity-wave momentum deposition) can be crudely represented by a *Raleigh friction* acting to relax model winds to zero. In the 96 km version, the relaxation coefficient is constant below 80km and varies above as,

$$\alpha(z) = 10^{-7} + 3 \times 10^{-6}(80 - z)^2/256 \tag{7.2}$$

where z is the the height above sea level, in kilometres. Other, more sophisticated schemes are also in use. The Lindzen scheme dealing with a discrete set of non-interacting (monochromatic) waves has been used in the past along with a scheme from *Fritts and Lu* (1993) incorporating the effects from an assumed broad spectrum of gravity-waves. For this current work, three broad spectrum schemes have been considered: Doppler Spread Theory (*Hines* (1997b)), Medvedev and Klaassan (*Medvedev and Klaassen* (1995)) and a simpler scheme (*Warner and McIntyre*, 1999). The first has been run with a combination of broad-spectrum waves and orographic ones, while the other two incorporate only a broad spectrum.

An input for radiation is needed because of the fourth primitive equation (2.4). This is achieved using the MIDRAD radiation scheme (*Shine* (1988)). It calculates a global radiation budget using archived data of molecular oxygen and ozone to calculate heating rates from short-wave solar radiation. Reradiated long-wave radiation is also used to calculate heating rates from archived CO_2. The degree of reradiation is also modulated from archived mean tropospheric albedo.

7.2 Variations in Gravity Wave Source Strength

Our current knowledge regarding the possible makeup of a global tropospheric source of gravity waves is poor. Computer models can currently run using any number of different gravity wave schemes ranging from implicit (e.g. Raleigh friction) to the kind of spectral schemes being examined here. However, apart from orographic sources, knowledge of source climatologies is currently still sketchy. However, in trying to answer what possible effect these waves have on climate it would be instructive to explore what possible impact an arbitrary *changing* source has. This has relevance to the question of how anthropogenic (human-made) changes impact on us and climate.

To this end, a first approximation to a global source of gravity-waves, can be thought of consisting of two distinct parts: a quasi-monochromatic, one arising from flow over mountains and a broad spectrum of waves originating from any number of different sources. It is fair to assume that the first part can be readily determined using topographic and weather datasets and has been successfully employed as outlined in section 4.1.1. The second source component is less well understood (quantitatively). As such one must approximate the strength, geographic and temporal distribution. As a first attempt one can assume a global mean source for the broad spectrum of waves and change the mean strength to see the effects of such a change on the model resolved middle atmospheric climate.

7.2.1 Non-Interacting Orography

To a first approximation the main contribution to a modelled climate utilising orographic and broad spectrum parts to a global gravity wave source will be their individual influence on the model as distinct from differences arising through their mutual interaction. To investigate this, a series of experiments were run investigating such a climatic response in the absence of these unique interactions.

These experiments differ in the strength of the imposed gravity wave source - as represented by the total wind variance of the broad spectrum of waves, σ_h. This was assumed to be globally homogeneous (the same value everywhere at the models lower boundary - 16 km) and isotropic (waves were taken to have no preferred direction of propagation) and ranged from 1 $m^2 s^{-2}$, 2 $m^2 s^{-2}$ and 4 $m^2 s^{-2}$. Other Hines' specific parameters were the horizontal wavenumber k_h which was given a value corresponding to a wavelength of 900 km. Motivated by the current poor knowledge of the part of the gravity wave spectrum with large vertical scale (corresponding to tens of kilometres), a low wavenumber cutoff was employed, whereby waves with scales larger than this were removed. Other parameters were taken to have values stated in section 4.2.

The interaction of the two sets of waves comes through the relevant terms in expressions (4.14)-(4.17); where wave parameters from either the broad or orographic parts of the source are set to zero, respectively. For example, the exponential term in expression 4.17 goes to one, as the orowave term $\hat{\sigma}_R^2$ must necessarily vanish.

Six year simulations were run from prior to the start of 1992 through to about the end of 1997.[4] The simulations were initialised from daily UKMO data suitably extrapolated up to a height of 96 km.[5] Although the emphasis during the analysis has been below a height of 80 km, an additional 16 km was needed to reproduce the effect of any waves which had

[4]Six-year runs have been carried out for all simulations in this chapter

[5]The uppermost field from the UKMO data (56 km) was simply copied to all SMM levels corresponding to heights above this.

yet to break. Such waves are thought important due the process of *downward control*, whereby they are found to have influence several scale heights below the level which they break (*Haynes et al.* (1991); *Lawrence* (1997)). Finally, daily fields of geopotential, temperature and horizontal wind were employed at the bottom boundary. These were taken from UKMO assimilated data, between 1992 and 1997.

Historically, the inclusion of gravity wave parameterisations in global climate models was found necessary to close the summer and winter stratospheric wind jets and to reverse the direction of the meridional temperature gradient in the mesosphere. This can be seen when figures 2.2 and 7.1 are compared.

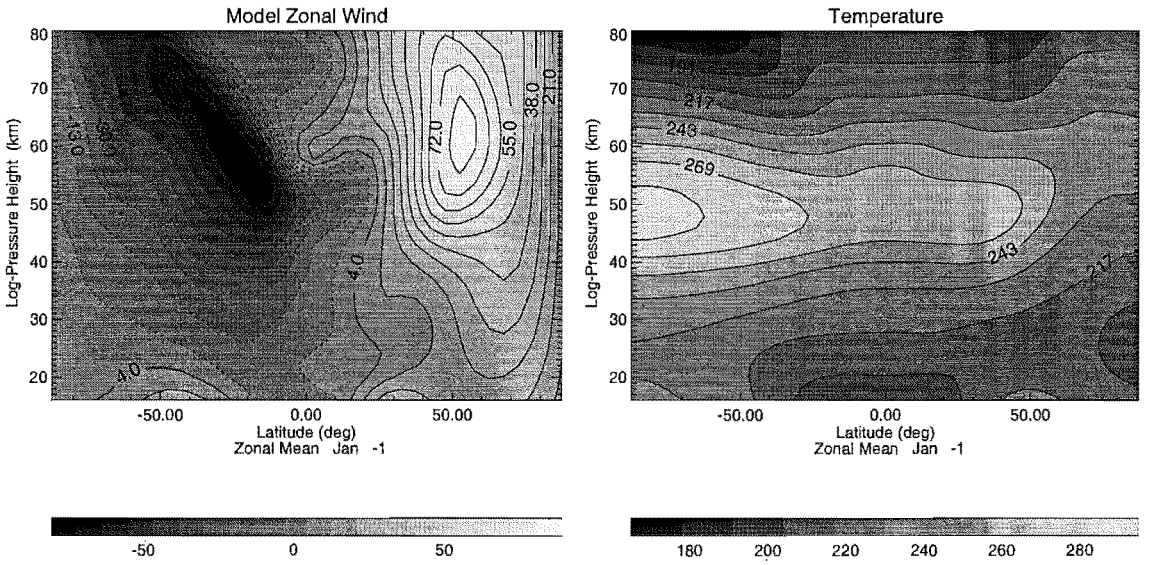

Figure 7.1: Zonal mean averages of zonal wind and temperature in January from the simulation running with a source strength of $\sigma_h = 1.0\ \mathrm{m^2\,s^{-2}}$ and no interaction between orographic and broad spectrum waves.

Figure 2.2 represents the predicted state of the atmosphere when no dynamical effects are included; that is a radiatively determined state. Figure 7.1 represents output from the SMM including the Hines parameterisation for gravity waves. The temperature profile differs from the radiatively determined case above a height of approximately 60 km. The meridional (north-south) gradient of temperature is seen to reverse with the parameterised inclusion of these waves effects. Associated with this is a closing of the solstitial stratospheric wind jets. This is seen in observations (refer to appendix D). Early attempts to reproduce the affects of these waves included introducing a friction like forcing (*Leovy* (1964)) which slowed the wind jets and resulted in a meridional circulation. Such a circulation is found when more realistic parameterisations are used and are a result of the competing effects of the Coriolis force and the drag of these waves breaking in the mesosphere.

Figure 7.2 shows the drag associated with the breaking of the parameterised gravity waves in the mesosphere. The atmosphere's response to this is for a meridional circulation

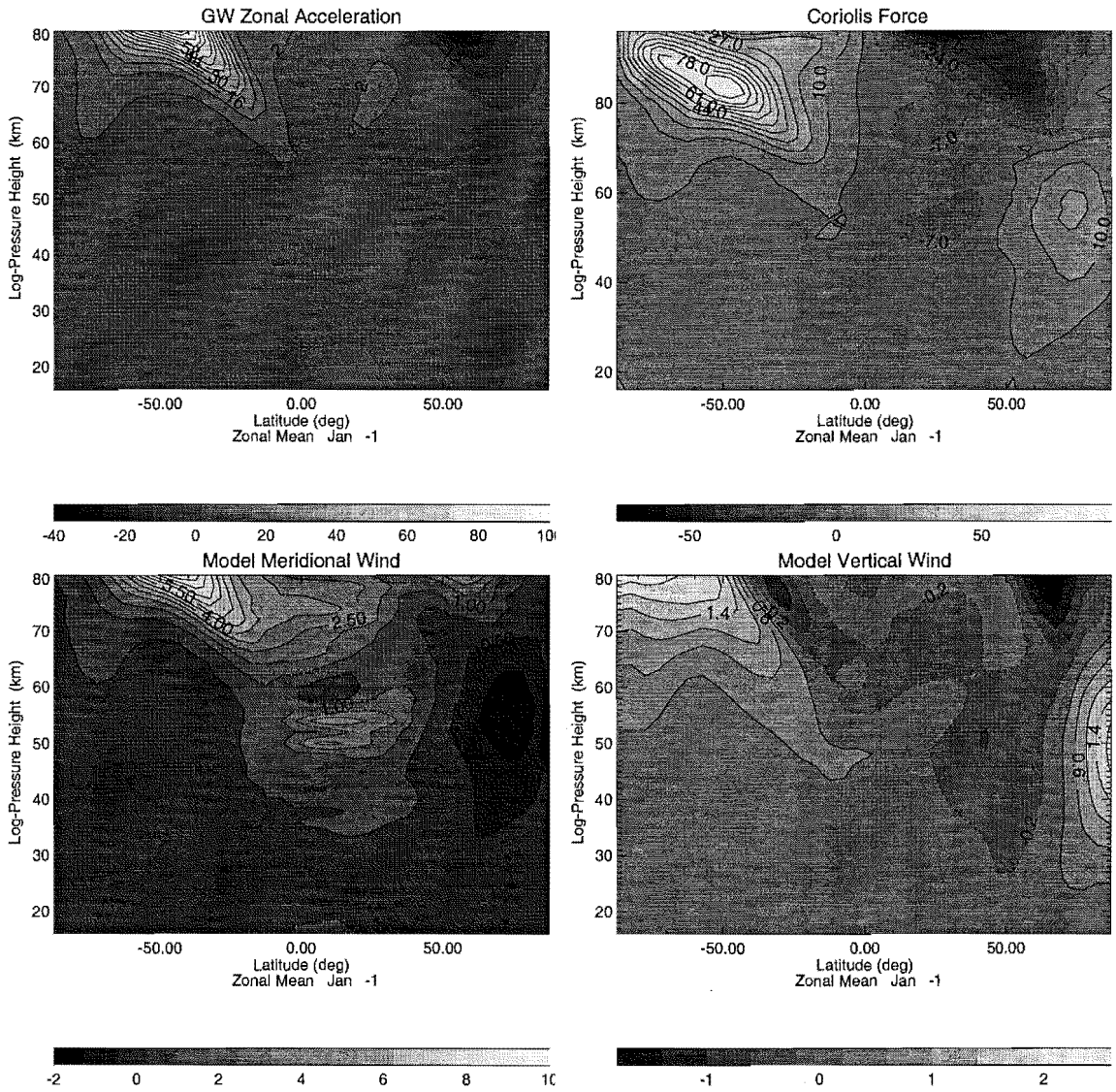

Figure 7.2: Zonal mean averages in January of gravity wave drag (m/s/day), Coriolis forcing (m/s/day), residual mean meridional and vertical wind (m/s) from the simulation running with a source strength of $\sigma_h = 1.0\ \mathrm{m^2\,s^{-2}}$ and no interaction between orographic and broad spectrum waves.

to develop along with opposing zonal Coriolis forces. Descent/ascent occurs over the winter/summer poles, respectively, as a result of continuity (conservation of mass). These vertical motions over the poles will move air between regions of different temperature and also create adiabatic heating/cooling through movement into more/less dense regions. It is found that the former effect, the advection of heat from one place to another is less significant over the poles as compared with the mechanical heating (figure 7.3). As such, it is found that these forcings drive both poles away from temperatures which would arise through radiative considerations alone. Consequently, the summer pole is cooler while the winter pole is warmer.

Figure 7.4 represents the modelled climate response to an increasingly strong gravity wave source ($\sigma_h = 1\ \mathrm{m^2\,s^{-2}}$, $2\ \mathrm{m^2\,s^{-2}}$ and $4\ \mathrm{m^2\,s^{-2}}$) during January. These simulations

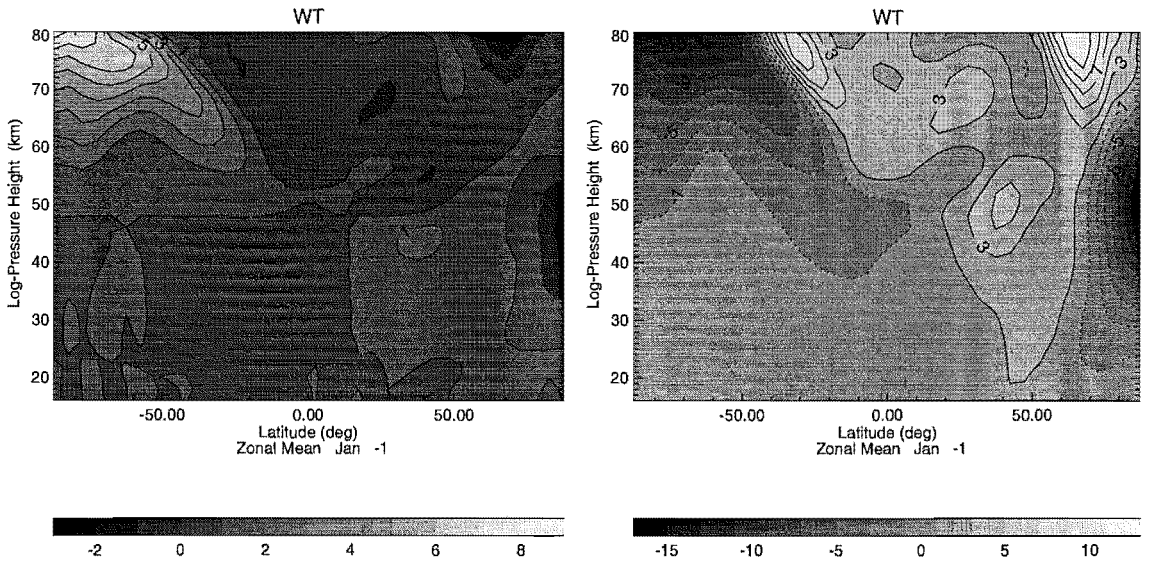

Figure 7.3: Zonal mean averages in January of vertical: temperature advection and adiabatic heating (K/day), from the simulation using a source strength of $\sigma_h = 1.0\ \mathrm{m^2\,s^{-2}}$ and no interaction between orographic and broad spectrum waves.

differ in the amount of drag deposited in the mesosphere - where a larger gravity wave source results in a stronger drag (figure 7.5). The drag profiles indicate a descent in the level of drag with increased source strength. There would appear to be a correspondence in the nature of the summer broad spectrum drag between the simulations with $\sigma_t = 1\ \mathrm{m^2 s^{-2}}$ and $2\ \mathrm{m^2 s^{-2}}$. The shape of the profile would appear to be linked with the stratospheric jet below. The gravity wave drag associated with the simulation having the highest source strength extends to below the stratopause ($\sim$56 km). Though small in magnitude at these heights, its effect is more pronounced due to the increased air density. The shape of the drag in the strong source simulation is also different from the other two; presumably because of the profoundly different summer jets which occur between that simulation and the other two. The drag in the winter hemisphere does not have as irregular a shape as that in the other hemisphere and the maximum descends as the forcing is increased. The direction of the drag is opposite to the direction of the zonal winds below as these preferentially filter out similarly directed waves leaving those with oppositely directed phase velocities to break higher up.

The orographic drag displays a similar trend with the maximum descending with increased source strength. *Positive* drag occurs over parts of the Andes. Orographic drag will always be directed to oppose the underlying winds they pass through, that is they act to reduce wind strength. As a consequence the southern summer westward winds will undergo eastward drag. Concomitant with the drop in height of the orographic drag maximum is a decrease in its strength. This is simply due to the increased air density at these lower heights. The level of these breaking heights is very sensitive to the strength

and position of the polar night jet, thus any changes in wind between simulations will have an impact on the level of this drag (refer to figure 7.4).

Returning to figure 7.4, however, the model zonal wind displays some striking changes as σ_h is varied. The strength and position of the southern jet changes markedly. The jet from the low source strength case peaks in magnitude at about 70 m/s. Significantly weaker winds peaking at around 30 m/s are seen for the σ_h =4 $m^2 s^{-2}$ case. At σ_h =2 $m^2 s^{-2}$ the jet also splits in two with the maximum at 20°S and 70°S in agreement with the CIRA86 data (see Appendix D) with peaks lowering by over 5 km . The northern winter jet maximum does not exhibit a similar decrease in strength but does fall in height by about 10 km between the simulations, however, there is no perceptible tilt of the jet toward the tropics with height which is found in both the UKMO and CIRA86 datasets (refer Appendix D). Both hemispheres' jets are seen to close due to gravity wave forcing in the mesosphere. This is in line with observations.

Features found in the temperature fields are linked intimately with ones found with the zonal wind. It is seen that the equatorward gradient in temperature above the stratopause diminishes as σ_h is increased, which would explain the weakening in strength of the summer jet (via thermal wind). Polar mesospheric temperatures also differ by about 15 K consistent with ascent over the summer pole. The meridional temperature gradient in the northern mesosphere reverses in sign at mid to high latitudes and a cold bias is to some extent alleviated in the lower mesosphere as stratopause temperatures rise by 20 K, but persists higher up (refer to Appendix D). Stratospheric temperatures do not differ appreciably between simulations though.

Changes seen in the residual mean circulation are consistent with Coriolis associated circulations responding to the fall in height of peak gravity wave driving (with increased σ_h) - thus penetrating lower down. This is witnessed by increased upwelling/downwelling over the summer/winter poles and a meridional drift reaching further down. This would have an effect on the temperature fields of advecting heat away from the summer stratopause thus smoothing the associated temperature gradient there. The stratospheric feature centred about the northern pole found in the lower strength output in the vertical wind is transient in nature and is associated with the number and strength of stratospheric warmings which have occurred during the month. The disappearance of this with the higher sourced runs may indicate an otherwise unreported interaction between planetary waves and these smaller scale ones. On examination of daily January output a slight change in frequency and timing of sudden warmings was noticed between the simulations, however, no systematic difference was seen.

Possibly associated with the change in character of sudden warmings is the poleward gradient in zonal wind northward of 60°N (figure 7.4). *Butchart et al.* (1982) showed that the polar-night jet at 30 km needed to peak around 75°N instead of 60°N (which

is seen climatologically), in order for them to model a major sudden warming. The poleward gradient in zonal wind is weaker in the simulations running with a stronger gravity wave source. This would indicate that, on average, the lower stratosphere is less suited to support the onset of these warmings - the background state is *ill-conditioned.* Any explanation as why this difference occurs is complicated by the nonlinear relationship between the large-scale planetary waves and the mean flow. Suffice to say that it is the change in circulation set up by the altered gravity wave source that ultimately gives rise to any differences seen.

Concerning the tropical stratosphere a noteworthy result is the formation of a QBO-like (Quasi-Biennial Oscillation) structure. This is found to occur for the σ_h =4 $m^2 s^{-2}$ simulation but for none of the others. This has been examined extensively by *Lawrence* (2001) using the Hines' scheme incorporated in the Stratosphere Mesosphere Model. Unlike here, that study did not include the effects from an orographic source of gravity waves. The inclusion of such is not thought to have any noticeable impact on the formation of a QBO and so will not be pursued further.

The trend in resolved large-scale wave activity can be seen in figure 7.6. These output were constructed from daily zonal (u) and meridional (v) SMM wind data. The zonal mean was removed from each and the resultant fields combined to give a measure of the large scale momentum flux - $\bar{u'v'}$, which was then zonally averaged. Six years of this output were then averaged for the month of January. It can be seen that large amplitude waves propagate up into the northern winter stratosphere (refer to section 2.6), peaking in magnitude about the stratopause (60 km). This feature is seen to fall in height between the three simulations, from approximately 60 km to 50 km. Variability in the propagation of these waves, as depicted by plots of standard deviation, is less in the higher strength runs. This is linked directly with the change in nature of stratospheric sudden warmings which occur between the three simulations during the month.

During equinox (climatological Aprils) one sees a continuation of deeper gravity wave induced residual circulations with stronger wave driving. Again, the peak in broad spectrum drag descends between simulations, this time notably in the southern hemisphere, where drag is seen as low as the stratopause for the σ_h = 4.0 m^2 simulation (figures 7.7, 7.8).

Other fields during April exhibit similar features as compared to the January results. Concomitant with the peak in gravity wave drag descending with increased σ_h, is a deeper meridional circulation. This, acting together with stronger and deeper vertical winds, helps to warm the southern stratopause by approximately 20 K. Furthermore, this warming is not confined to above the stratopause - significant warming occurs below. Contrast this to similar heights in the polar north where there is little difference between simulations.

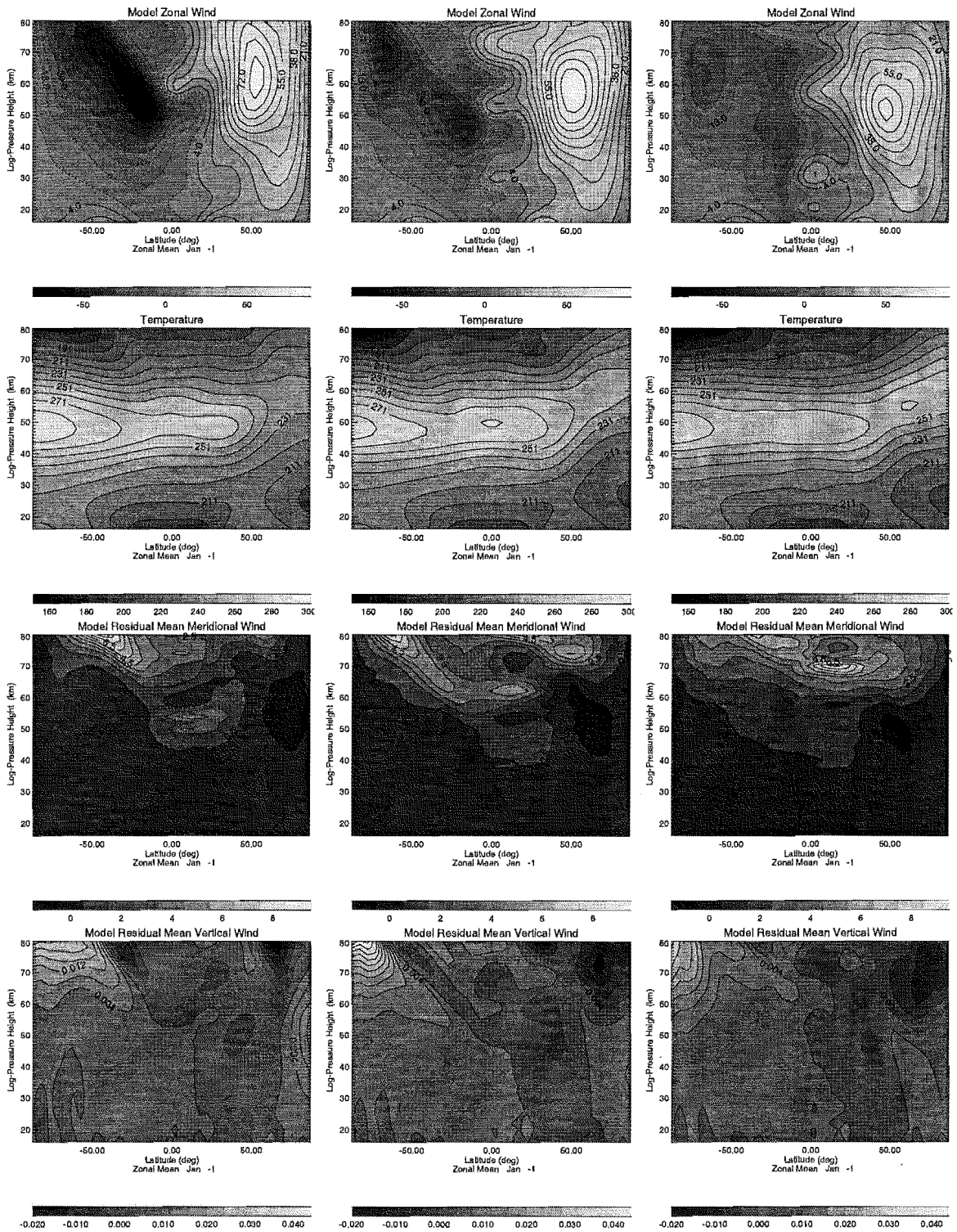

Figure 7.4: Zonal mean averages of zonal wind (m/s), temperature (K), meridional and vertical wind (m/s) from the simulations using a non-interacting gravity wave source. Strengths are $\sigma_h = 1.0$ m^2 s^{-2} $\sigma_h = 2.0$ m^2 s^{-2} $\sigma_h = 4.0$ m^2 s^{-2} respectively, during January.

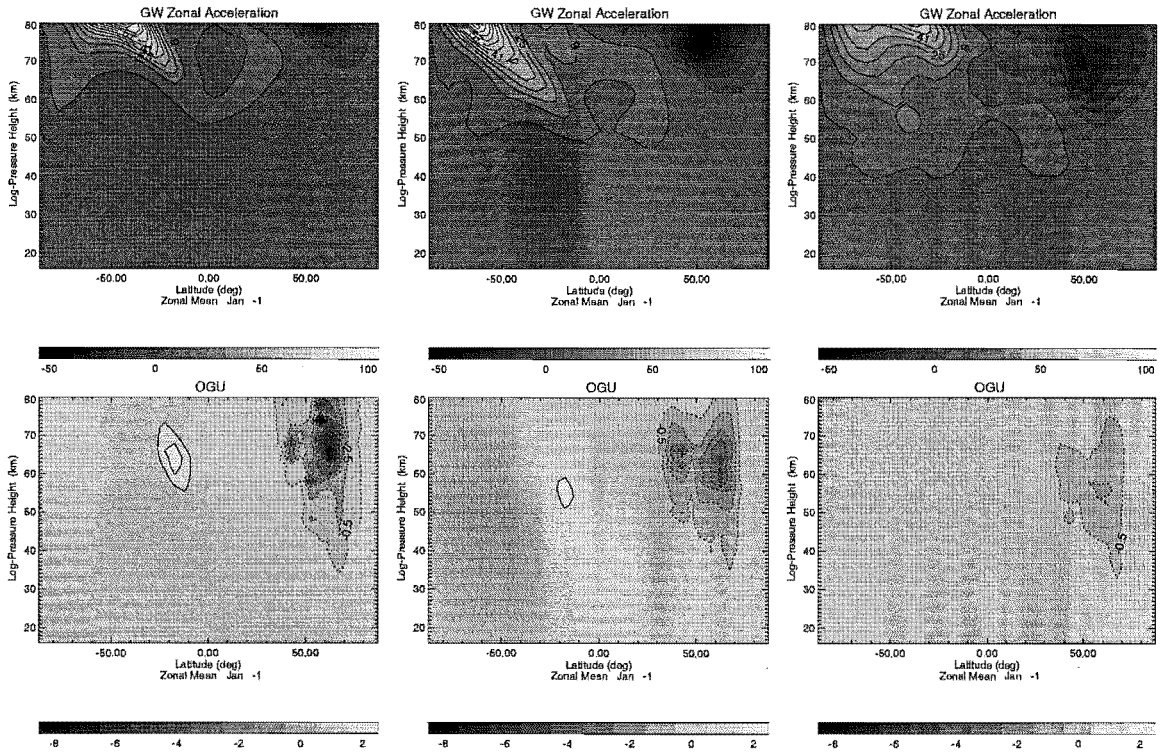

Figure 7.5: Zonal mean averages of gravity wave drag (m/s/day) (from a broad spectrum and orographic source) from the simulations using a non-interacting gravity wave source. Strengths are $\sigma_h = 1.0\ \mathrm{m^2\,s^{-2}}$, $\sigma_h = 2.0\ \mathrm{m^2\,s^{-2}}$ $\sigma_h = 4.0\ \mathrm{m^2\,s^{-2}}$ respectively, during January.

Related directly to changes in the temperature field are the zonal winds, where the southern westerly jet descends and weakens in an analogous manner to the westerly jet for the January case. This would also appear to explain the drop off in the amount of orographic drag, in this case over the Antarctic Peninsula, where the critical level processes are more than likely occurring lower in the stratosphere.

Results in the northern hemisphere (April) must be taken with caution due to the presence of the stratospheric final warming which occurs during these times. These relate to the final reversal in sign of the prevailing westerlies to easterlies which arise due to the change in the north-south temperature gradient. Sudden warmings which occur during the winter months, can also bring about a reversal in wind direction and it is thought that the final warming is a sudden warming which does not revert back to westerlies. It was noticed that the onset of the final warming was brought forward 1-2 weeks within each modelled year between the $\sigma_h = 1.0\ \mathrm{m^2\,s^{-2}}$ and $\sigma_h = 2.0\ \mathrm{m^2\,s^{-2}}$ sourced simulations. This was largely reversed between the $\sigma_h = 2.0\ \mathrm{m^2\,s^{-2}}$ and $\sigma_h = 4.0\ \mathrm{m^2\,s^{-2}}$ simulations, where the onset was put back towards the end of April.

In comparison to the CIRA86 data it is found that the trend to higher temperatures in the lower stratosphere with an increased source strength brings them more in line with *observations*. However, it would appear that this is at the expense of the temperature

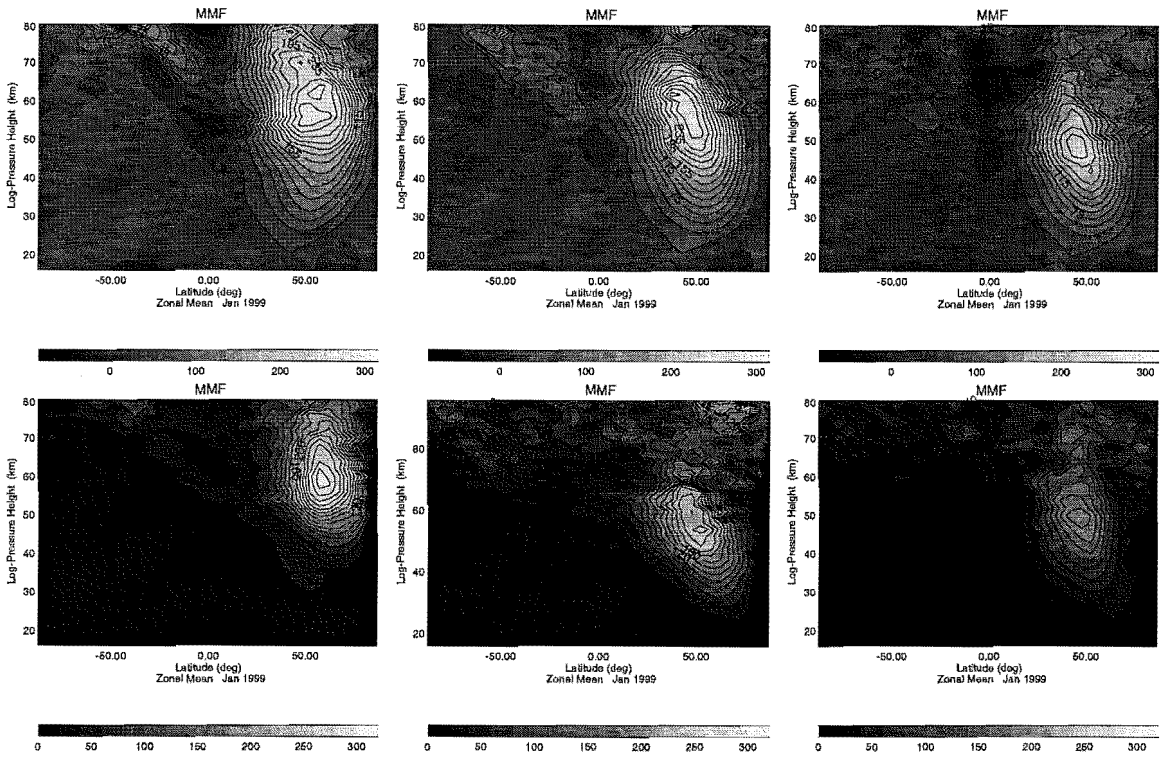

Figure 7.6: Zonal mean averages (top) and standard deviations (bottom) of model resolved wave momentum flux ($\overline{u'v'}$) during January. Strengths are $\sigma_h = 1.0$ m^2 s^{-2}, $\sigma_h = 2.0$ m^2 s^{-2} $\sigma_h = 4.0$ m^2 s^{-2} respectively.

at the southern polar stratopause which is increasingly warm and not in agreement with observations. The relative height of this part of the stratopause is also lowered which is more in line with both CIRA86 and UKMO assimilated datasets. The northern lower stratosphere is affected little by the change in mean gravity wave source strength but is consistently cooler than both datasets (e.g. Appendix D.)

The change to decreased zonal winds with a lower jet core using increased source strengths is not in agreement with the CIRA86 dataset. The more realistic simulation producing a suitably elevated southern jet runs with the lowest source strength. However, this also displays an unusually high southern polar stratopause, thus the temperature and wind fields which are coupled via thermal wind are not modelled correctly in all simulations.

It should be cautioned though that there is by no means consistent agreement between the CIRA86 and UKMO assimilated datasets. Firstly, the former were compiled over a limited 4 year period and display a mesospheric state taken from retrieved temperature data and with winds (calculated accordingly) assumed in geostrophic balance - derived wind weaker than actual wind. There are differences which include for climatological April a consistently warmer stratopause in the former dataset.

During July one again witnesses a descent of both broad spectrum and orographic

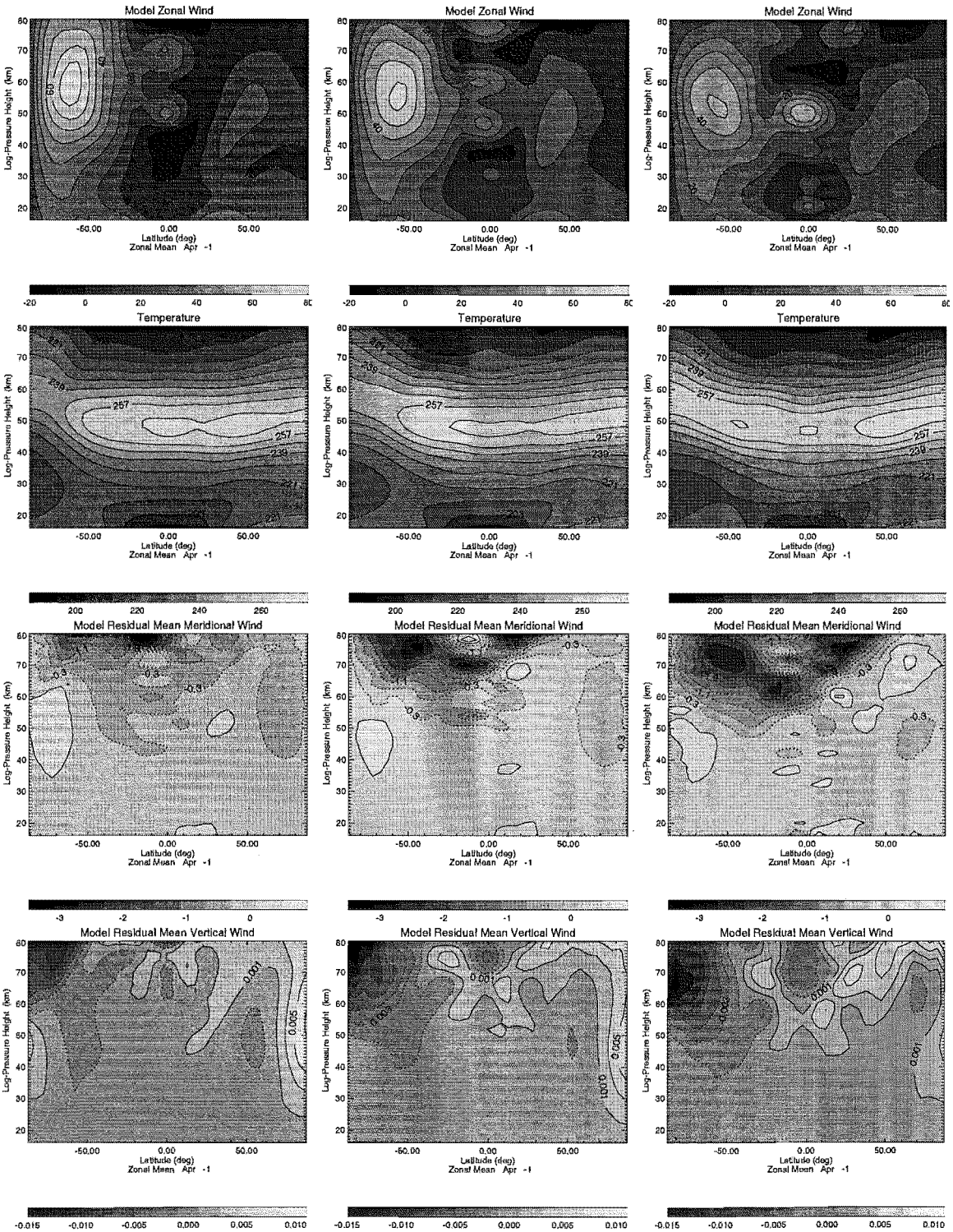

Figure 7.7: Zonal mean averages of zonal wind (m/s), temperature (K), meridional and vertical wind (m/s) from the simulations using a non-interacting gravity wave source. Strengths are $\sigma_h = 1.0\ \mathrm{m^2\,s^{-2}}$ $\sigma_h = 2.0\ \mathrm{m^2\,s^{-2}}$ $\sigma_h = 4.0\ \mathrm{m^2\,s^{-2}}$ respectively, during April.

drag between simulations. However the effects seen in the modelled climate is different to that seen during January. The main trends of mesospheric warming/cooling in the winter/summer hemispheres is still seen, although the extent of this is considerably enhanced

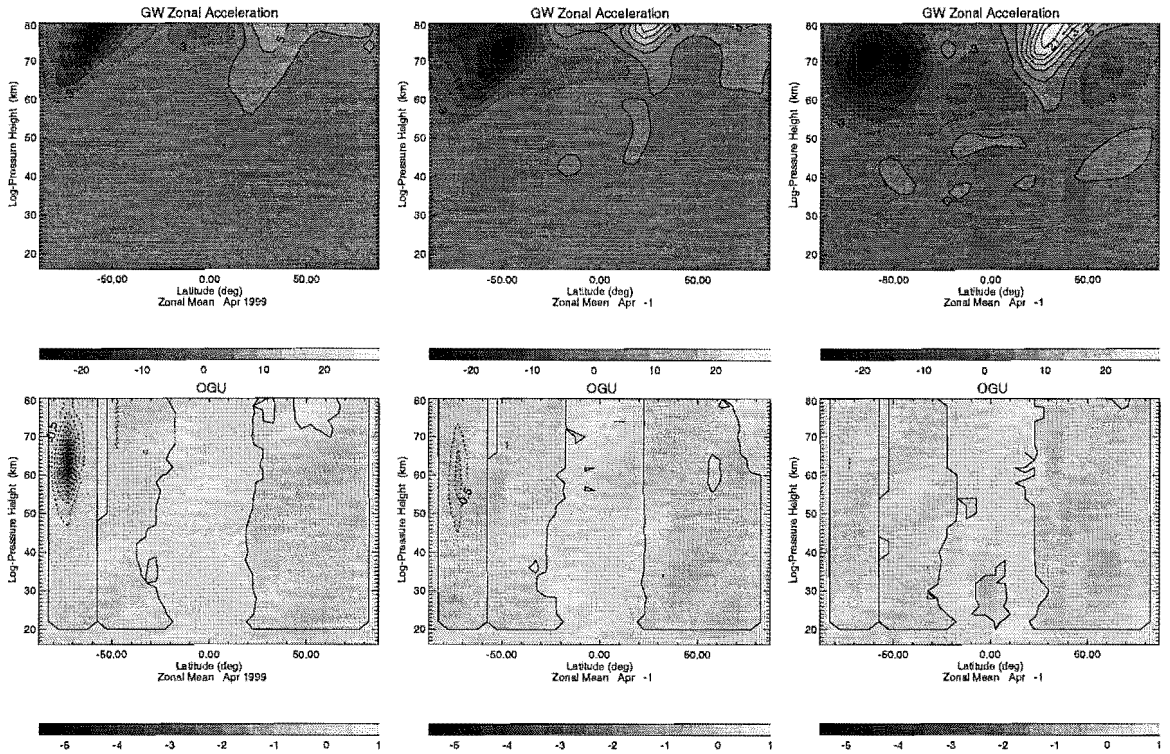

Figure 7.8: Zonal mean averages of gravity wave drag (m/s/day) (from a broad spectrum and orographic source) from the simulations using a non-interacting gravity wave source. Strengths are $\sigma_h = 1.0$ m^2 s^{-2}, $\sigma_h = 2.0$ m^2 s^{-2} $\sigma_h = 4.0$ m^2 s^{-2} respectively, during April.

during the month (figure 7.9,7.10).

The summer temperature trend is consistent with the southern stratopause descending in height with increased σ_h. The southern winter mean conditions differ appreciably to those seen during the northern winter. Temperatures are generally warmer at higher σ_h throughout most of the stratosphere and mesosphere, with appreciable differences between simulations occurring at the model bottom. Associated with this is a weakening in the meridional temperature gradient which (via thermal wind) greatly reduces the strength of the polar night jet. Though this feature does occur in the winter north (January), it does not occur to the same extent as it does in July. Again, a reduction in the height of peak orographic drag is also seen.

In comparing the modelled trend to the *observational* datasets the southern polar temperatures are still in disagreement. Although the trend to a warmer winter mesosphere is more in accord to what is seen observationally the winter stratopause is again too warm and high. Lower down, in the polar winter stratosphere, temperatures are too cold also. This has a direct bearing on the strength of the polar night jet which is stronger in the two lower strength simulations.

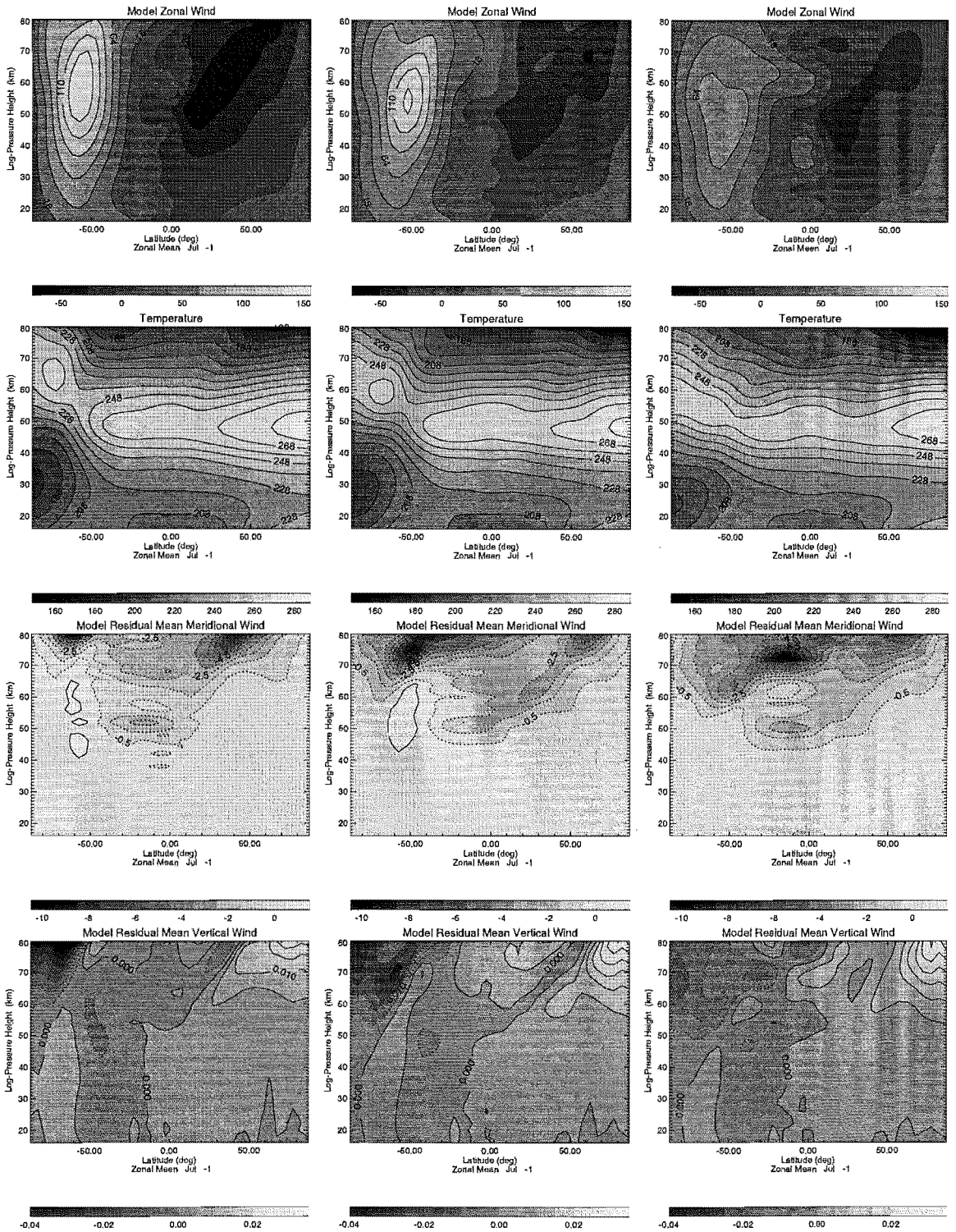

Figure 7.9: Zonal mean averages of zonal wind (m/s), temperature (K), meridional and vertical wind (m/s) from the simulations using a non-interacting gravity wave source. Strengths are $\sigma_h = 1.0\ \mathrm{m^2\,s^{-2}}$ $\sigma_h = 2.0\ \mathrm{m^2\,s^{-2}}$ $\sigma_h = 4.0\ \mathrm{m^2\,s^{-2}}$ respectively, during July.

7.2.2 Interaction between Gravity Waves

A simulation was carried out using the Doppler Spread Parameterisation of Hines. A global mean source of waves (broad spectrum) was combined with an *interacting* source

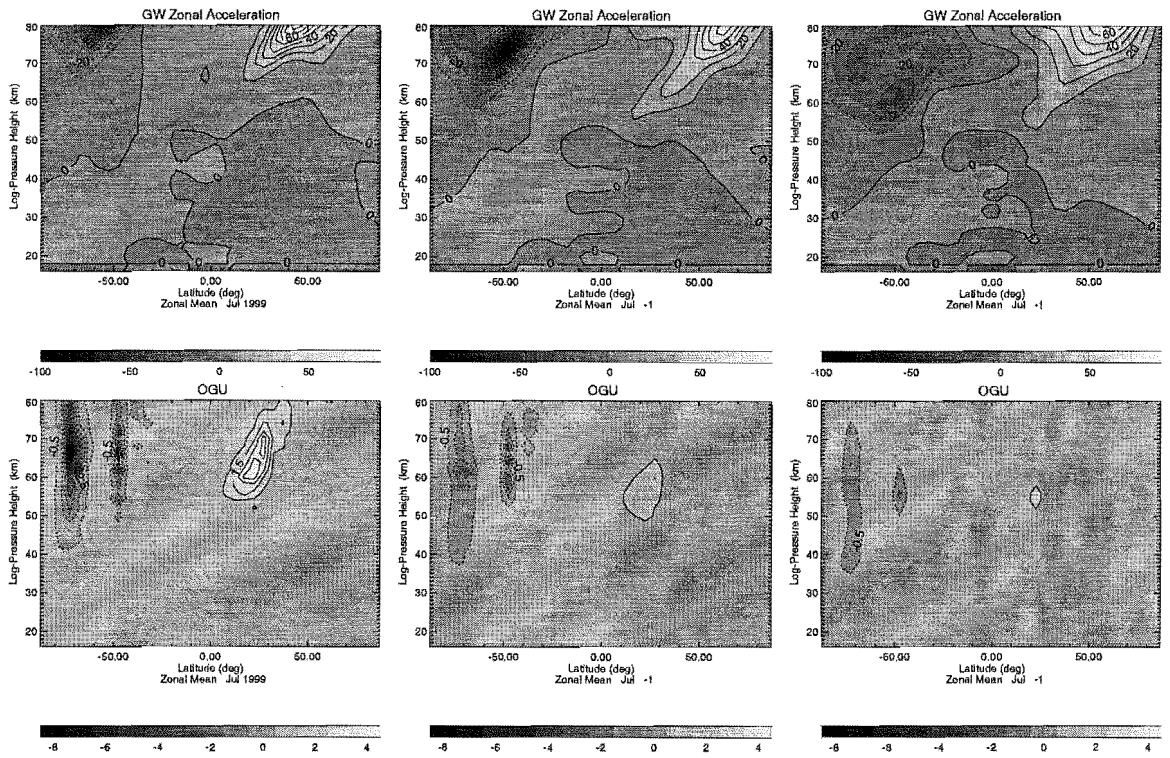

Figure 7.10: Zonal mean averages of gravity wave drag (m/s/day) (from a broad spectrum and orographic source) from the simulations using a non-interacting gravity wave source. Strengths are $\sigma_h = 1.0\ \mathrm{m^2\,s^{-2}}$, $\sigma_h = 2.0\ \mathrm{m^2\,s^{-2}}$ $\sigma_h = 4.0\ \mathrm{m^2\,s^{-2}}$ respectively, during July.

of mountain waves. The strength of the former (as encapsulated by the parameter σ_h^2 - the total wind variance of the spectrum of waves) was set to $1\ \mathrm{m^2\,s^{-2}}$, at a height of 10 km and suitably extrapolated up to 16 km - the bottom-most level of the SMM. A six year run was performed starting from 7 November 1991. UKMO data was used to initialise the run and daily boundary fields of: geopotential, temperature and zonal/meridional wind were employed at the models lower boundary to simulate resolved tropospheric wave activity. The output was then compared to a similar simulation where there was no modelled interaction between the two sources of gravity waves (that is, fields from the non-interacting simulation were subtracted from those output from the interacting simulation).

Figure 7.11 highlights these differences and should be compared with the same strength run in figures 7.4 and 7.5. It is immediately apparent that the differences are small. In fact, the differences lie within one standard deviation of each of the fields and so one cannot state the simulations are statistically different (figure not shown). This is in line with the findings of chapter 5.2 where it was found that during solstice times the dominant effect on both broad spectrum and orographic waves were through the background wind.

It is noticed that there appears to be very little (if any) sympathetic broad spectrum drag located alongside that from the orography. In chapter 5.2, it was suggested that

this was an effect linked with the mutual interaction between the two sets of waves. It is seen that differences in broad spectrum drag are minor compared with those from the orography. This is explained by the localised nature of the orographic drag. In practise these drags would be very much larger than those from the broad spectrum (at these heights) and so would appear above these in any zonal averaging. One would at first conclude that the differences seen in these plots can more than likely be put down to a slight change in height of dissipation of the orographic waves. This would have a slight influence on the strength and position of the polar night jet which is seen in the dipole character of the zonal wind differences. These would have follow on effects on both the temperature and residual circulation.

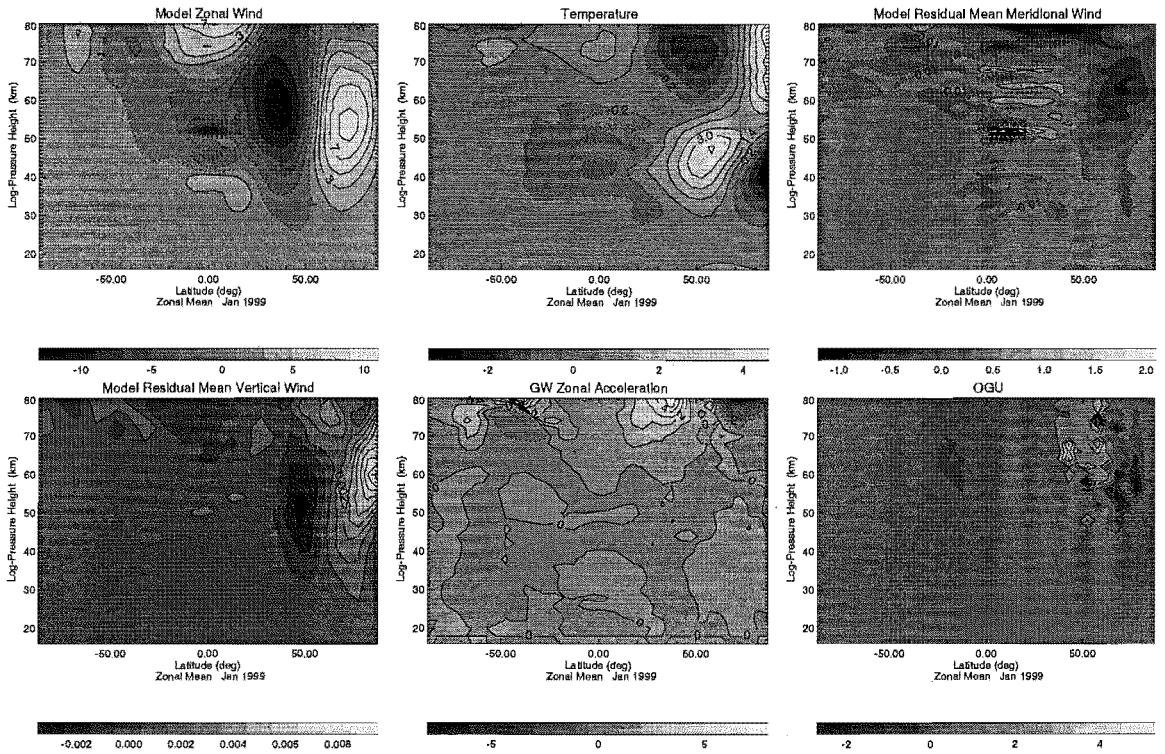

Figure 7.11: Zonal mean differences of zonal wind (m/s), temperature (K), meridional/vertical wind (m/s) and broad-spectrum/orographic gravity wave drag (m/s/day) between the simulations using an interacting/non-interacting gravity wave source. Broad spectrum strengths are $\sigma_h = 1.0\ \mathrm{m^2\,s^{-2}}$, during January

During April (figure 7.12), it is noticed that the dipole feature in the zonal wind differences persists even in the absence of any noticeable orographic driving. These differences are still very small and still lie within a standard deviation of the fields (not shown), which are relatively large at these times due to final warmings which occur during the northern spring. The change in position of the polar night jet can possibly be attributed to differences in broad spectrum drag occurring in the northern mesosphere. These slight differences would cause minor changes in the residual circulation and thus heating budget in these regions. This would show as a change in zonal circulation via thermal wind.

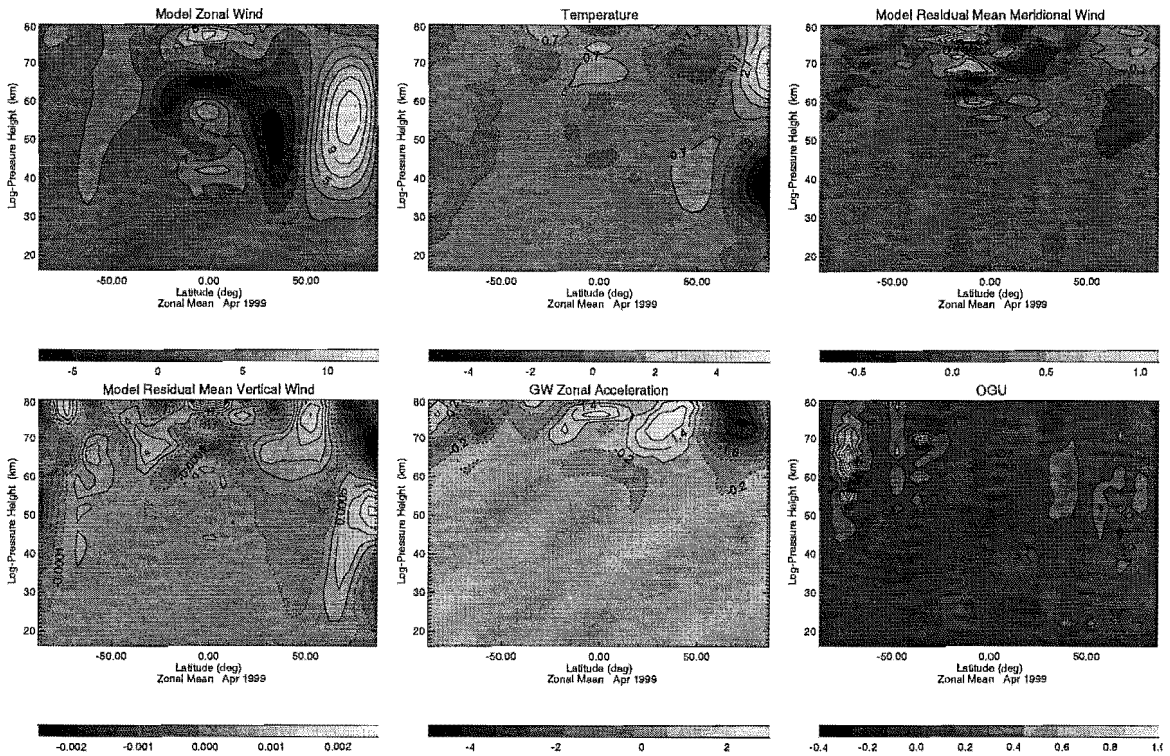

Figure 7.12: Zonal mean differences of zonal wind (m/s), temperature (K), meridional/vertical wind (m/s) and broad-spectrum/orographic gravity wave drag (m/s/day) between the simulations using an interacting/non-interacting gravity wave source. Broad spectrum strengths are $\sigma_h = 1.0$ m^2 s^{-2}, during April.

During July (figure 7.13) further differences are seen about the polar night jet. These are consistent with a slight poleward shift in the position of the jet, due to slight changes in circulation from orographic drag originated from, most probably, the Antarctic Peninsula. The changes in the residual mean circulation are small compared to the mean values from the individual fields themselves ($< 10\%$). However, differences in temperature in the stratospheric polar south are seen to be of the order of a degree or two in the mid to lower stratosphere. This may have an influence in the formation of frozen particulates where heterogeneous ozone reactions take place in the spring. However, just as in the previous two seasonal cases, there would not appear to be significant differences from incorporating an *interacting* orographic gravity wave source. It must be noted though that the inclusion of an orographic source is important in reducing the strength of the polar night jet and giving rise to localised stratospheric circulation.

7.2.3 Tropospheric Launch Height

It is currently accepted that models implementing a launch height for gravity waves low in the troposphere generally simulate an improved middle atmospheric state. In a study by *Manzini and McFarlane* (1998) it was found that the southern cold winter bias in stratospheric temperature was largely rectified when their prescribed gravity wave source

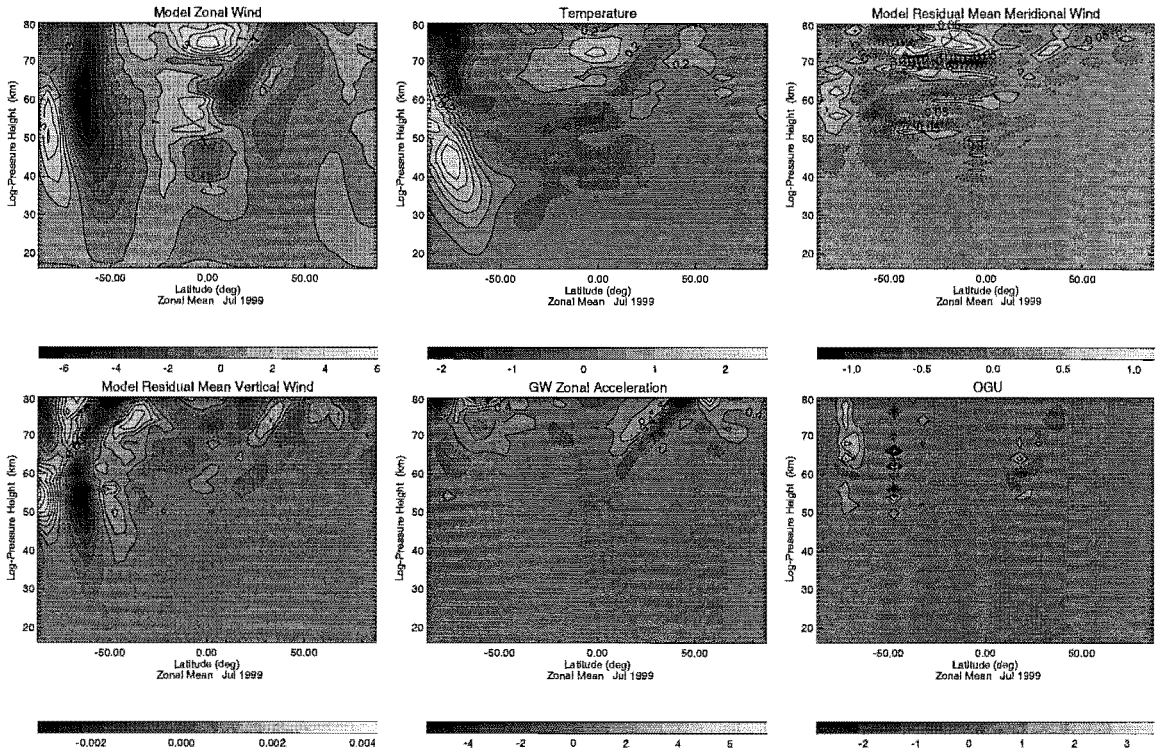

Figure 7.13: Zonal mean differences of zonal wind (m/s), temperature (K), meridional/vertical wind (m/s) and broad-spectrum/orographic gravity wave drag (m/s/day) between the simulations using an interacting/non-interacting gravity wave source. Broad spectrum strengths are $\sigma_h = 1.0\ \mathrm{m^2\,s^{-2}}$, during July.

was launched near the ground. They also noted a strengthening of summer mesospheric easterlies, in accord with observations. Such a launch height also results in there being a negative gravity wave momentum flux above the tropospheric jets which has been seen in observations recently by *Vincent et al.* (1997) in the lower stratosphere. Such a source would also result in an acceleration of summer stratospheric jet which is thought to occur (*Alexander and Rosenlof* (1996)).

In chapter 6 it was found that not only could the mean wind introduce asymmetries into the gravity wave spectrum but so could the large scale stationary wave structures. It was seen that a stationary wave one signal could be carried by gravity waves leaving the stratosphere but it remained to be seen whether this signal could, upon dissipation, force a wave one signal in wind in the mesosphere. More noteworthy would be if such a signal could be driven in the summer mesosphere from dissipation of gravity waves originating from the troposphere.

To test this assertion, a boundary gravity wave source was constructed for inclusion in the SMM from filtering an isotropic source of gravity waves in the same manner as mentioned in chapter 6. The launch height was taken to be 2 km and output was removed from 16 km - corresponding to the bottom-most level of the SMM. Six years of daily data was compiled and then incorporated into the SMM along with the default boundary fields

of geopotential, temperature and wind (needed to reproduce other tropospheric wave phenomena which would otherwise not be forced). It should be stated that this boundary included the total gravity wave momentum flux, not just the wave one component. The zonal wave one component of this source can be seen in figure 7.14. Unlike the results of chapter 6, the meridional component was considerably smaller than the zonal one.

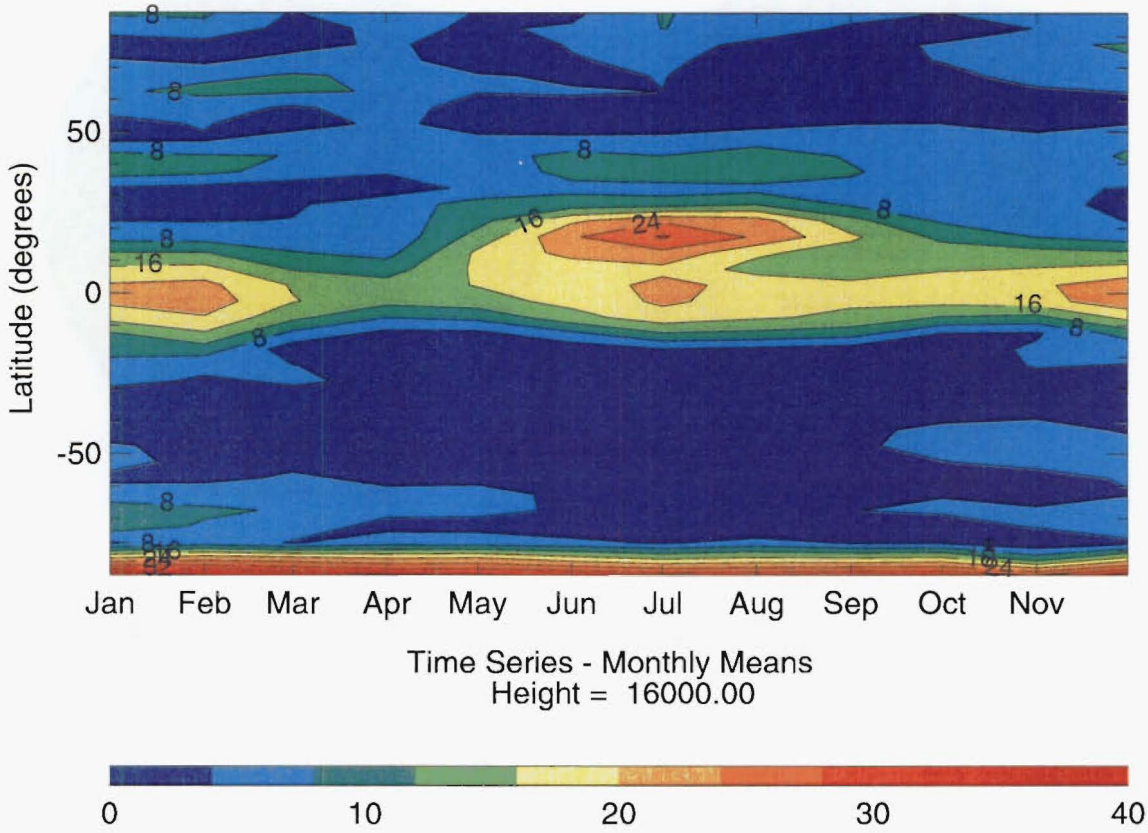

Figure 7.14: Timeseries at 16 km showing the horizontal structure of wave one zonal momentum flux ($\times 10^{-5}$Pa) calculated using a tropospheric launch height for gravity waves of 2 km.

The gravity wave source at 2 km comprised waves having a total wind variance of 1 $m^2 s^{-2}$ with a characteristic horizontal wavelength of 900 km. As before a low m spectral slope of one was assumed. However, so as to help facilitate a sizable forcing in the mesosphere, no low wavenumber cutoff was employed. It is thought that only those waves travelling fastest will survive to these heights - these are waves having the largest vertical scale. The values of the various adjustable parameters were unchanged from those stated in chapter 5. No orographic waves were included in the simulation. The simulation was run for 6 years between 1991-1997 and the output averaged to give a climatological mean of monthly averages.

It can be seen from figure 7.14 that peaks in wave one gravity wave activity occur most notably about 20 °N during the northern summer. A minor peak occurs at the same time but at the higher latitude of about 40 °N. It would appear that these signals

are linked with the Asian monsoon and the Tibetan high which occurs at these latitudes and times. The Tibetan high is characterised by low values of static stability and its geographic extent is large (figure 7.15).[6]

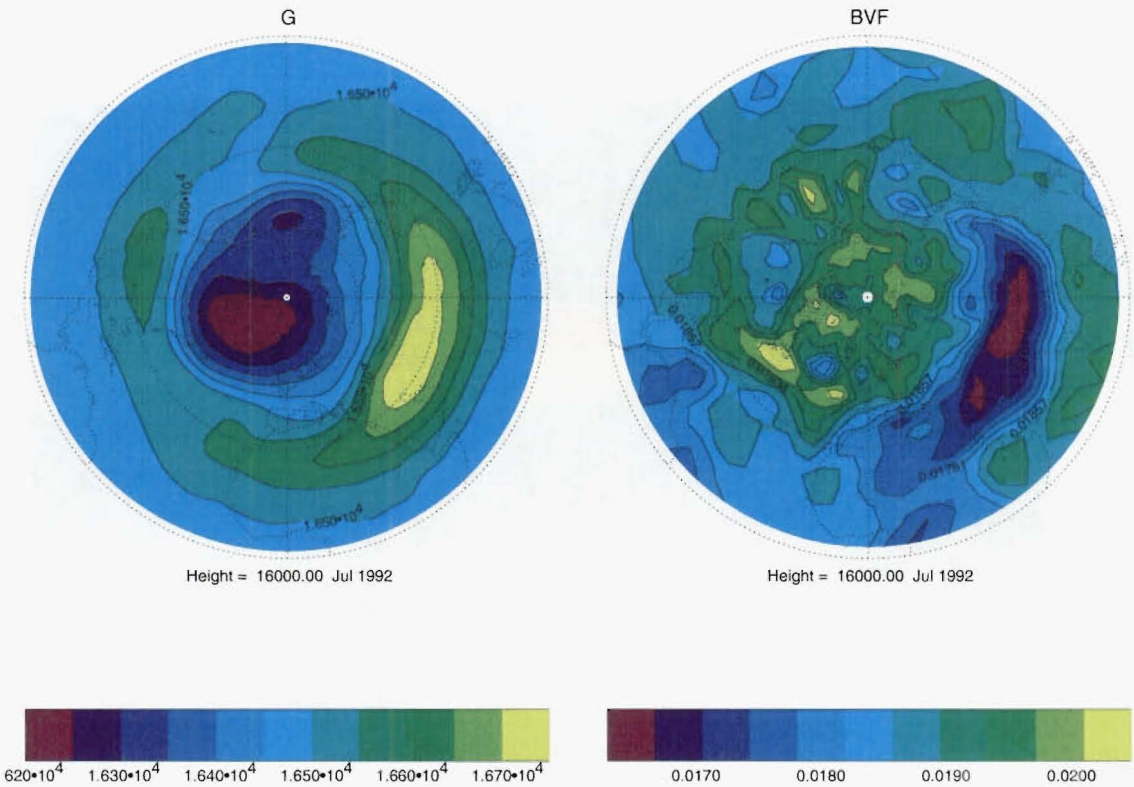

Figure 7.15: Data from the UKMO assimilated dataset showing northern hemisphere geopotential height (m) and Brunt-Väisälä frequency (Hz) at a height of 16 km, during July (1992). The Tibetan high can be seen over the Indian sub-continent with an angular extent of $> 90°$.

The wind associated with this high could conceivably force a low wavenumber planetary signal in a tropospheric gravity wave source. The relatively low static-stability associated with this feature (as shown by values of Brunt-Väisälä frequency above) would reinforce any large-scale feature imprinted in a tropospheric gravity wave source propagating up from below (refer to equation 4.4 and chapter 6). Evidence of such a process occurring can be seen at 37.5°N (figure 7.16), where a wave one forcing does indeed occur from May through August peaking at 85 km at a magnitude of 40 m/s/day. The nature of this forcing is analogous to the mean wave forcing at the same latitude which peaks in the same season several kilometres higher and at twice the magnitude of those from the wave one field.

It is seen that these forcings are producing a wave one response in the zonal winds at this latitude (figure 7.17). By examination of the mean zonal wind, the origin of this wave one wind structure becomes apparent. At underlying heights the zonal wind is

[6]Shown here is a high in geopotential height (*Tibetan high*), however lower down there is an associated low, called the *Tibetan low*.

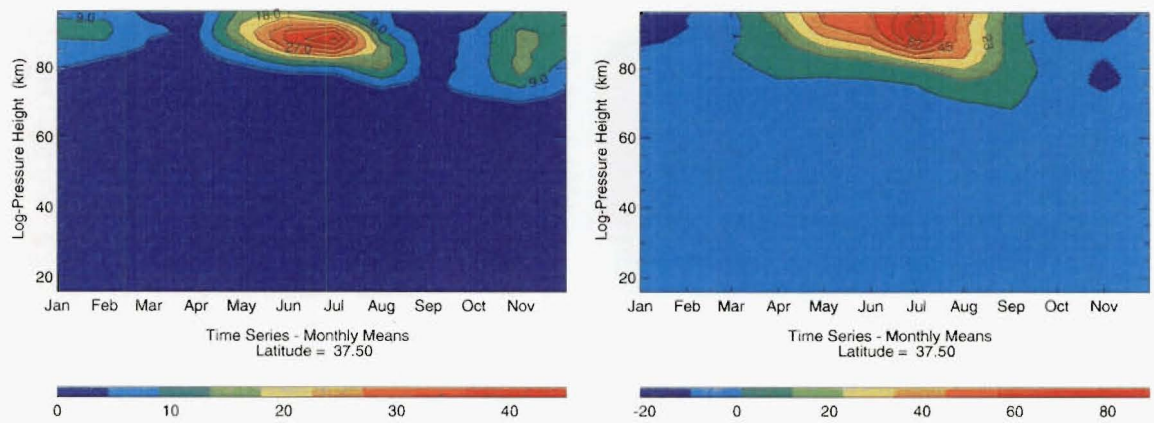

Figure 7.16: SMM timeseries at 37.5°N showing the vertical structure of zonal wave number one (top left) and mean (top right) gravity wave drag (m/s/day) calculated from the simulation launching a tropospheric gravity wave source.

predominantly westward in sign, which from theory (equation 2.18) precludes the passage of any tropospheric Rossby wave - either stationary or travelling. Although attenuated throughout the stratosphere (refer to chapter 6), the spectrum of gravity waves is able to carry its wave one tropospheric signal through the regime of westward winds and force a wave number one structure at overlying heights. These smaller scale gravity waves are breaking due to a combination of the zonal wind shear becoming positive above the jet core and non-linear wave-wave interactions becoming significant at these heights due to the decrease in air density (refer to section 5.1). These winds are of the same magnitude as those found by *Wang et al.* (2000), although they are in the northern hemisphere.

It is important to note that during these times a two-day-wave is seen observationally at these heights (section 2.6). It has been suggested that the existence of this could be due to baroclinic instability caused by the effect of gravity wave drag on the latitudinal temperature gradient - a reversal in the meridional temperature gradient (compared to in the stratosphere) at mesospheric heights is attributed to breaking gravity waves. The origin of the feature here, though, is not linked entirely with a baroclinic instability as the region of wave one drag is located together with wave one signal in winds, suggesting that the wave drag is directly driving these large-scale winds.

These results are obtained using crude assumptions about the tropospheric source of gravity waves and suggests that it is most likely the tropospheric state and not the exact makeup of the source which give these. However, such claims should be tempered until more is known about the exact geographic and spectral makeup of any tropospheric source of waves.

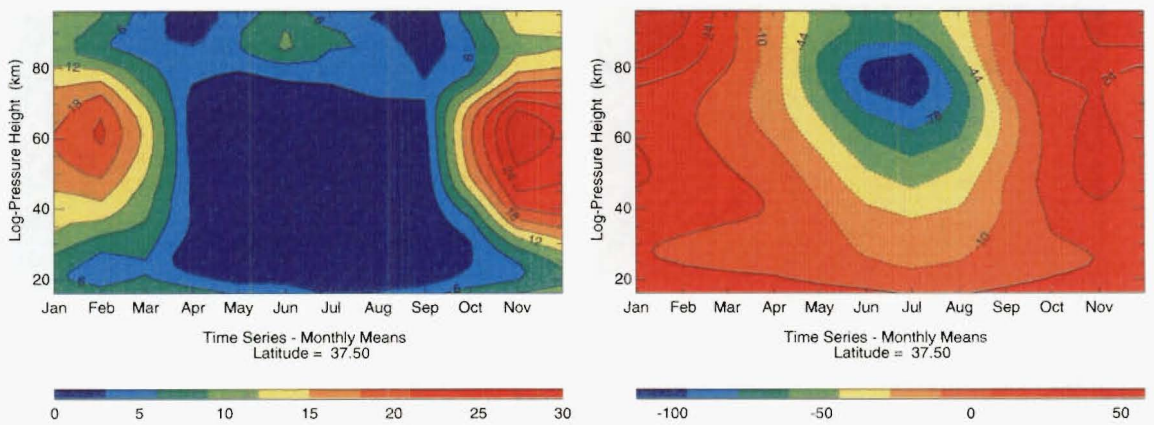

Figure 7.17: SMM timeseries at 37.5°N showing the vertical structure of zonal wave-one/mean wind (m/s) calculated from the simulation launching a tropospheric source of gravity waves.

7.2.4 Geographic Changes in Source Strength

The previous assumption about a globally homogeneous valued source for gravity waves is a crude one to make and is at odds with observation. *Allen and Vincent* (1995) conducted the first systematic study comparing a number of sites in and about Australia for gravity wave activity. In that study they found a correlation between the location of particular sites to the observed normalised temperature variance in the lower atmosphere (an indicator of the strength of wave activity). Tropical sites appeared to have consistently higher values of this compared to those from higher latitudes. This would be consistent with greater convection at such tropical locations and thus associated wave activity.

As a first step towards refining the prescribed global gravity wave source, a further set of simulations were conducted imposing a simple trigonometric relationship on the strength of the global source of gravity waves. As before the Hines DSP was used, with its source parameter, σ_h varied as $0.5 + \cos(latitude)$ as seen by figure 7.18. This form was chosen to emphasise tropical locations over extratropical ones as found by *Allen and Vincent* (1995). As before, other Hines specific parameters were set as in chapter 5.

To help gauge the model differences introduced using a geographically varying source of gravity waves, a comparison was made with the simulation running a globally homogeneous, interacting source of orographic and broad spectrum waves, with a total wave wind variance of $\sigma_h = 1\,\mathrm{m^2\,s^{-2}}$. Figure 7.19 shows results from this simulation for climatological January; six year simulations were again completed. It is noticed that the northern winter jet is slightly stronger in the geographically varying case. This is consistent with a weaker source poleward of approximately 60°N. Greater westward directed momentum flux is able to close off more of the polar night jet when it is deposited in the mesosphere, as is seen from the broad spectrum drag. This has the added effect of driving slightly greater descent over the polar north which induces slightly warmer temperatures there. Furthermore these temperature changes are seen down as low as 30 km. Over the southern

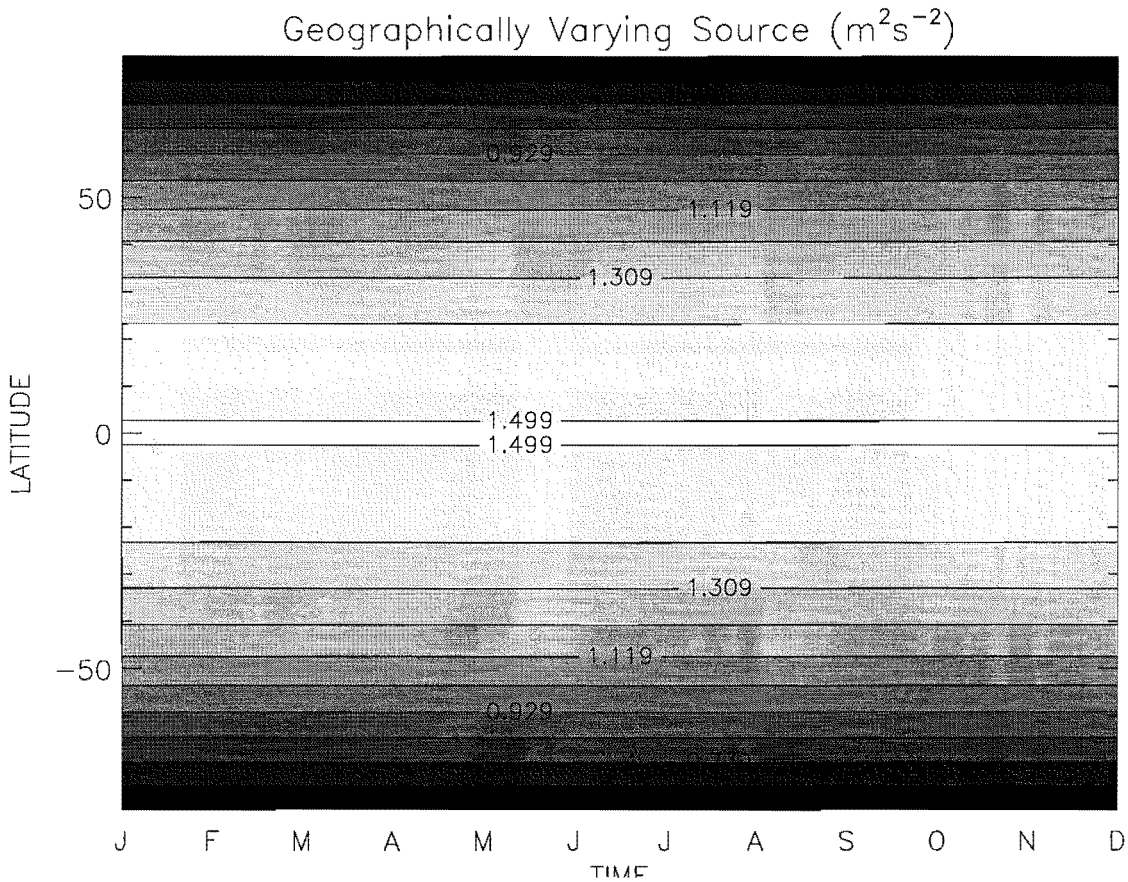

Figure 7.18: Global values of σ_h at 16 km for the simulation utilising a geographically varying source of gravity waves of the form $0.5 + \cos\phi$.

summer pole, a slight cooling is observed in the mesosphere, however this effect is very slight. This can be seen linked to noticeable increases in southern upwelling (rising air). The rising motion over the northern stratospheric pole which is associated with sudden warmings during the month is similar between the two simulations.

In comparison with the observational datasets, it is once again seen that most of the polar winter middle atmosphere is cooler than expected. There is a slight improvement in temperatures for the homogeneous sourced run but this is expected due to it having a stronger polar gravity wave source. The zonal winds (both hemispheric jets) are stronger than the observations and the polar night jet does not exhibit an equatorward tilt as is displayed in the CIRA86 data. Such a short coming is common amongst many present day atmospheric models.

During April, the stratospheric north looks similar between simulations. This month is significant in that a reversal in the meridional temperature gradient, accompanied by a change in sign of the zonal wind jets dominates the dynamics of the middle atmosphere. The onset of the southern winter westerly jet appears to be the major difference during the month. As was the case with the winter north, the southern *winter* jet which is beginning

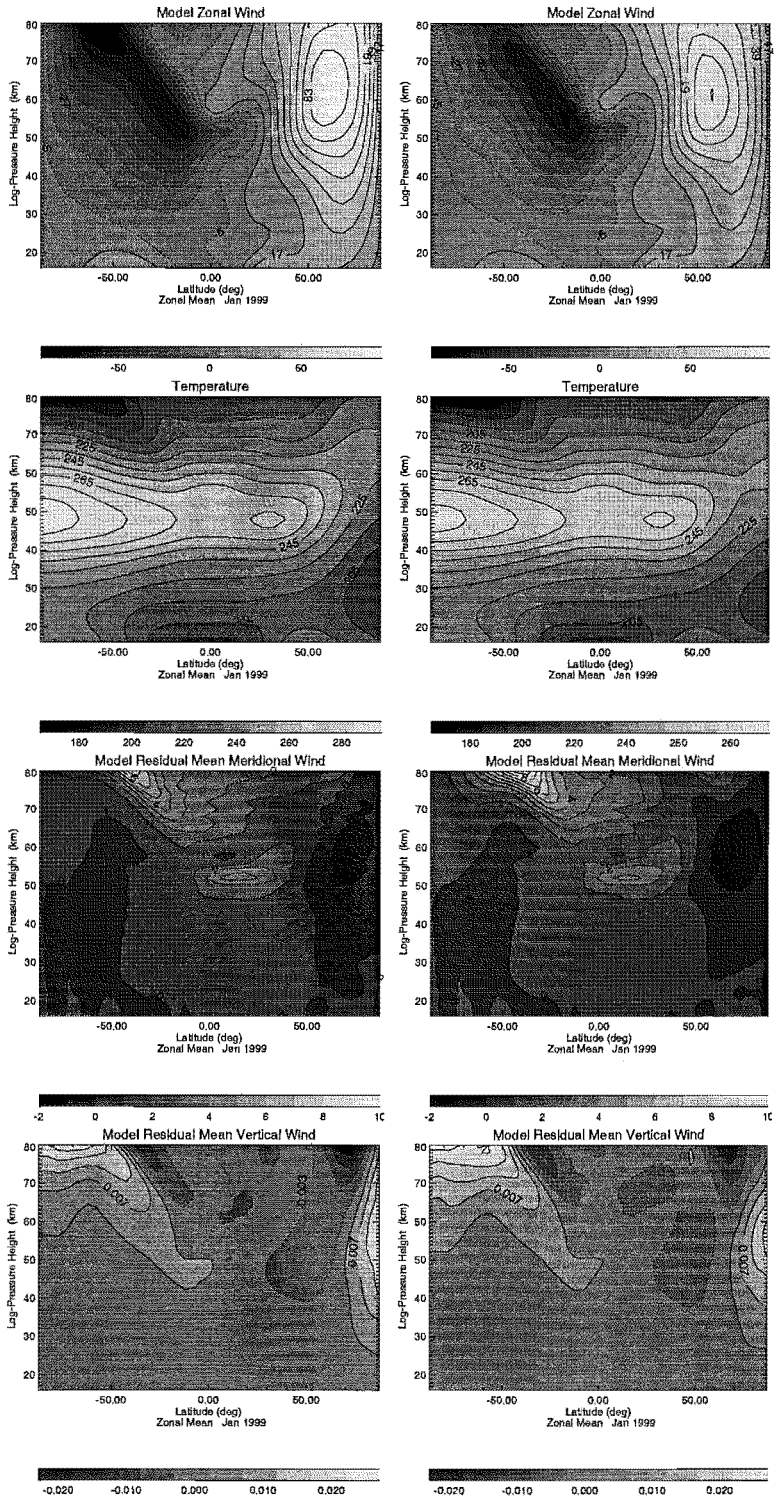

Figure 7.19: Zonal mean averages of zonal wind (m/s), temperature (K), meridional and vertical wind (m/s) from the simulations using a geographically varying and global mean source, respectively. Strengths are $\sigma_h = 0.5 + \cos\phi$ m^2 s^{-2} and $\sigma_h = 1.0$ m^2 s^{-2} respectively, during January.

to form is weaker in the geographically varying simulation, presumably for the same reason as for the northern winter jet. Associated with this is a weakened temperature gradient above the southern stratopause and stronger residual circulations. However, this alone

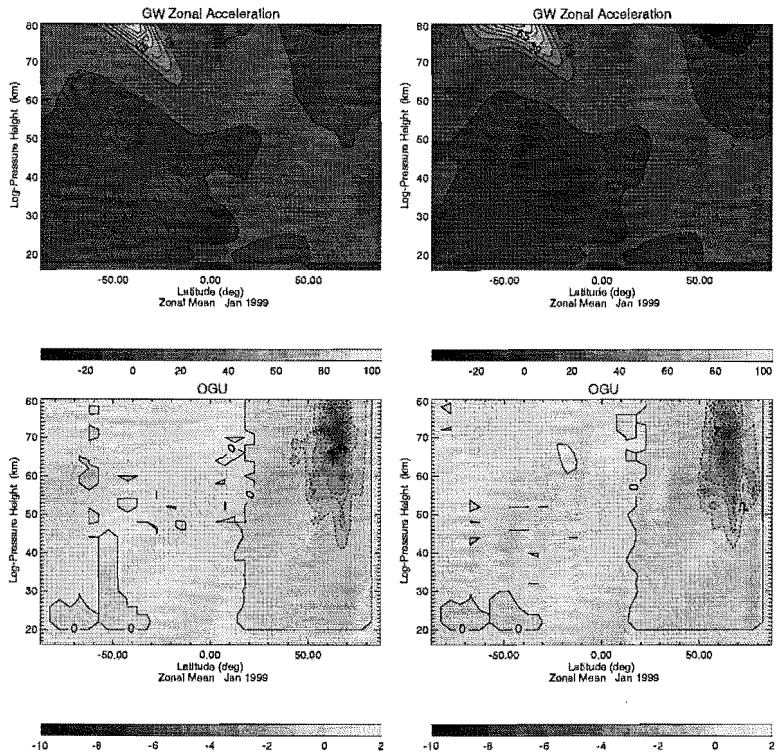

Figure 7.20: Zonal mean averages of gravity wave drag (m/s/day) (from a broad spectrum and orographic source) from the simulations using a geographically varying and global mean source, respectively. Strengths are $\sigma_h = 0.5 + \cos\phi$ m^2 s^{-2} and $\sigma_h = 1.0$ m^2 s^{-2} respectively, during January.

does not suggest an earlier time for westerly change. The orographic drag, however, is strongly influenced by the sign of the underlying winds. It is seen that this is weaker and lower down for the globally homogeneous case. This, suggests that the onset of westerly flow is earlier with a weaker source of extratropical gravity waves. This trend was seen in section 7.2.1, with the trend in greater source strength between simulations (*c.f.* figure 7.8). The strength in broad spectrum gravity wave forcing is considerably stronger in the globally homogeneous simulation. This is expected because of a stronger source at these latitudes, but may be influenced by the nature of the formation of the winter jet as the differences are more marked than the drag during the northern winter at similar heights.

The geographically varying sourced simulation appears to model the southern polar mesosphere more accurately, although displays a cooler stratopause at similar latitudes. The entire stratosphere at these latitudes is cooler than the homogeneous sourced case and further from observations. One can again put this down to the size of source at these latitudes. Both simulations display a similar extratropical northern mesosphere similar to each other and observations. The zonal winds in both simulations are slightly stronger than observed (for the CIRA86) dataset anyway and could be due to the time of onset of westerlies during the month - a later onset of westerlies will correspond to weaker average values. Higher frequency information would clear the issue, but such is not available for

this dataset.

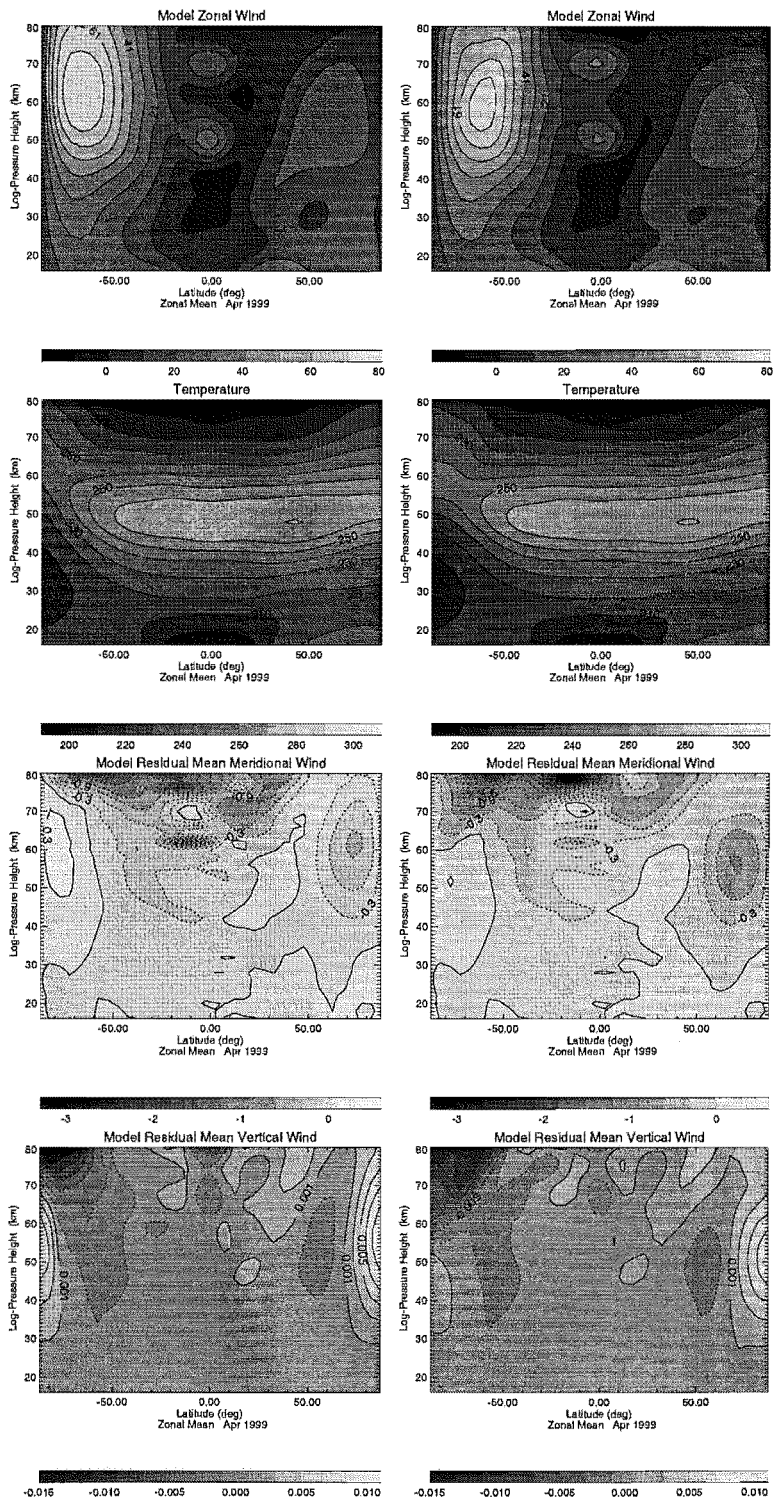

Figure 7.21: Zonal mean averages of zonal wind (m/s), temperature (K), meridional and vertical wind (m/s) from the simulation using a geographically varying and global mean source, respectively. Strengths are $\sigma_h = 0.5 + \cos\phi$ m^2 s^{-2} and $\sigma_h = 1.0$ m^2 s^{-2} respectively, during April.

Figures 7.23 and 7.24 represent the modelled atmospheric state for the month of July. The northern middle atmosphere appears very similar between the two simulations and

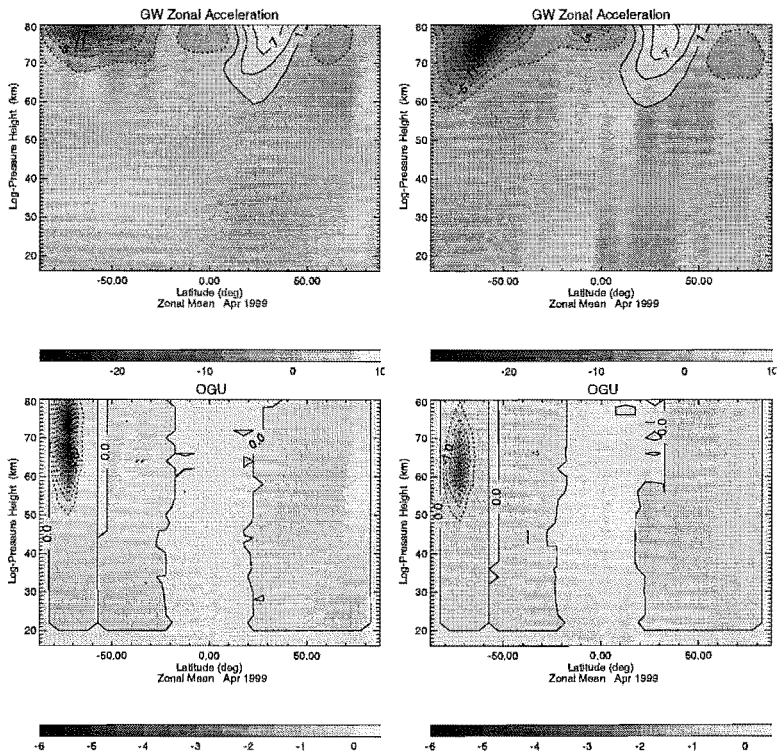

Figure 7.22: Zonal mean averages of gravity wave drag (m/s/day) (from a broad spectrum and orographic source) from the simulations using a geographically varying and global mean source, respectively. Strengths are $\sigma_h = 0.5 + \cos\phi$ m^2 s^{-2} and $\sigma_h = 1.0$ m^2 s^{-2} respectively, during April.

at a first glance so does the south. The zonal wind jets are very similar as are the residual circulations. However, it is noticed that mid to lower southern stratospheric temperatures are significantly different. There exists a 15-20 K difference in temperature. This difference is also seen in section 7.2.1 with the trend in increased source strength. There, similar differences were seen. What is different here is the fact that the sources are small at these latitudes, although they do differ by approximately 100%. The sensitivity is more apparent when one notices that the difference in temperature over the southern pole at 50 km is about 45 K between the geographically varying run and the globally homogeneous simulation with source strength of $\sigma_h = 4$ m^2 s^{-2}. These are statistically significant - the standard deviation within these simulations is less than the differences seen in figure 7.23 (not shown).

As expected, temperatures in the winter middle atmosphere are far cooler than observed. This has considerable influence on the strength of the polar night jet which is considerably stronger than what is observed. The north is modelled well except for the polar northern lower stratosphere which is cooler and a weaker modelled summer jet.

Timeseries of the tropical state show no significant differences and also do not model this region well. The semi-annual oscillation produced (in both simulations) achieves the desired frequency but fails to reproduce desired wind strengths. There is also no sign of

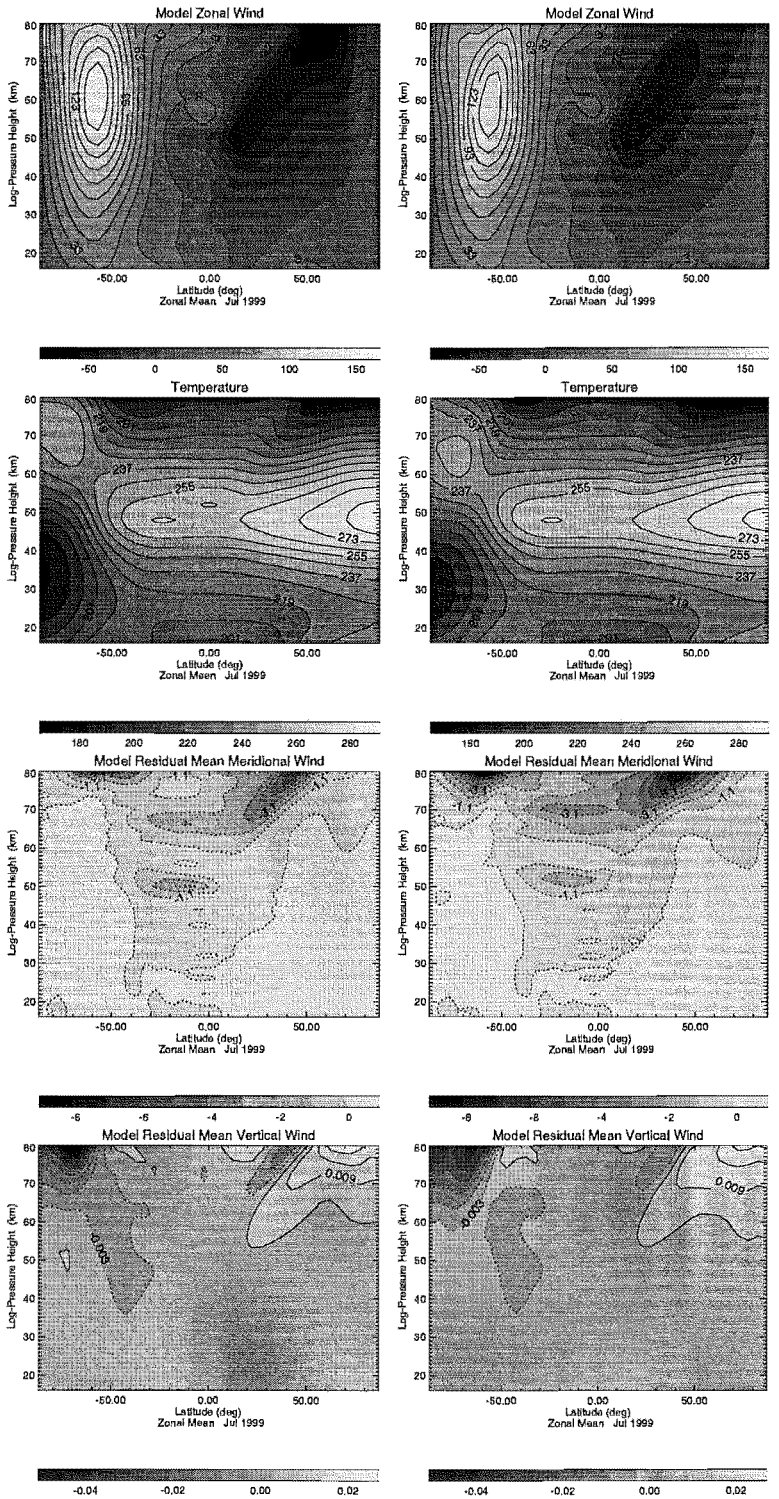

Figure 7.23: Zonal mean averages of zonal wind (m/s), temperature (K), meridional and vertical wind (m/s) from the simulations using a geographically varying and global mean source, respectively. Strengths are $\sigma_h = 0.5 + \cos\phi$ m^2 s^{-2} and $\sigma_h = 1.0$ m^2 s^{-2} respectively, during July.

a quasi-biennial oscillation in the lower stratosphere in either simulation.

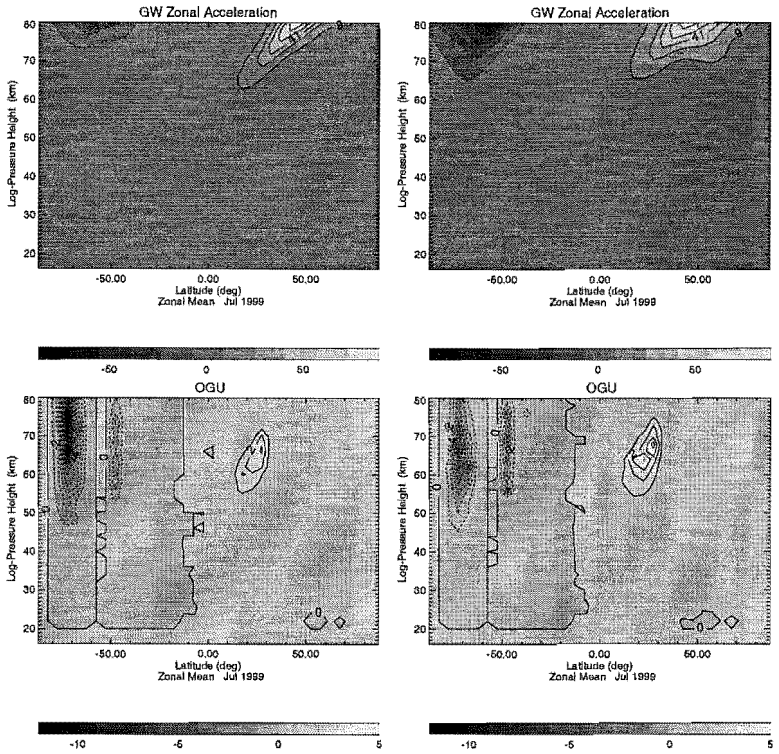

Figure 7.24: Zonal mean averages of gravity wave drag (m/s/day) (from a broad spectrum and orographic source) from the simulations using a geographically varying and global mean source, respectively. Strengths are $\sigma_h = 0.5 + \cos\phi$ m^2 s^{-2} and $\sigma_h = 1.0$ m^2 s^{-2} respectively, during July.

7.2.5 Temporal and Geographic Changes in Source Strength

The final set of simulations incorporating a non-uniform source of tropospheric gravity waves comprises a source varying with both latitude and time of year. The assumption made is that a tropospheric source of broad spectrum gravity waves is linked to the relative position of the sun overhead - a higher elevation corresponding to greater solar forcing of convectively generated gravity waves.

The exact form of this source differs from the *geographically* varying only source in that it is not a straight trigonometric relationship. A time- varying Gaussian-like function is used.

$$\sigma_h^2 = \sigma_0^2 \exp \frac{(\phi - \bar{\phi})^2}{2\gamma^2} + 0.75 \tag{7.3}$$

The source is a function of latitude (ϕ) and time (t) whose peak *moves* between the tropics of Cancer and Capricorn according to $\bar{\phi} = 23.5° \sin(\omega t - \Phi)$. Where ω is the angular frequency of one solar cycle and Φ is time of the northern spring equinox expressed as a phase within the year. σ_0^2 is a variance like term associated with the strength of the tropospheric source of gravity waves. The geographic spread of this Gauss-like function was controlled by the parameter γ, whose value was chosen to give the spread in σ_h^2 as seen by figure 7.25.

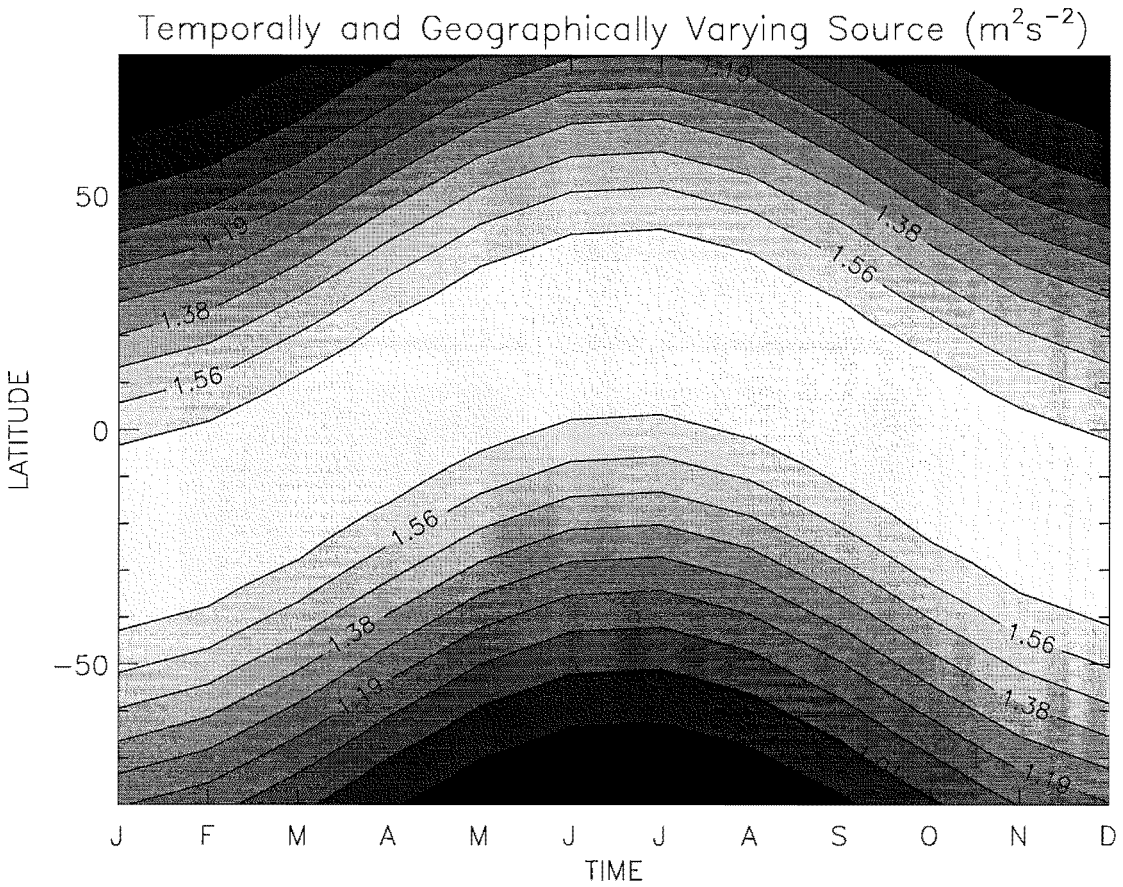

Figure 7.25: Global values of σ_h at 16 km for the simulation utilising both a geographically and temporally varying source of gravity waves of form given by equation 7.3.

Figures 7.26 and 7.27 compare output from the temporarily varying source with that of the geographically varying one. The zonal wind fields look remarkably similar, with the later simulation having a slightly stronger jet core. The temperature fields are also in broad agreement except in the polar north where the latter simulation predicts a slightly cooler stratosphere. The residual mean circulation show similar agreement with the only notable exception being the averaged ascent over the northern pole. This feature is linked with both the number and duration of sudden warmings during the month. As the model has shown quite a sensitivity to even slight changes in gravity wave strength during winter, one would expect modelled temperatures throughout the middle atmosphere to be lower for comparative simulations running the time varying source, as its form was chosen to have a greater strength in the summer hemisphere. Both the broad spectrum and orographic drag for each simulation are similar, with the possible exception of stronger orographic drag in the latter simulation.

At first these results appear at odds with the those from previous simulations. The northern winter middle atmosphere has shown great sensitivity to any difference in gravity wave forcing. However, with the source varying in time, one is not seeing appreciable

change, during this month anyway. It is fortuitous that for this simulation the broad spectrum drag in the winter hemisphere is actually very similar in value to the geographically varying simulation, considering the different nature of the sources in the two simulations.

Again, discrepancies are found over the winter polar mesosphere in temperature. There is no alleviation of the cooler modelled temperatures there. Although for both simulations, the extratropical wind jets are more in line with observation.

During equinox the simulations continue to repeat each others main characteristics. The only perceptible differences here appear to be associated with greater broad spectrum drag inducing greater downwelling in the polar south. This is connected with higher temperatures above the southern polar stratopause. These differences are due to the tropospheric source of parameterised gravity waves which are being forced in the two runs. During these times and latitudes the tropospheric source is stronger for the temporarily varying case, thus the differences in the fields. This is another surprising result considering the relative difference in strengths between the simulations at these times. During these times the two simulations have source strengths of approximately $\sigma_h = 0.5$ m^{2}s^{-2} and $\sigma_h = 0.75$ m^{2}s^{-2} (geographic only/temporal varying, respectively) at these latitudes. This is a further indication of the sensitivity of the model to changes in source strength especially at these latitudes.

In the main, the temperature profiles seen are in accord with both the CIRA86 and UKMO datasets, about most of the stratopause especially. The exception to this is the southern stratopause, where minimal gravity wave drag occurring at these times do not allow for great adiabatic heating and so produces a cooler polar stratopause as a result.

Finally during July small differences are found in temperature above and below the southern polar stratopause. These are small (below 10K) and are linked, again to circulation changes brought about by increased broad spectrum drag in the mesosphere. It should be noted that the simulations are run with a model lid at 96 km. Drag here (not seen in figures) will have a direct bearing on circulation below, via downward control. Any increase in strength of a (isotropic) source of gravity waves launch at the tropopause will result in additional drag in the mesosphere and resultant circulation changes. It is interesting to note very little change in the atmospheric state during the northern summer. The trend in a cold extratropical bias persists and appears endemic to all of these simulations.

7.3 Discussion

In this chapter an attempt was made exploring the response of an atmospheric model to broad changes in the makeup of a parameterised tropospheric gravity wave source. The study was conducted using one particular parameterisation so as to remove any possible

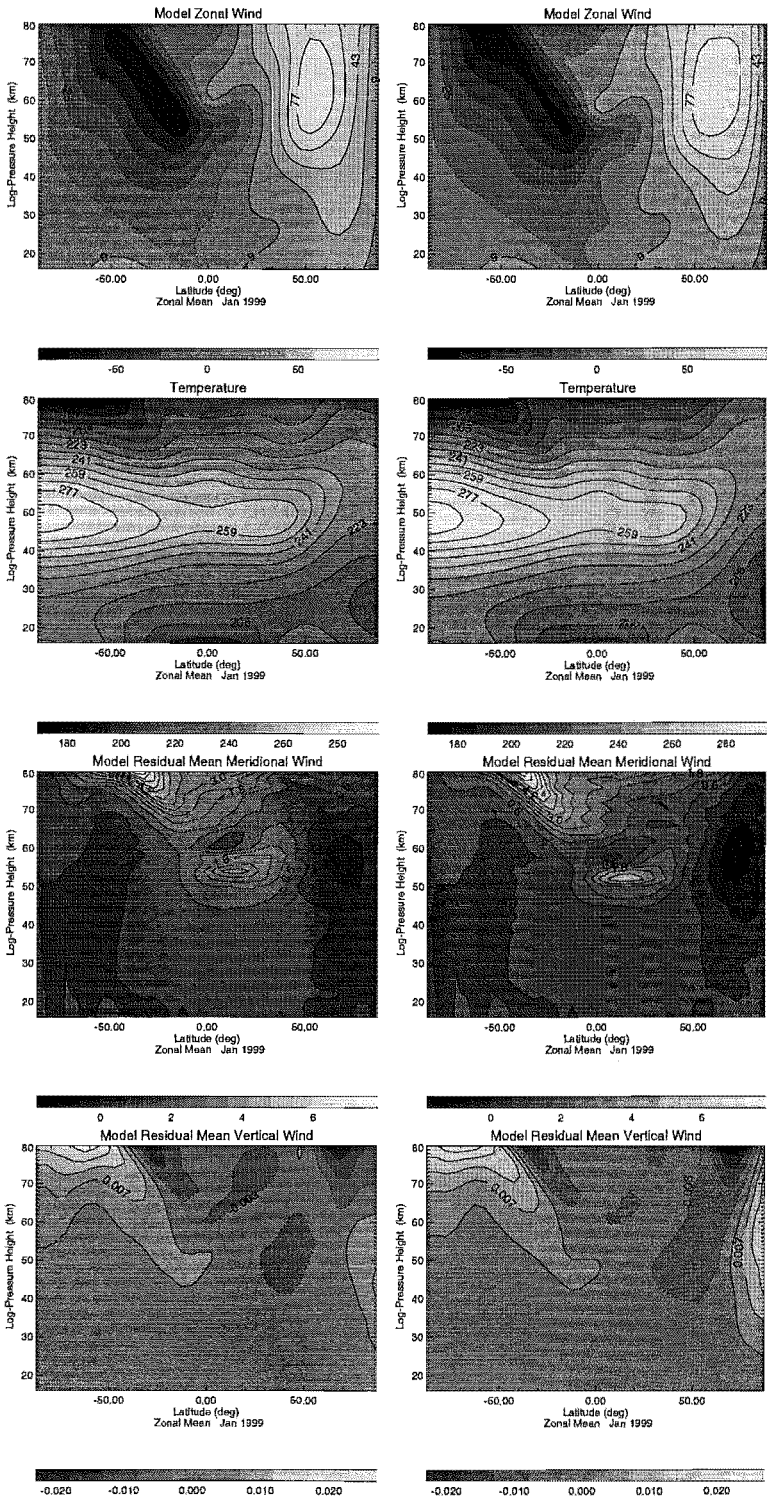

Figure 7.26: Zonal mean averages of zonal wind (m/s), temperature (K), meridional and vertical wind (m/s) from the simulations using a source varying in latitude/time and latitude, respectively. Peak strengths are $\sigma_h = 1.75$ m^2 s^{-2} and $\sigma_h = 1.5$ m^2 s^{-2}, respectively, during January.

ambiguity as to the nature of differences seen. The study also assumed isotropy in the source. That is no preferred direction for the initial spectrum of waves. This was clearly a crude assumption to make, but one which is imposed considering our present knowledge

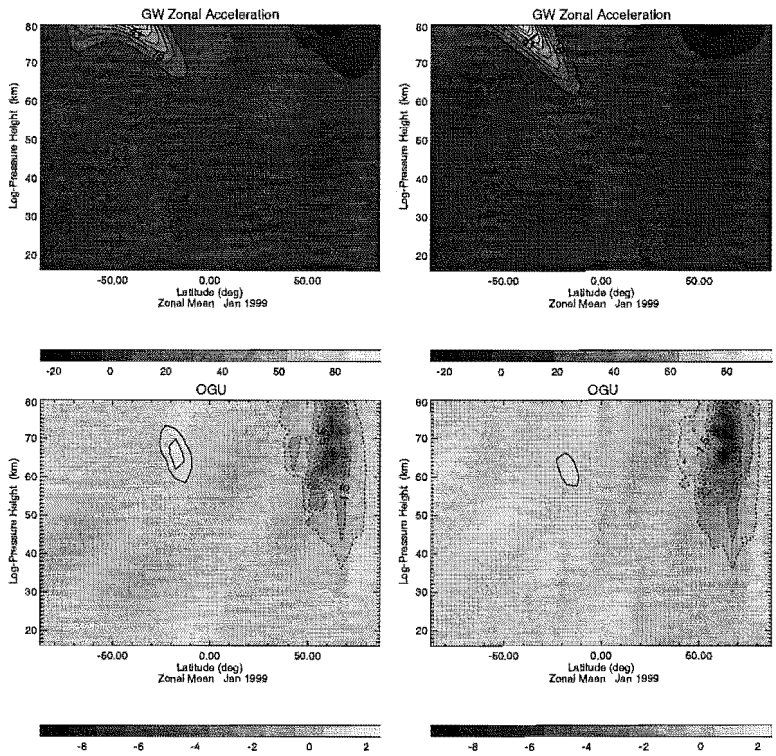

Figure 7.27: Zonal mean averages of gravity wave drag (m/s/day) (from a broad spectrum and orographic source) from the simulation using a source varying in latitude/time and latitude, respectively. Peak strengths are $\sigma_h = 1.75$ m^2 s^{-2} and $\sigma_h = 1.5$ m^2 s^{-2}, respectively, during January.

of such a global source.

The first section discussed the broad modelled response to a global increase in strength of a tropospheric gravity wave source. The general trend throughout the year was for a reduction in the height of breaking of waves in the mesosphere as the strength was increased. This is expected in theory to occur, as a stronger source will be more susceptible to non-linear effects from the spectral wave induced wind at lower altitudes. Because of the isotropy condition imposed and the level of the launch height (tropopause), intervening stratospheric winds between the launch height and the mesosphere filter parts of the spectra, leaving a net flux of waves opposing the direction of the winds below. Furthermore, the spectrum of waves was launched about the wind - that is their ground based phase velocities were distributed about the mean wind. This would have a significant effect. Thus, the net result was for a drag to tend to close off the stratospheric jets. Furthermore, recent studies (*Alexander and Rosenlof* (1996)) have suggested that a local forcing is required on the summer stratospheric wind jet to explain local circulation there. The spectrum as it has been setup will do just that, as it is composed entirely of extrowaves. When non-linear effects are small compared to the background wind effect - below the stratopause, the forcing is almost entirely accelerative. However, the merits or otherwise of such a forcing in the winter hemisphere can only be guessed. It could be

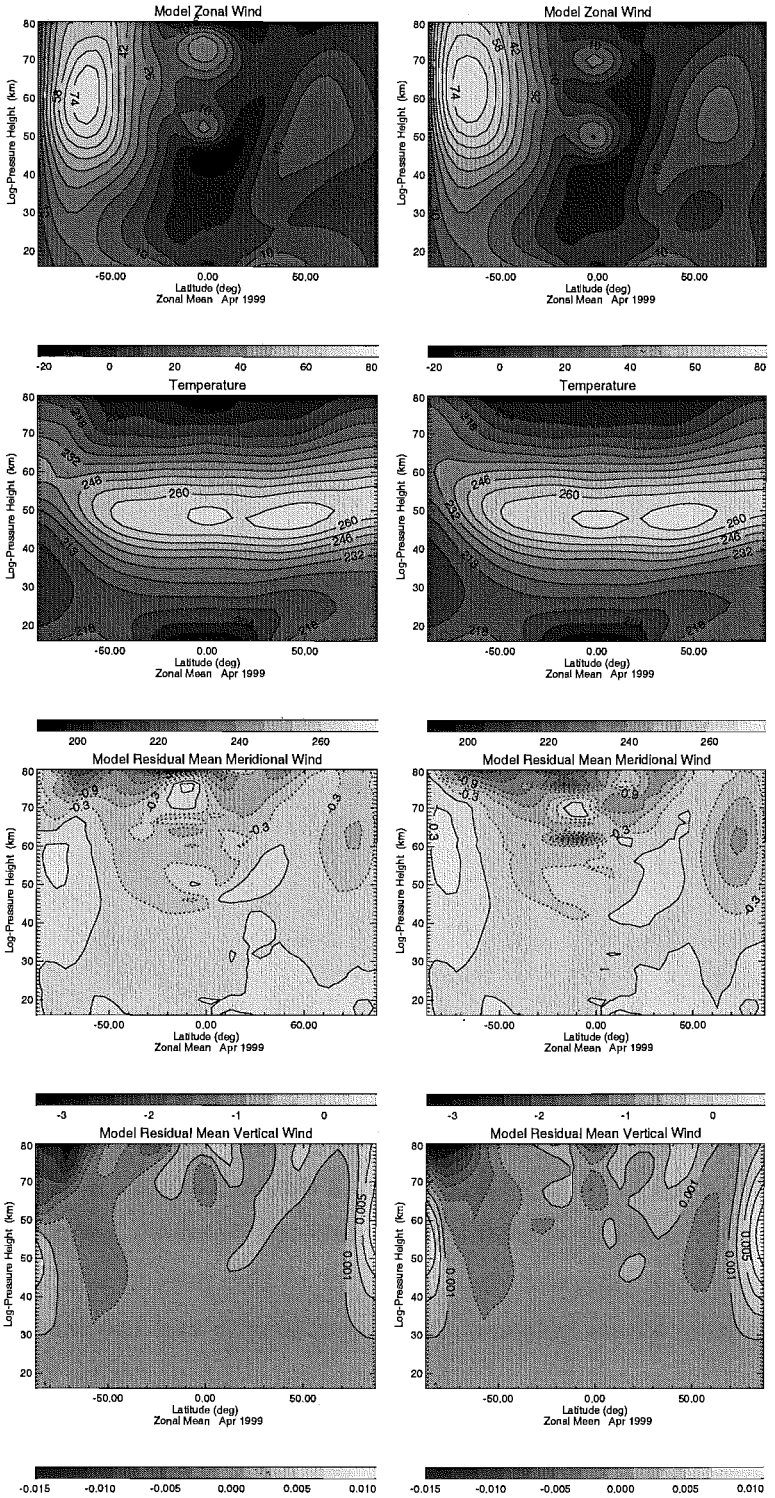

Figure 7.28: Zonal mean averages of zonal wind (m/s), temperature (K), meridional and vertical wind (m/s) from the simulation using a source varying in latitude/time and latitude, respectively. Peak strengths are $\sigma_h = 1.75$ m^2 s^{-2} and $\sigma_h = 1.5$ m^2 s^{-2}, respectively, during April.

that the lower than observed stratospheric temperatures could have been influenced by the circulation changes set up from such a forcing. Indeed, a positive forcing on the polar night jet would increase the magnitude of the poleward temperature gradient, causing

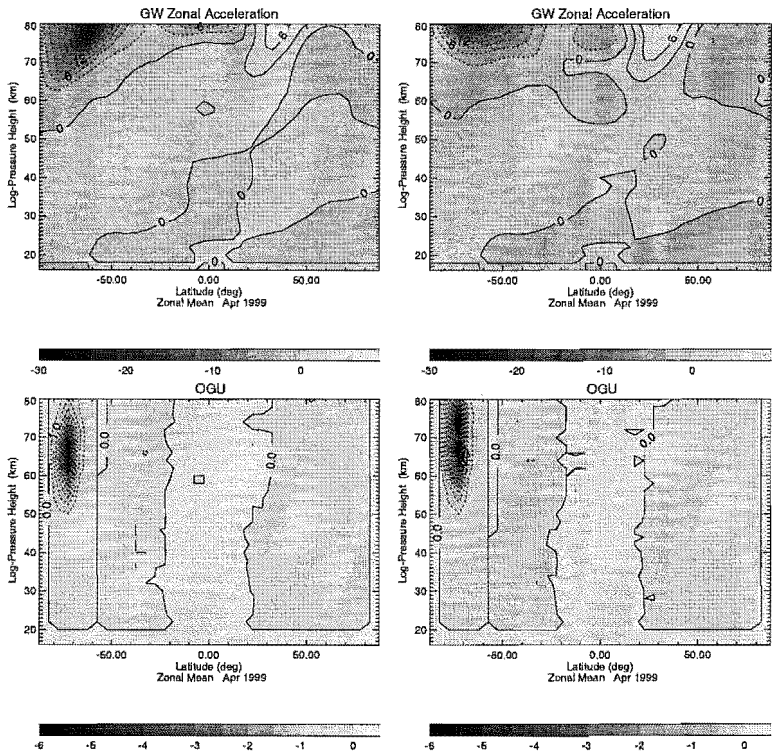

Figure 7.29: Zonal mean averages of gravity wave drag (m/s/day) (from a broad spectrum and orographic source) from the simulation using a source varying in latitude/time and latitude, respectively. Peak strengths are $\sigma_h = 1.75$ m^2 s^{-2} and $\sigma_h = 1.5$ m^2 s^{-2}, respectively, during April.

lower temperatures. This would be due to the Coriolis force setting up a southward circulation causing ascent and thus cooling over the northern pole. Exactly how significant this would be compared with the opposite driving higher up, is not known.

One of the effects of using a weak global source of tropospheric gravity waves (or indeed none at all), is an unusually cool winter middle atmosphere. The trend seen in these simulations was for this to be improved. However, in doing this the temperature of the polar stratopause did rise above observational values. It was also seen that the summer lower stratosphere was cooler than observed throughout all of the runs - and was thus apparently insensitive to a changing source. The summer mesosphere although cooled throughout the three simulations did not cool as much as the winter mesosphere warmed.

A further difference was the relative number and strength of sudden warmings throughout the month of January. It was seen that the timing of these changed slightly between simulations and indeed that the timing of the final warming, at least between the two lower sourced runs, occurred at earlier times. The changes in nature of sudden warmings can be explained due to a weakening of the meridional temperature gradient northward of 60°N at a height of 30 km - a weaker wind gradient does not favour the occurrence of these events (*Butchart et al.*, 1982). The delay in onset of the final warming could

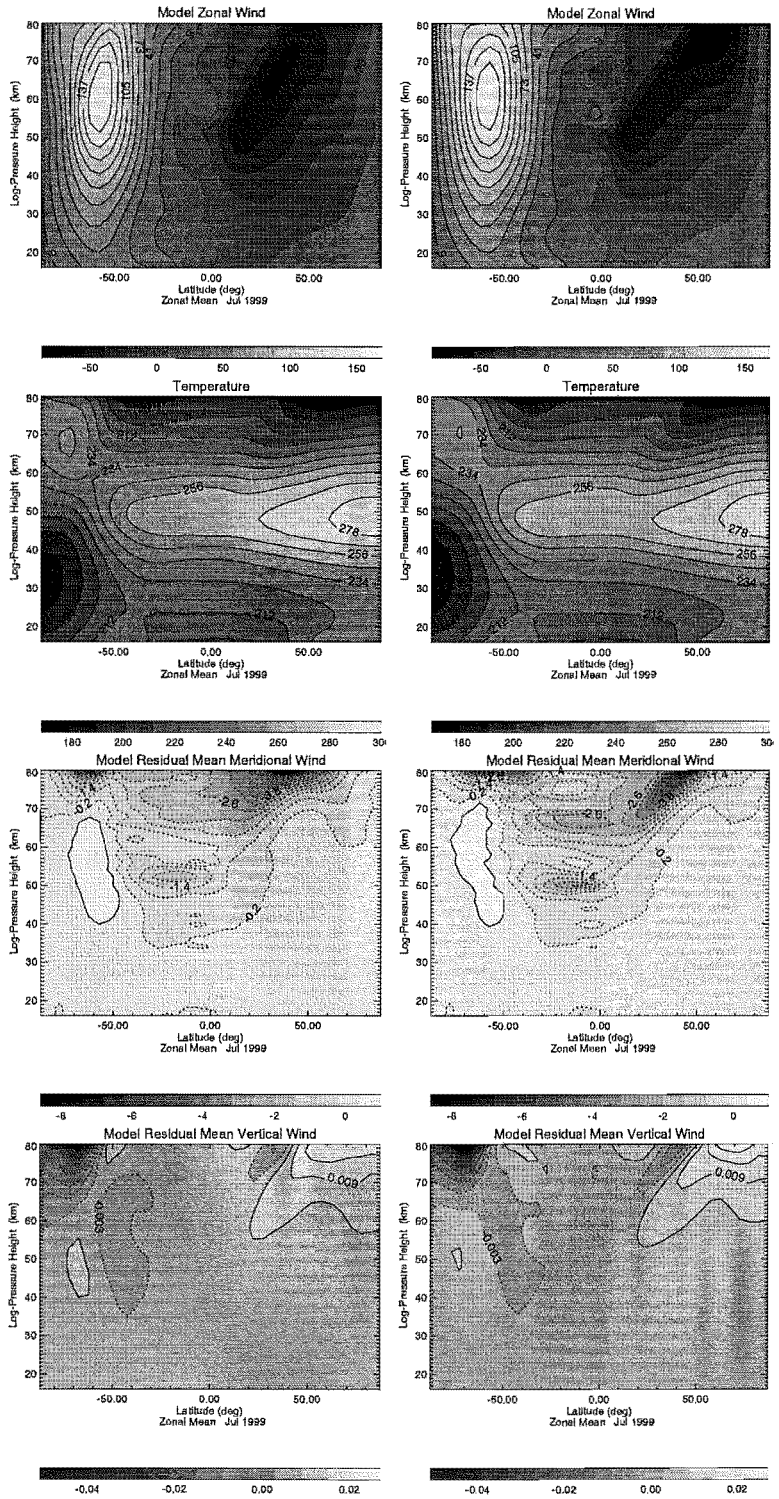

Figure 7.30: Zonal mean averages of zonal wind (m/s), temperature (K), meridional and vertical wind (m/s) from the simulation using a source varying in latitude/time and latitude, respectively. Peak strengths are $\sigma_h = 1.75$ m^2 s^{-2} and $\sigma_h = 1.5$ m^2 s^{-2}, respectively, during July.

possibly be explained by the fact that the meridional temperature gradient was weakened between the two low strength simulations. The switch from zonal westerlies to easterlies is sensitive to this and is simply related to the reversal of this gradient. The change in

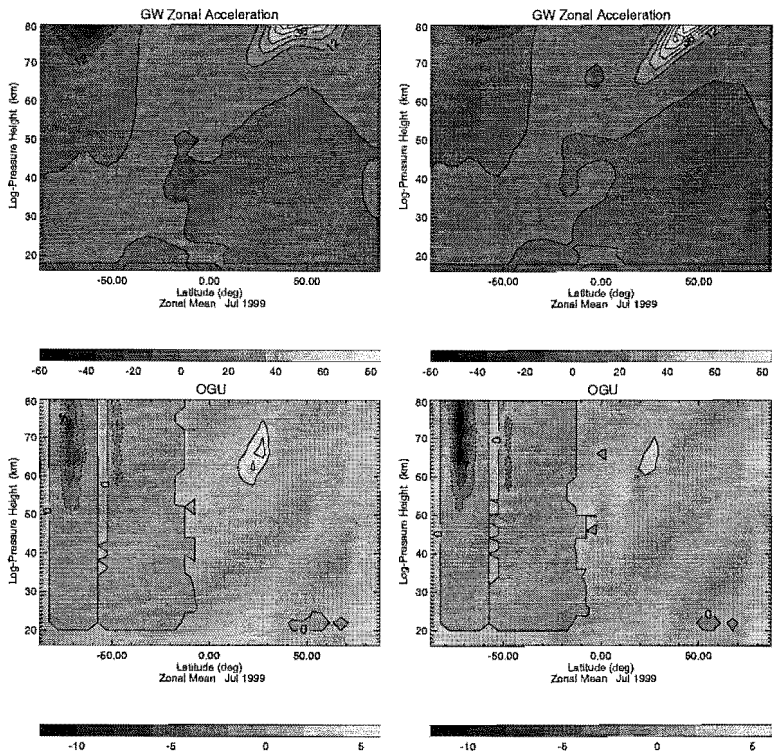

Figure 7.31: Zonal mean averages of gravity wave drag (m/s/day) (from a broad spectrum and orographic source) from the simulation using a source varying in latitude/time and latitude, respectively. Peak strengths are $\sigma_h = 1.75$ m^2 s^{-2} and $\sigma_h = 1.5$ m^2 s^{-2}, respectively, during July.

the winter jet also changed the nature of propagation of model resolved planetary waves (lower breaking level). The effects from these are the major influence on the evolution of sudden warmings. This and the profoundly different atmospheric state may go to explain why the final warmings occurred later in the strongly sourced run.

The change in the atmospheric state due to the mutual interaction between the two sources of waves appeared minor and lay within the natural variability of the model. During winter and northern spring the atmospheric variability is particularly great due to sudden warmings and the final warming. To a first approximation, one would not expect to conclude any significant statistical difference between the interacting and non-interacting cases. So although observationally these processes may not be seen above the general atmospheric *noise*, their effect could still be appreciable. It was noted that there may have been statistically significant changes seen in the southern winter lower stratospheric temperatures. This is further indication of the sensitivity of this part of the atmosphere to dynamical forcing during these times.

Section 7.2.3, differed from the other sections in that its aim was not to examine broad changes in the modelled atmospheric state and link these to a particular source. As already mentioned, such a study has been already undertaken, investigating a launch height for a global source of these waves *below* the tropopause (*Manzini and McFarlane*

(1998)). Instead the aim was to follow up the findings from section 6 by including a tropospherically filtered source as input into the SMM and examining the simulation for the predicted forcing (*Osprey and Lawrence*, 2001). It was seen that a planetary wave signature was indeed forced in the model. This was linked to wave one gravity wave drag in the model and appeared to be linked with both the Tibetan high and Asian monsoon. Such a planetary wave signal was investigated by *Wang et al.* (2000) during the southern summer. However, it would also appear that similar signals have been seen in the northern hemisphere as well during summer (*Wang*, pers. com.).

A summary listing the chief modelled climatic sensitivities after changing a tropospheric source of gravity waves as previously discussed, and a comparison with observations can be seen in table 7.3. For completeness, to compare with differences seen after changing the launch height of the source spectrum, the reader is instructed to consult *Manzini and McFarlane* (1998).

Future work should include models run including more accurate, observationally based tropospheric sources. The beginnings of such have already begun in earnest (*Lawrence*, pers. com.) and should shed light on what significance a realistic source has on climate. With these, different parameterisations can be better tested against each other and observation and should indicate what physics is important and so should be included. Ideally, one would prefer such a source to be determined from the model itself. For instance, the amount of convection, parameterised or otherwise may go to determine the amount of gravity wave momentum flux leaving the troposphere (*Webster*, pers. com.). This is currently done using orographic sources where topographic datasets are required. This has the advantage of coupling the source to the model and more accurately (possibly) representing the impact of other processes on a modelled climate. The shortcomings of such an approach would include introducing greater scope for error as many such processes are currently themselves parameterised in models. It is these processes which most adversely affect a models performance. Finally, there is always the prospect of greater computer power. This has the advantage of better resolving the physics of these small scale waves. However, one still needs an accurate representation of a global source as it has been seen that some parts of the atmosphere are especially sensitive to gravity wave forcing.

Source Changes	Sensitivities/Comparison with Observations
As global mean source increases:	• Polar-night jet weakens and reversal occurs lower down • Polar winter stratosphere and mesosphere warms • Summer stratosphere remains cool (insensitive to changing source) • Timing of final warmings are earlier (c.f. low-mid source) and later (c.f. low-high source), respectively • An unrealistically weak polar night jet is seen for high source, but: • Realistic Quasi Biennial Oscillation
After inclusion of an interacting orographic source:	• Polar night wind jet shifts poleward • Winter polar stratopause ascends (away from observations) in northern hemisphere while polar stratosphere warms in southern hemisphere • No QBO is reproduced • Cold winter bias remains in polar mesosphere; improves in northern hemisphere but worsens in southern hemisphere
As mean source decreases toward the poles:	• Cold winter bias remains in polar mesosphere - entire middle atmosphere cools • Polar night jet strengthens and trends above observations • No QBO is reproduced
As a geographically varying source changes in time:	• Polar middle atmosphere winter temperature warms with a trend toward observations, although: • Cold winter bias persists in polar mesosphere • No QBO is reproduced

Table 7.1: Table of sensitivities seen between simulations and comparisons with observations. The low, mid and high sources refer to the simulations utilising a gravity wave source of total wind variance of 1 $m^2 s^{-2}$, 2 $m^2 s^{-2}$ and 4 $m^2 s^{-2}$ respectively.

Chapter 8

Comparison of Two Parameterisations in the SMM

In section 5.2 a comparison of three gravity wave parameterisations was done examining their respective interaction with a prescribed atmospheric state. That study was termed *off-line* in that the relevant tendencies produced by the models (eg: zonal wind tendency) were not allowed to feed back into a model and adjust it accordingly. This is a significant factor and is one which must be addressed to gain a more complete understanding of the relative performance of each of the schemes.

As for the off line tests, a common source was employed for each of the parameterisations. This was done in a completely analogous manner as previously. That is, a particular spectrum was assumed ranging in vertical wavenumber from a low number cut-off to an upper bound determined by the Hines parameter, m_{ji} (refer equation 4.4). Then a strength parameter was assigned, which corresponded to the total wave wind variance of the DSP. From this, a spectral horizontal momentum flux could be calculated. Other common parameters (e.g. the characteristic horizontal wavelength) had values as stated in previous chapters.

Originally a value of 1.0 $m^2 s^{-2}$ was employed for the total wave wind variance. However, it soon became apparent that the resultant drag produced for the MK95 simulation was occurring too high as to make the integrations unstable. That is, not enough drag was occurring within the model and so the winds were becoming increasingly strong so as to break the CFL criterion. The remedy was to increase the source strength (4.0 $m^2 s^{-2}$) so that the breaking could occur lower down as was seen with the DSP simulations in Chapter 7. This had the desired effect and stable runs were completed for 6 years of model time. As predicted from the single column comparisons, the drag from the USSP was very slight using these values for the source and no stable integrations could be sustained. A stable integration could possibly be performed if the gravity wave source strength was increased sufficiently. This was not attempted, however, as the required strengths would necessarily be one to two orders of magnitude different compared to the other two schemes (as measured by total momentum flux). This would be difficult to reconcile with range in source strengths thought to exist - being between $\sim$1-4 $m^2 s^{-2}$ for a total wind variance (*Allen and Vincent*, 1995).

Figure 8.1 shows the climatological output from the SMM for both the MK95 and DSP

parameterisations for the month of January. From immediate inspection it is apparent that both simulations are considerably different. From the broad spectrum drag profiles it is seen that considerable drag occurs down as low as the stratopause for the DSP run, however, this is not seen in the MK95 run. This has considerable impact on all the other fields. A combination of direct drag on the southern summer jet from eastward directed drag and temperature changes reducing the poleward temperature gradient results in a significant reduction in the the wind jet. This is not seen to the same extent for the MK95 simulation. The northern circulation is dominated by the dynamical heating of the polar middle atmosphere. Even though considerable warming is seen for the DSP simulation, the strength of the polar night jet is still maintained by the poleward gradient in temperature.

A similarity is seen when comparing the MK95 simulation with the DSP simulation running with a globally homogeneous wave wind variance of 1.0 $m^2 s^{-2}$, in section 7.2.1. The respective January output fields are very similar with the only notable difference being the northern stratopause having a local maximum for the MK95 simulation. Such a feature is seen in the UKMO assimilated data and was not seen in any of the previous DSP simulations. Also, the residual meridional circulation is slightly stronger for the MK95 case.

During April the simulations differences are dominated by a residual meridional circulation which resembles for the MK95 simulation, that displayed by the DSP with a quarter of the source strength. The MK95 simulation produces a residual circulation closer to that shown for the UKMO reference data. The southern stratopause is cooler for the MK95 run than for the similarly strengthed DSP run, but warmer than that using the lower source strength. This is consistent with the vertical circulation - stronger/deeper descent, greater warming. The zonal winds have strengths directly related to these other fields, with that for the MK95 run intermediate in strength to the mentioned DSP simulations. The pattern of broad spectrum drag for the MK95 run is similar in magnitude and pattern to the two weaker DSP simulations, presumably in accordance with the simulated winds below.

Finally for July, the southern stratopause is markedly warmer in the high sourced DSP run. It is also lower in altitude, more in agreement to UKMO data for the same period. Although, it should be stated that none of the simulations seen thus far have been able to reproduce a southern winter stratopause quite like that for the UKMO dataset. The chief difference being the marked increase in height of the polar region compared with higher latitudes seen for this study. The likely cause for this is the relative make up of the spectrum - an inappropriate assumption of spectral isotropy at the tropopause. Again, linked to temperature differences, the polar night jet is considerably stronger for the MK95 run.

To help identify the possible factors giving rise to the differences seen between the two simulations, a further set of simulations were conducted dumping any remaining wave-momentum left, at the top of the model. The reasoning here has its origins in equation 2.19. Its predicted wave-driven circulation is dependant on all waves going on to break higher in the atmosphere. Up until now, each simulation has been run without this upper boundary condition. The results of this further set of runs are qualitatively very similar to the ones shown. This can be explained after looking at the results from section 5.2. It was seen there that most spectral momentum flux is deposited in the troposphere and stratosphere. There is very little remaining in the mesosphere, where the top of the model is located. Although the wave induced accelerations seen at these heights are larger than those seen below, this is solely due to the rarefied atmosphere (the wave acceleration is inversely proportional to density). It is the magnitude of the net momentum flux (and latitudinal gradient) which go to determine any change in circulation lower down.

8.1 Discussion

The current state in gravity wave parameterisation is concerned with both physics and source issues. In this study, the model performance of three separate schemes have been explored neglecting consideration of any source issues. The modelled differences here have been solely due to the encoded dynamics of the theory.

In section 5.2 it was asserted that the differences between two of the schemes (the DSP and MK95) were systematic yet small. The third behaved in a completely different manner and was attributed to ideas laid out in the theory, ideas which were approached in an entirely different way to the other two schemes. However, it has been seen that, differences no matter how small can be accentuated in a non-linear atmospheric model. These differences could be put down to the choice of tunable parameters in the models. However, the MK95 parameterisation has only the one tunable parameter, the characteristic horizontal wavelength and so such arguments can only be pursued so far[1]. Most likely it is the slightly stronger modelled interaction between the waves, as described in the DSP, which induce changes in the model which produce a positive feedback - waves break lower down resulting in stronger wind shear, which in turn result in the waves breaking lower down. The differences seen here are probably inherent and cannot be put down to tuning within a given scheme. It is these which will ultimately determine the relative success of any scheme as soon as more complete observations are made so as to refine our ideas of the global makeup of a tropospheric gravity wave source.

The behaviour of the MK95 parameterisation was likened to that from lower strength DSP ones. It was necessary to increase the strength of its source so as to produce enough

[1]however, the DSP has many such tunable parameters.

drag within the model for stability. This behaviour was not seen to the same extent in the offline testing - it was purely an effect of inclusion in the model. The degree of similarity to these other runs was significant. The nature of the forcing and the resultant atmospheric state was uncannily similar. However, it is not justifiable to just introduce another adjustable parameter so as to smooth over these differences. These are fundamental and direct attention as to what needs to be examined within the theory of each to understand why they occur.

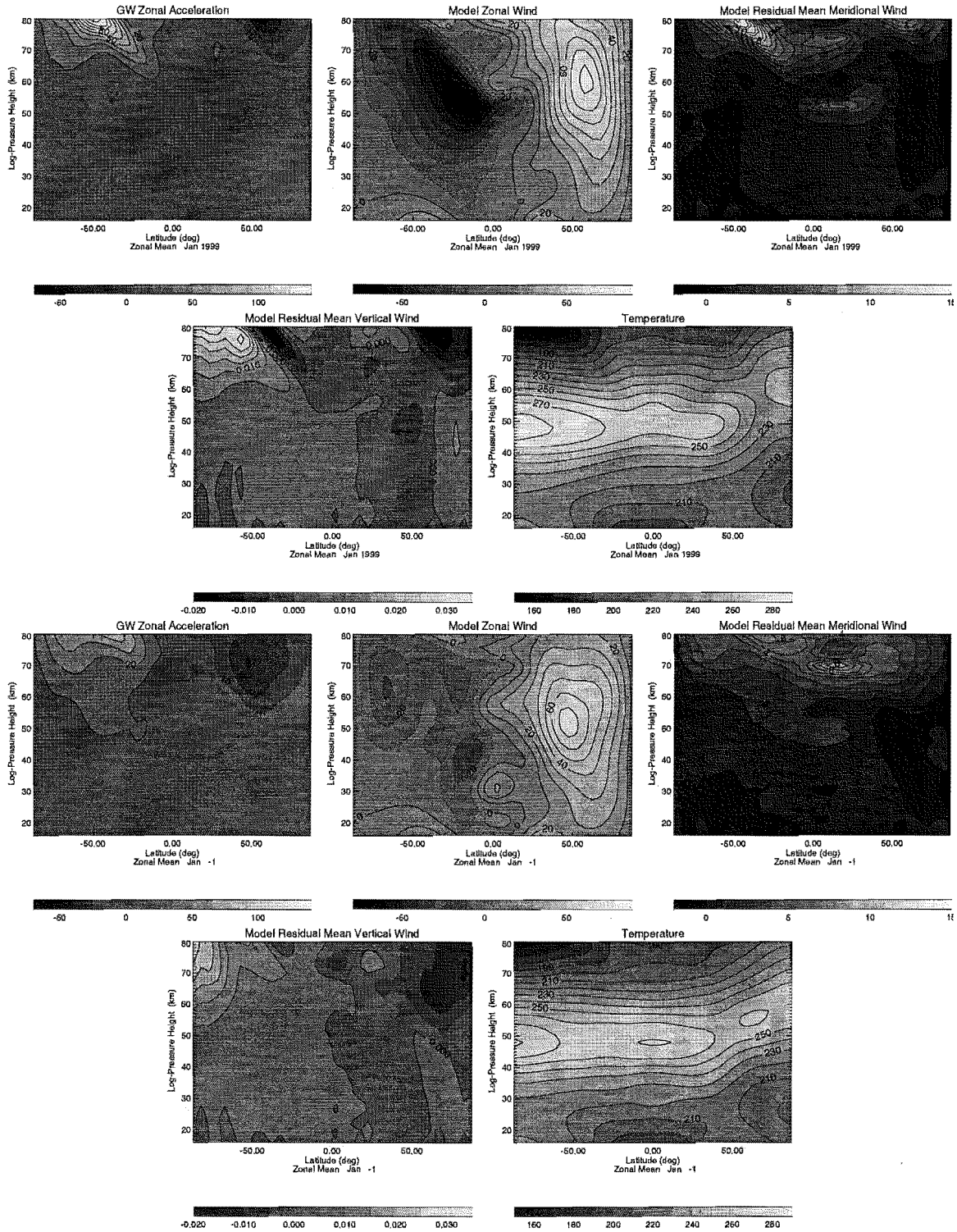

Figure 8.1: Climatological vertical output from the SMM of: zonal broad spectrum drag (m/s/day), zonal, meridional and vertical wind (m/s) and temperature (K), from the MK95 and DSP schemes, during January. The total wind variance of the source of waves was σ_t =4.0 $m^2\,s^{-2}$.

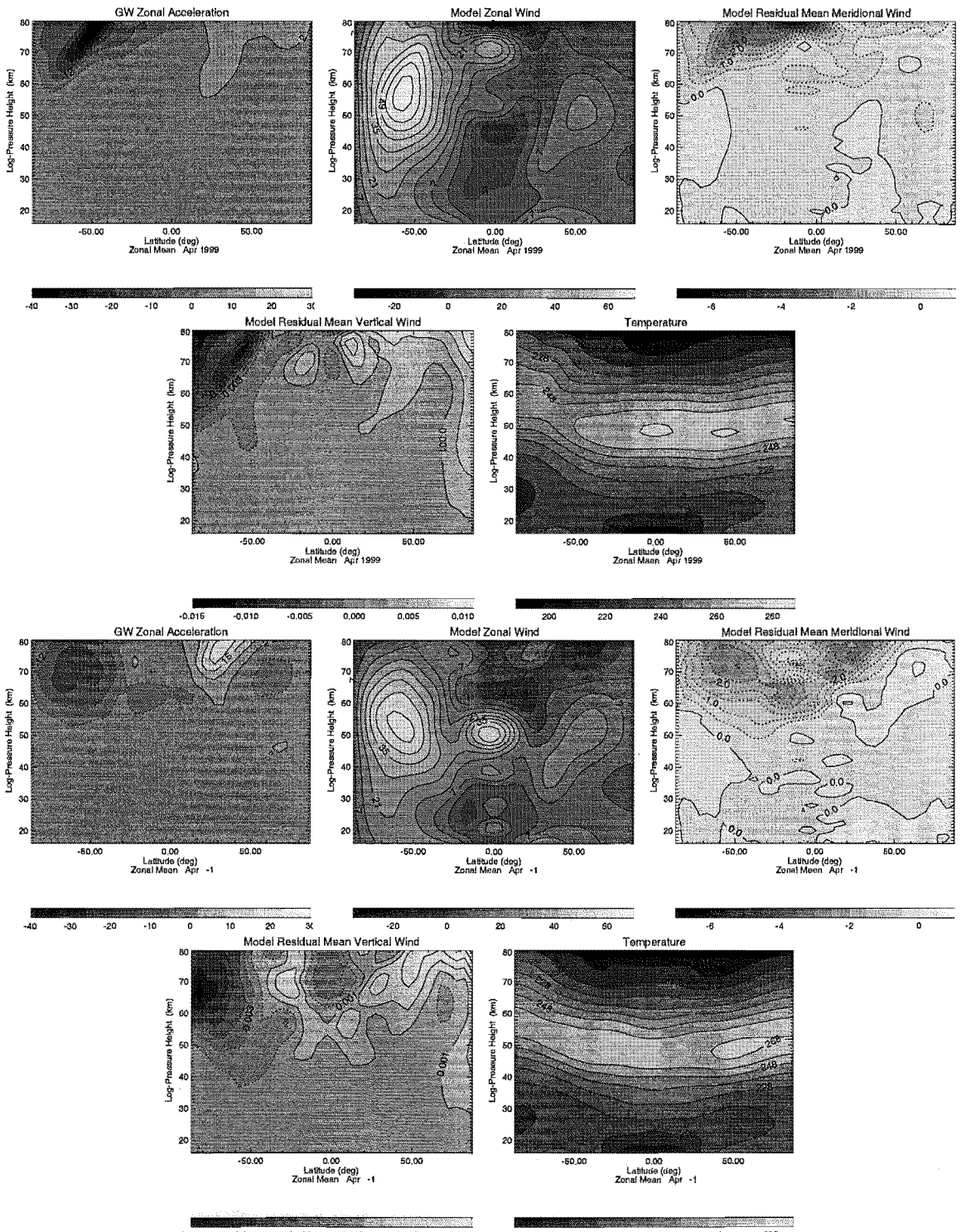

Figure 8.2: Climatological vertical output from the SMM of: zonal broad spectrum drag (m/s/day), zonal, meridional and vertical wind (m/s) and temperature (K), from the MK95 and DSP schemes, during April. The total wind variance of the source of waves was σ_t =4.0 $m^2\,s^{-2}$.

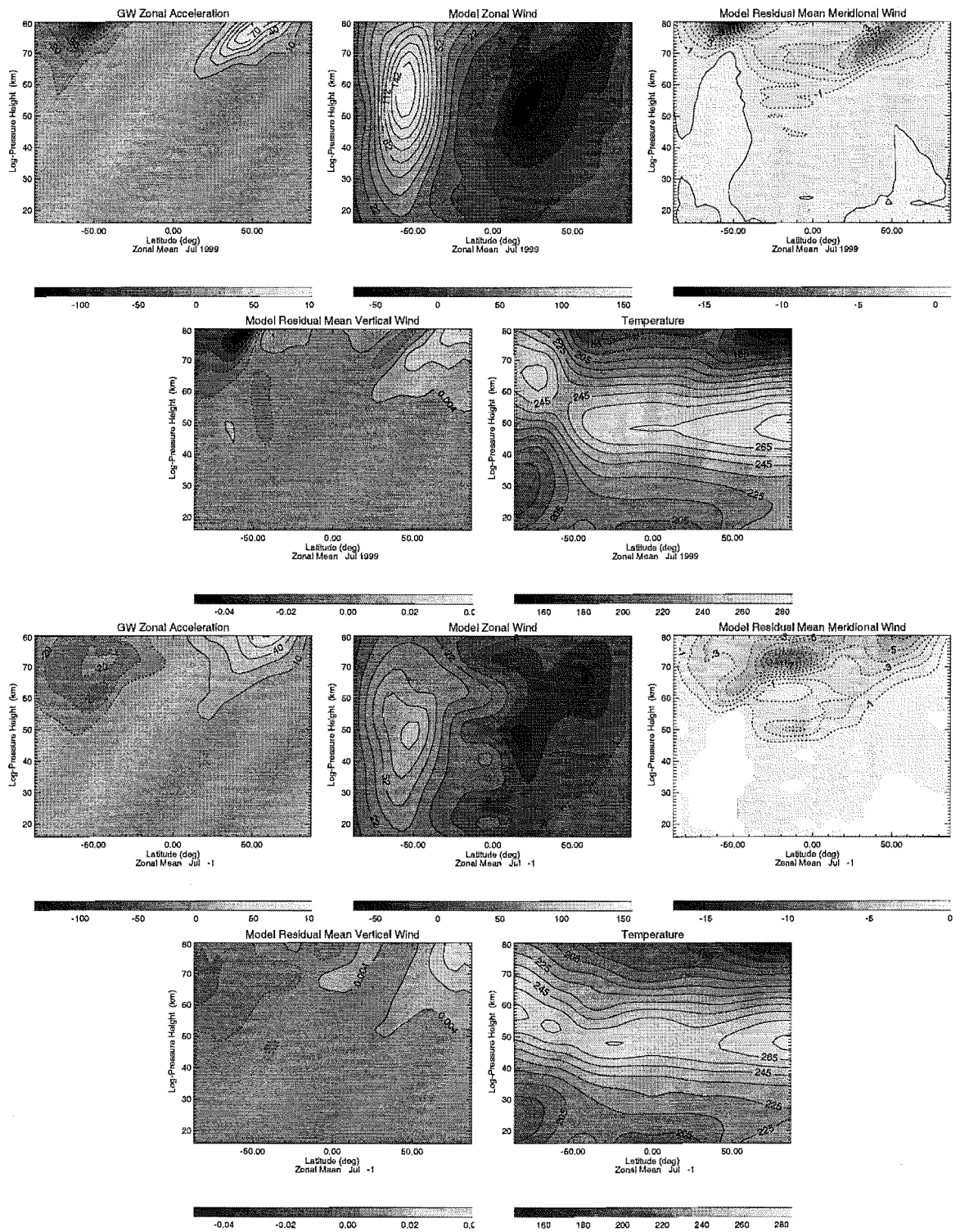

Figure 8.3: Climatological vertical output from the SMM of: zonal broad spectrum drag (m/s/day), zonal, meridional and vertical wind (m/s) and temperature (K), from the MK95 and DSP schemes, during July. The total wind variance of the source of waves was σ_t =4.0 $m^2\,s^{-2}$.

Chapter 9

Summary and Discussion

Before the availability of fast computers and sophisticated parameterisation schemes, it was widely appreciated that there was a real need for some kind of representation of the effects of small-scale gravity waves in atmospheric models. With the advent of these new *tools*, it has become apparent that these ideas may be somewhat naive - other issues (e.g. a realistic tropospheric source) are just as important.

A second issue which is proving less tractable compared to that of parameterisation is the one of representing accurately all possible tropospheric sources of gravity waves. It has been known for some time that these waves can be generated in a number of different ways, but quantifying the relative contribution from each of these is somewhat problematic. Furthermore, being able to obtain information about a particular source event at a given time is one thing. Doing so over a global scale on seasonal timescales is quite another and it is this sort of information which is required to improve model simulations of the middle atmosphere as well as to verify the accuracy of modelled source regions.

But is there a need to have an accurate representation of a global source? Or put another way, how sensitive (or otherwise) is a modelled climate to arbitrary changes in a prescribed tropospheric gravity wave source? That is the main issue that has been addressed in this thesis. A second issue - the choice of parameterisation, has also been explored.

The latter issue was first addressed in a couple of model environments removed from any direct interaction with a wholly dynamic model. The first of which (chapter 5) used data from a combination of different datasets to construct *representative* vertical profiles of the mean atmospheric state for a number of different locations during different times. From this, a standard source was given to three gravity wave schemes and their relative response noted (section 5.2). It was found that for two of the schemes, similar responses were achieved under conditions of significant background wind shear. This should come as no surprise as all three schemes incorporate the effects from the wind in an entirely similar fashion. That is assuming from linearised theory (appendix B), various parts of the gravity wave spectral source undergo critical level processes (break down), whenever the difference between their phase-velocity and the background wind approaches zero

(equation B.12). Significant differences only became apparent within regions of little wind shear. Such behaviour is predictable because both the schemes in question (the DSP and MK95) use the *wind* as set up from waves in the spectrum to facilitate dissipation of parts of the spectrum in a similar fashion to that achieved by the background wind. When the spectrum of waves is travelling through regions of little wind shear and a considerable part of the slower, high vertical wavenumber spectral parts are left, the wind effects from the spectrum become noticeable - that is differences are seen between these two schemes. This response is also influenced by the momentum density of waves in the spectrum - which is weighted toward these slower waves.

The third scheme (the USSP), behaved in an entirely different manner to the other two parameterisations. Only in conditions of alternating wind shear, as seen in the tropics, is an order of magnitude correspondence seen with the others. The trend was for a steady decrease in spectral momentum flux with height. This meant that there was less available momentum left to force the background flow higher up compared with the other two. It would appear that this difference has its origins in the way the USSP models dissipation. As seen in appendix C, under idealised conditions of no wind and constant temperature, the amount of wave forcing by the USSP is controlled by atmospheric density and *spectral shape*. As compared to the DSP scheme under similar conditions, it was seen that the USSP gave greater dissipation at all levels. Spectral shape also controls the amount of dissipation for the other schemes but does not play as dynamic a role as in the USSP.

Section 5.1 examined the effect of inclusion of the mutual interaction between orographic and broad spectrum waves. The affect on the the broad spectrum by the orographic source appeared confined to the region of breaking of the latter - though the size of the effect was appreciable (a factor of three). However, it was noted that such a response would be highly dependent on the relative makeup of the spectrum of waves at the height in question. The Doppler shifting of the background wind on both sets of waves appeared to minimise the size of the effect seen, as shown by the height of breaking of the orowave lowering under conditions of no wind shear. As such, it was stated that such processes would be most noticeable during times of equinox - when wind shear is least.

Chapter 6 differed somewhat from others in the thesis. The objective was to look at how large scale stationary planetary waves, as represented in the UKMO assimilated dataset, influenced the vertical propagation of an arbitrary source of tropospheric gravity waves (*Osprey and Lawrence* (2001)). The exercise was purely exploratory in nature and the end result surprising to some respects. Although *Holton* (1984) carried out a similar study, no attempt was made to impose longitudinal structure on the tropospheric gravity wave source. It was found that the pattern of gravity waves reaching a particular height is directly influenced by the pattern of the underlying winds. However, once formed, how long do those patterns forced in the propagating source of gravity waves persist? It was

found that during the northern summer, a large scale planetary-like signal appeared in the vertically propagating gravity wave source in the troposphere. Although attenuated somewhat, this signal survived to the stratopause. The origins of this signal appeared linked to comparatively low levels of static-stability associated with the Tibetan low which has an intimate connection with the forcing of the asian monsoon. This has implications for the vertical propagation of planetary waves which from basic theory (section 2.6) precludes the passage of these larger waves through regions of easterly flow - those which are found during summer in the middle atmosphere. The contention was then whether this planetary-like signal could then be forced on the background flow when the gravity waves would eventually break at an overlying height. This was the subject of section 7.2.3.

It was found that on inclusion of a source like that seen in chapter 6 into a mechanistic computer model (SMM), a planetary-like forcing was indeed seen above 80 km. Furthermore, this forcing appeared directly related to a wave one planetary wave feature in the zonal wind. That such a feature is forced during summer has significant implications for the dynamics of the mesosphere during these times. This ties in well with findings (*Wang*, pers. com.) which describe similar features in WINDII data during these times in the northern hemisphere.

Chapter 7 systematically set about determining the sensitivity, or otherwise, of the atmosphere to large changes in a prescribed tropospheric gravity wave source. The aim was not to try and *tune* a model response which was more in-line with observations, but to gauge whether the results obtained warrant the effort spent in developing such a source.

Section 7.2.1 examined the modelled response to global mean changes in strength of a tropospheric gravity wave source. The major areas of response were the southern winter polar middle atmosphere and the northern winter polar mesosphere (although there was some change seen in the stratosphere during this time). The runs incorporating a larger source looked more like observations, although temperature of the winter stratopause did rise above observations. These changes had considerable impact on the polar night jet in both hemispheres, where an unrealistic weakening occurred. One would expect from past studies (*Allen and Vincent* (1995)), that an unrealistic model response may be observed, as observational extratropical source strengths are lower than those used for two of the simulations. The summer mesosphere displayed a trend to cooler temperatures, but not to the same extent as the winter mesosphere warmed.

Linked with the profoundly altered polar night jet, is a change in the propagation of model resolved planetary waves. The level of gravity wave breaking was seen to occur lower down with increased source strength. The stratospheric momentum budget is influenced significantly by the passage of planetary wave one and two, so a descent in peak breaking should have a significant difference. Possibly linked with these altered propaga-

tion characteristics is the nature of stratospheric sudden warmings seen during January. A change in the onset time and strength of these between simulations was linked to changes in stratospheric winds near the pole. The onset of the (southern) final warming also appeared linked in some way to gravity wave source strength. For the two lower strength simulations, earlier times for final warmings occurred for a given year between simulations. However, for the stronger source case, this was reversed. This is not surprising considering the considerably changed fields seen between simulations.

For a geographically varying global gravity wave source, the modelled response was entirely consistent with the circulation changes resulting from either stronger gravity wave drag at a given height or drag peaking lower down. Such reasoning can be used to explain the changes seen between all simulations. For the two sources compared in this section, the geographically varying source had a weaker tropospheric source poleward of about 60° N/S and so slightly weaker residual circulations were observed.

For section 7.2.5 where a comparison was made between the geographically varying source and another similar, but one whose latitudinal peak varied within the tropics, depending on season, very little change was seen - geographically or seasonally. This can be explained due to a fortuitous choice in source strengths, where polar source strengths were comparable during winter. Having said this, there were slight differences in the summer consistent with the stronger source forced during those times.

The final simulation examined the modelled effect of using an interacting source of orographic and broad spectrum waves. The differences were minor and included a slight poleward shift of the polar night jet. This appeared to result in circulation changes, causing a rise in stratospheric temperature of the order of a few degrees Kelvin. One could justifiably assume that these processes would be obscured observationally by general variability in the atmosphere, although their effect is systematic and would appear to have a noticeable change in the southern winter stratosphere. However, it may be that other models which resolve a troposphere may share different results (*Chattopadhyay*, pers. com.). It is also worth mentioning that longer running simulations may produce smaller inter-annual variances in temperature and wind. Thus, small changes introduced using a coupled source may then become observed statistically.

Changes (in temperature) seen in the southern winter polar stratosphere were seen between most of the simulations carried out. This could have important implications for ozone related processes occurring during these times. Generally, a colder polar stratosphere facilitates the formation of icy particulates in this region. On these particulates, chemical reactions take place which play a role in ozone destruction. Any change in temperature in this region would change the concentration of these frozen aerosols and possibly influence the rate of ozone destruction in the proceeding spring. With extreme weather thought attributable to anthropogenic changes in CO_2 (global warming), any

increase in gravity wave activity during these times (caused by an increase in the number of storms) may have a hitherto unreported affect on ozone levels over the southern pole.

Much has been said about the extratropical response to gravity wave driving, but not much about tropical changes. There has been considerable research on the tropical response to gravity wave driving. *Lawrence* (2001) investigated (amongst other things) how the tropical circulation changes to different source strengths. It was concluded that a QBO-like response was achieved using a source comparable to that used for the $\sigma_h = 4.0\ \mathrm{m^2\,s^{-2}}$ simulations. Furthermore its frequency appeared linked with the strength of source used about the tropics. Other studies looking at both the QBO and the semiannual oscillation (SAO) have been undertaken looking at how gravity waves affect these (*Mayr et al.*, 1997, 1998a,b,c). For all of the experiments done for this work only those simulations running with an equatorial source strength of about $\sigma_h = 4.0\ \mathrm{m^2\,s^{-2}}$ have been able to reproduce something resembling a QBO. It is also interesting to note that the temperature variances quoted by *Allen and Vincent* (1995) about tropical latitudes, correspond to these source strengths.

There is doubt about how significant the differences seen in chapter 7 are. Ordinarily, one would compare such differences with variability within a given simulation - as shown by plots of standard deviation. However, inclusion and comparison with such data as compiled from simulations run for just six model years, raises more questions than they answer. Such are useful for identifying higher frequency differences which may be lost or difficult to interpret within monthly averages. Furthermore, during two of the seasons studied (January - during winter, and April) there exist changes in the atmospheric state which will most likely blur any interpretation of differences seen in source strength. Sudden and final warmings are such examples and occur during these times. All the circulation differences quoted so far can be explained simply by, as stated, larger gravity wave breaking or breaking occurring lower down. It is doubtful whether these changes would disappear in longer runs and so any question about the origin of these differences becomes moot.

Finally, in chapter 8 it was seen just how limiting offline testing can be. It was concluded in the offline testing of the three parameterisations that there appeared to be little difference between the MK95 and DSP schemes. However, on inclusion into the SMM, there were remarkable differences. It appeared that the MK95 simulation running with a global source strength of $\sigma_h = 4.0\ \mathrm{m^2\,s^{-2}}$ looked very similar to the DSP one running at a quarter the strength. They shared many of the climatological features, prompting the suggestion that one could get comparable results by introducing another adjustable parameter to smooth over the differences. Doing this obscures the origins of these differences - those being the nonlinear interaction between the waves, which is modelled differently in the schemes, produces a positive feedback in the model. The drag

output from the SMM using the USSP was insufficient to run stable integrations. For any credible parameterisation to be used in the future, there must be consistency in results using similar sources.

As stated in chapter 7, future work must address the issue of a better, more accurate global source. It has been found that using a geographically varying source of parameterised gravity-waves one can model a more representative atmospheric state which cannot be achieved from using a constant source. Thus modellers should seriously consider employing such a geographically varying source if they wish to model a QBO in the tropics while maintaining a credible extratroical state. Although studied indirectly here (refer to section 7.2.3), introducing anisotropies into the gravity wave spectrum at the source height should be undertaken. Sensitivity of southern polar temperatures during winter to increases in gravity wave forcing should encourage investigation using models employing more sophisticated ozone parameterisations - do these sensitivities result in significant changes in ozone concentration? Furthermore, credible parameterisations must reproduce similar modelled responses. Also, not only should different schemes give more consistent results, one must also look at the differences arising from different atmospheric models, running with the same gravity wave schemes. This will be more difficult to evaluate, as there is more scope for differences to occur. However, there is only the one atmosphere and to reproduce and understand the temporal and geographic characteristics of it should be the goal of all.

Appendix A

Definition of Symbols

u	zonal wind
v	meridional wind
w	vertical wind
N	Brunt-Väsäillä frequency
ρ	atmospheric density
ϕ	latitude
λ	longitude
Φ	geopotential
Ω	angular frequency of rotation of the Earth
f	Coriolis parameter, $2\Omega \sin \phi$
$\frac{D}{Dt}$	advective or total derivative, $D/Dt = \partial/\partial t + u\partial/\partial x + v\partial/\partial y + w\partial/\partial z$
a	radius of earth
R	gas constant
c_p, c_v	heat capacity at constant pressure and volume, respectively
H	scale height
T	absolute temperature
p	pressure
θ	potential temperature
Γ	atmospheric temperature lapse rate $(\partial T/\partial z)$
Γ_d	adiabatic lapse rate (g/C_p)
q	heat energy
ζ	vorticity
σ	isentropic density, $-\frac{\partial p}{g\partial\theta}$
β	meridional gradient of Coriolis parameter (β-plane approximation)

SI units are used throughout unless otherwise stated.

Appendix B

Derivation of Gravity-Wave Dispersion Relation

One of the solutions to the set of primitive equations are internal gravity waves. However, a number of assumptions must go into such a derivation. As such, the solution must only be viewed as an idealisation and does not hold under some conditions.

Consider three of the primitive equations (2.1, 2.4, 2.5), and linearise about some mean state, thus;

$$\zeta = \bar{\zeta} + \zeta' \tag{B.1}$$

Assume also the Boussinesq approximation whereby only those density perturbations associated with buoyancy effects are maintained (the 'nearly incompressible' approximation). Consider only two-dimensional flow (x-z directions) and a background state being hydrostatic 2.3, isothermal and in uniform horizontal motion. From this, the primitive equations take the form;

$$\frac{Du'}{Dt} + \frac{\partial \Phi'}{\partial x} = 0, \tag{B.2}$$

$$\frac{D}{Dt}\frac{\partial \Phi'}{\partial z} + N^2 w' = 0, \tag{B.3}$$

$$\frac{\partial u'}{\partial x} + \frac{\partial w'}{\partial z}. \tag{B.4}$$

All primed quantities are perturbations about some mean state. Variable definitions can be found in A. Furthermore, assume each of the perturbed parameters have wave-like solutions of the form,

$$u', \phi', w' = \left(\hat{u}, \hat{\Phi}, \hat{w}\right)(z) Re(\exp i(kx - \omega t)). \tag{B.5}$$

Substituting these into the previous linearised primitive equations yields,

$$-\omega \hat{u} + k\bar{u}\hat{u} + k\hat{\Phi} = 0 \tag{B.6}$$

$$\omega \hat{\Phi}_z - \bar{u}k\hat{\Phi}_z + iN^2\hat{\omega} = 0 \tag{B.7}$$

$$ik\hat{u} + \hat{\omega}_z = 0, \tag{B.8}$$

where,for notational convenience, the subscripted notation represents a partial derivative. Now, rearranging B.8 for $\hat{u}$ and substituting into B.6 gives,

$$-i\frac{\hat{w}_z}{k}(k\bar{u} - \omega) + k\hat{\Phi} = 0. \tag{B.9}$$

Finally, $\partial/\partial z$(B.9) will allow an elimination of the second of the original three variables, ϕ,

$$-i\frac{\hat{w}_{zz}}{k}(k\bar{u} - \omega) + k\hat{\Phi}_z = 0, \tag{B.10}$$

via the substitution of B.6 rearranged for $\hat{\Phi}_z$ and put into B.9, yielding the wave equation,

$$\hat{w}_{zz} - \left(\frac{N}{\bar{u} - c}\right)\hat{w} = 0, \qquad c \equiv \omega/k. \tag{B.11}$$

A dispersion relation for the preceding wave-equation can be got by defining the vertical wavenumber, m by,

$$m^2 \equiv \frac{N^2}{(\bar{u} - c)^2} \Rightarrow \frac{m}{k} = \frac{N}{\tilde{\omega}}. \tag{B.12}$$

This defines the intrinsic frequency of the monochromatic gravity-wave, $\tilde{\omega}$. If this frequency should ever tend to zero, then it is implied (by the singularity in the equation) that this theory should be superseded by another one. It is thought that the diminution of the waves' vertical scale causes critical layer processes to be important and so promote wave saturation and subsequent obliteration. One could have assumed an exponential increase in the perturbed quantities with height (as density falls the amplitude of the parameter perturbations must increase to conserve wave action). Doing this in the foregoing theory admits an unbounded increase in wave amplitude (via an exponential term). This, again, serves as a warning to the preceding theory. Other physics is thought to limit further wave growth.

Appendix C

Response of the USSP to an Isothermal, Windless Atmosphere

To investigate the role processes other than Doppler shifting have on the evolution of spectra in the USSP, it is instructive to remove the effects from the background wind entirely. Also, to make the analysis more straightforward it is helpful to also exclude the effects of a varying temperature profile, thus quantities like static stability will also be constant with height.

In the DSP (section 4.4), conservative spectral evolution is handled by Doppler shifting the spectrum of waves from one height to another depending on local values for the background wind and static stability (refer equation 4.27). At different heights, a given part of the spectrum may change in vertical wavenumber, m, so a change of coordinates via a Jacobian is needed to map the spectrum from one height to another. However, under the approximation of an isothermal, windless atmosphere, the Jacobian disappears - any given spectral component maps onto itself.

In modelling spectral dissipation, the imposed saturation curve (equation 4.28) at a particular height, simply replaces those parts of the initial spectrum (equation 4.25) which have values greater than it. In this study, only the low-m part of the initial spectrum was retained, thus there was a high wavenumber cutoff, m_x which was made equal to m_{1x11} (figure 4.6). With increased height, the imposed saturation curve grows smaller as density decreases, this has the effect of lowering the value of m_x. Exactly how this changes its form can be easily determined by equating the second term of equation 4.25 to the saturation curve at some height, z. Solving for the wavenumber $m = m_x$, gives,

$$m_x(z) = m_{1x11}\frac{\rho_z}{\rho_1}^{1/4}. \tag{C.1}$$

In this, the normalisation factor, D is cancelled as it is a constant under these special conditions (normally a function of static stability) and the standard values for s and t were used.

The amount of momentum flux retained in the spectrum can be found by integrating (with respect to vertical wavenumber) the second term in equation 4.25 between the limits of 0 (no low wavenumber cutoff, m_{1cut}, taken for simplicity) and $m = m_x$. Then adding

to this the contribution from the imposed saturation curve, integrating between $m = m_x$ and m_{1x11}. This yields, after some manipulation,

$$\frac{2\rho_z F(z)}{\beta D} = 2(\rho_1 \rho_z)^{1/2} - \rho_z. \tag{C.2}$$

Although this expression has units of density, its vertical structure is the same as momentum flux, $\rho_z F(z)$. It is this second expression which represents the amount of spectral momentum flux retained in the spectrum at some arbitrary height, z. The two right-hand terms are exponential in nature - density decreases exponentially with height. The second term decreases more rapidly than the first and so becomes negligible after a few scale heights. Neglecting this term one can see how rapidly the function is decreasing by taking the natural log and rearranging. Doing so gives,

$$z = B - 2H \ln(\rho_z F(z)), \tag{C.3}$$

where the functional form $\rho = \exp(-z/H)$ was used for density and H represents scale height. One now has an expression for the evolution of spectral momentum flux under these special conditions. Comparing the vertical evolution of momentum flux of the USSP

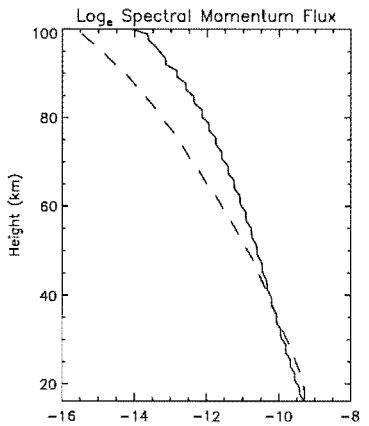

Figure C.1: The natural log of total spectral momentum flux for two of the schemes in an isothermal, windless model atmosphere; The DSP (solid) and the USSP(dotted).

scheme to that from the DSP one notices a greater loss rate of spectral momentum flux for the USSP. Furthermore, the loss rate seen for the USSP is in line with equation C.3. It is reasonable to assume that such an effect will persist to some extent when wind and temperature are allowed to vary with height. Thus, the schemes will have available significantly different amounts of momentum flux to impart on the background flow at a particular height, even though they may introduce the same source from below.

Appendix D

Climatological Wind and Temperature Data

The following are mean climatological wind and temperature data from the UKMO assimilated and CIRA86 datasets. The former were averaged over the years 1992-1997.

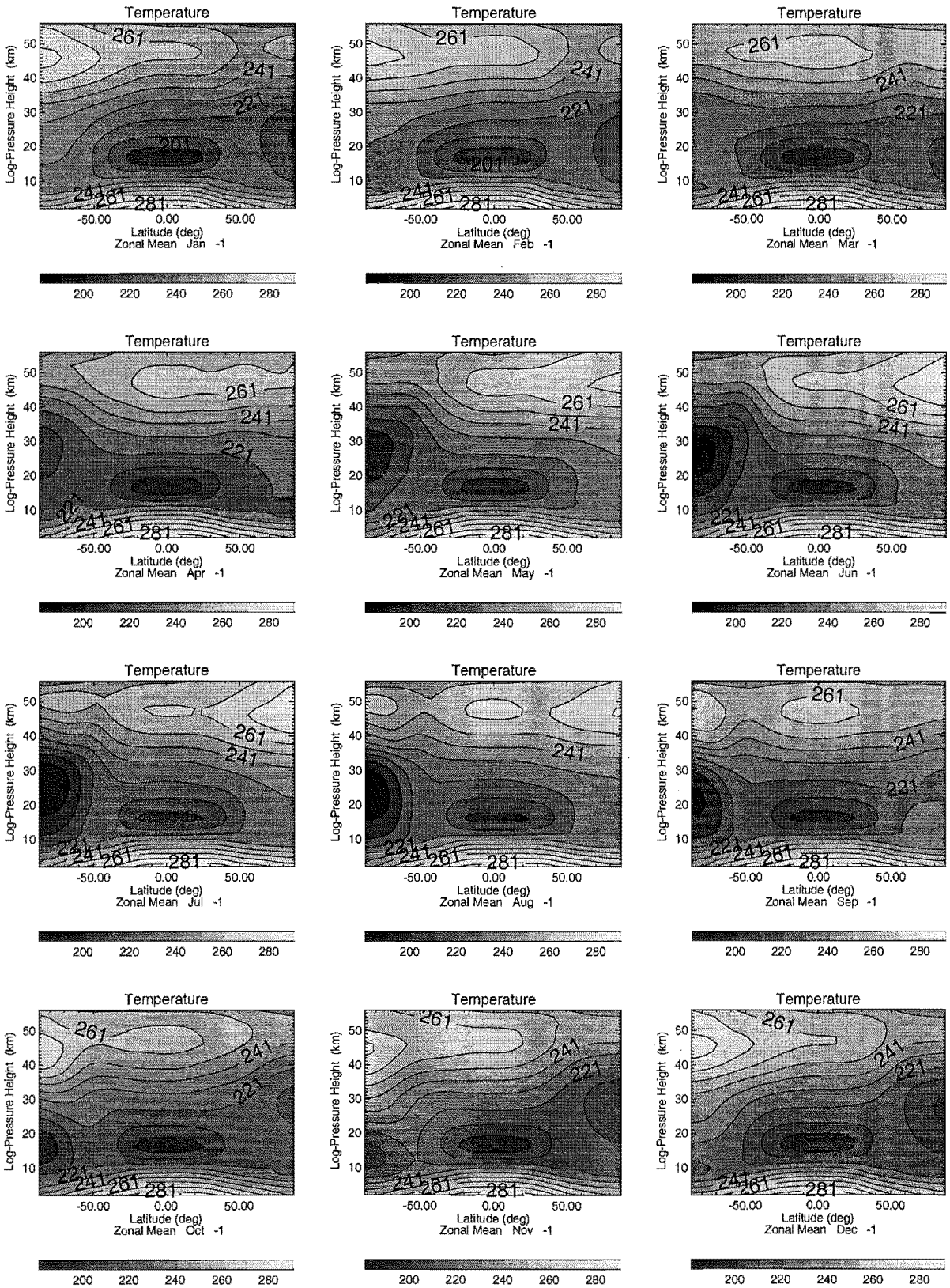

Figure D.1: Zonal-mean values of temperature averaged over 1992-1997, from the UKMO assimilated dataset.

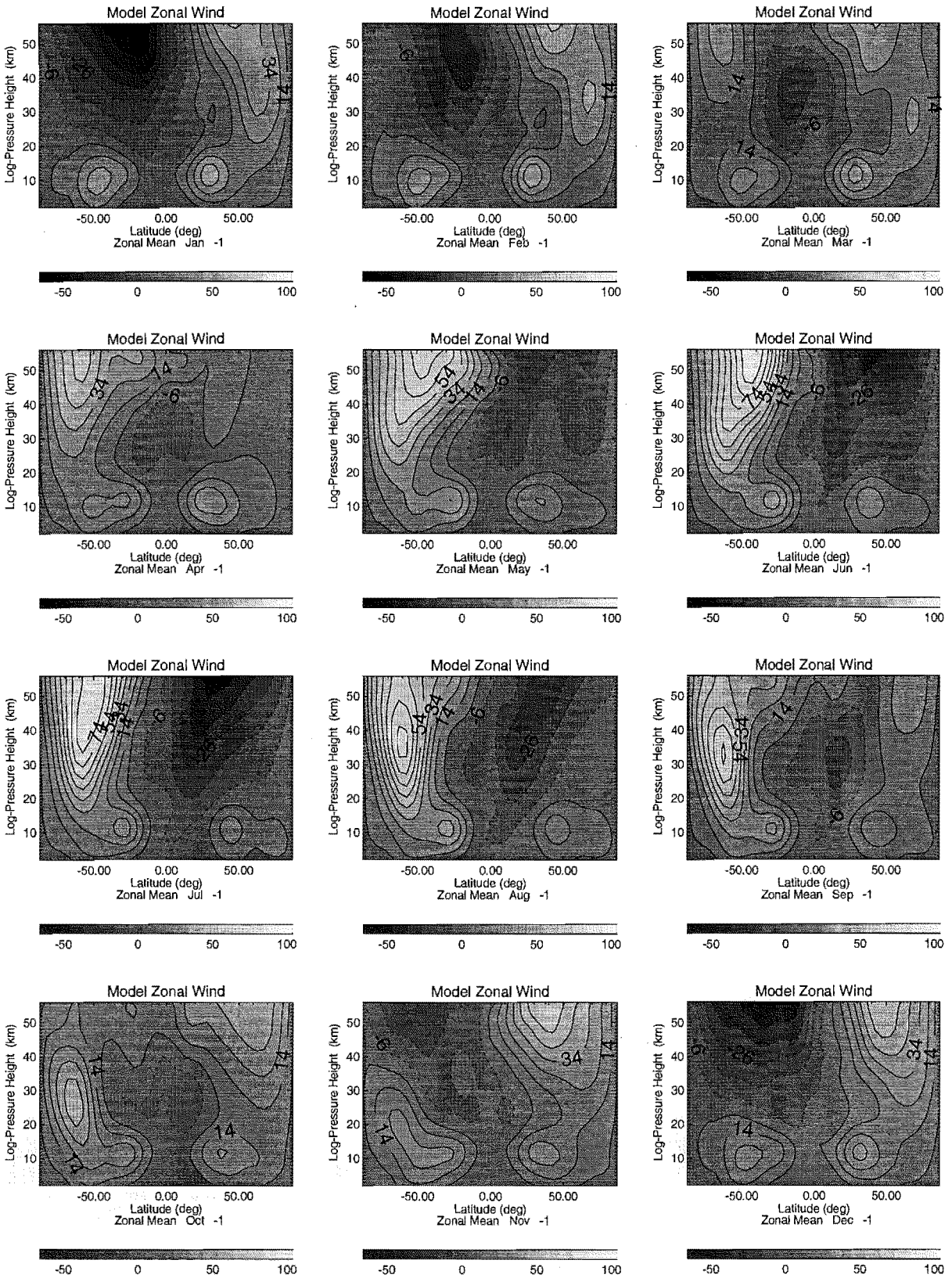

Figure D.2: Zonal-mean values of zonal wind averaged over 1992-1997, from the UKMO assimilated dataset.

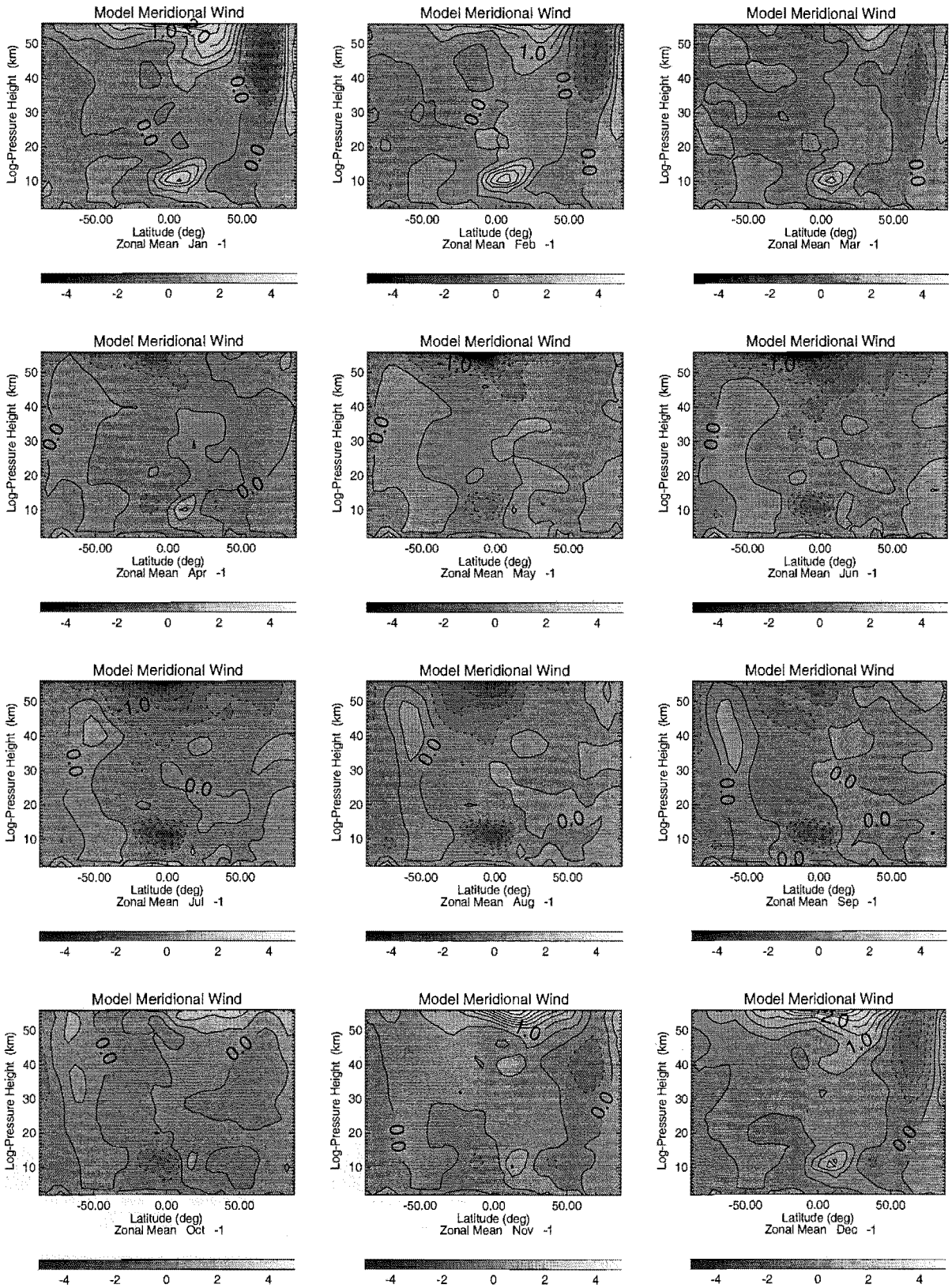

Figure D.3: Zonal-mean values of meridional wind averaged over 1992-1997, from the UKMO assimilated dataset.

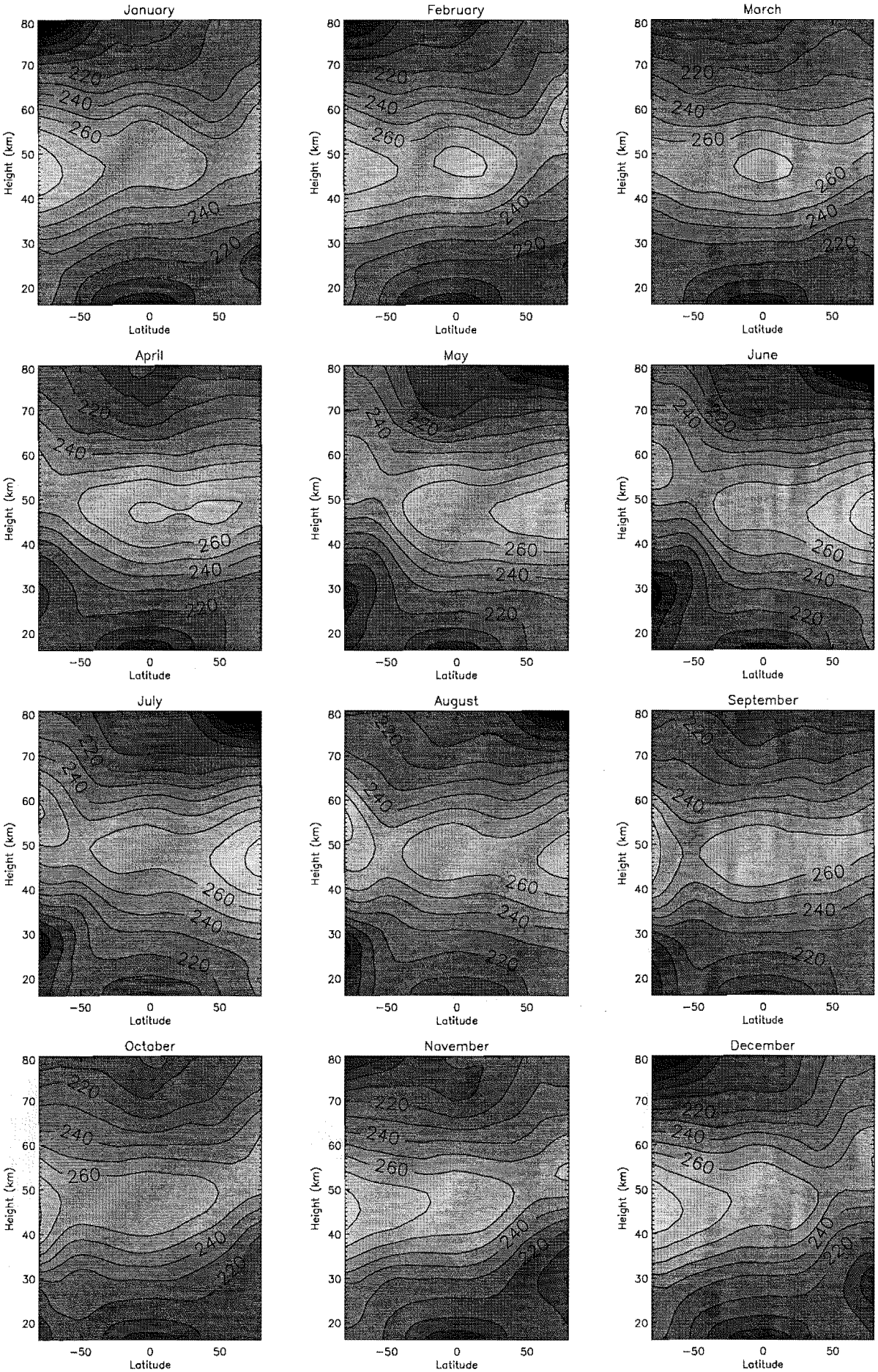

Figure D.4: Zonal-mean values of temperature averaged over 1986-1990, from the CIRA dataset.

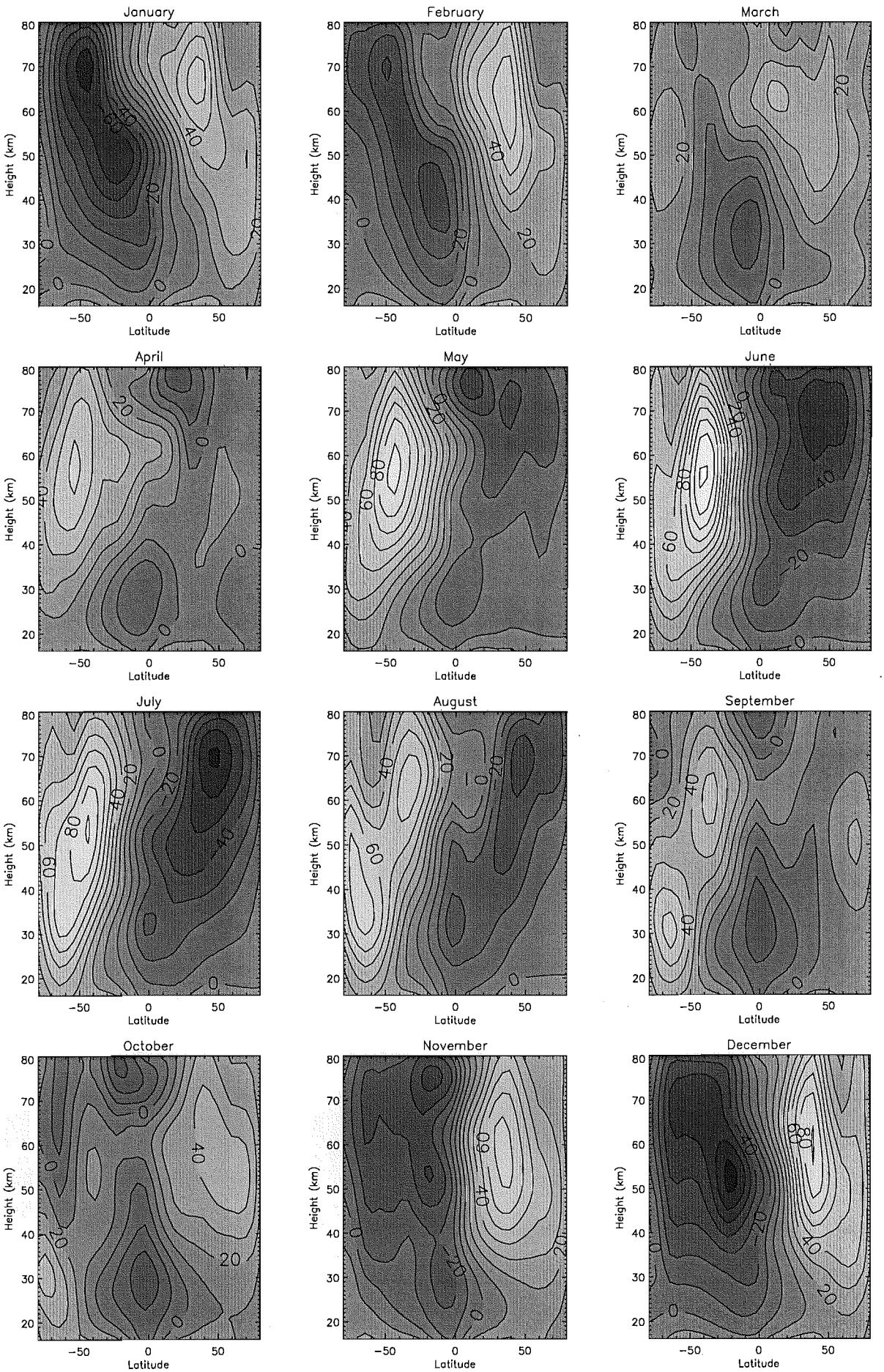

Figure D.5: Zonal-mean values of zonal wind averaged over 1986-1990, from the CIRA86 dataset.

References

Alexander, M., Interpretations of observed climatological patterns in stratospheric gravity wave variance, *J. Geophys. Res.*, *103*(D8), 8627–8640, 1998.

Alexander, M., and K. Rosenlof, Nonstationary gravity wave forcing of the stratospheric zonal mean wind, *J. Geophys. Res.*, *101*(D18), 23465–23474, 1996.

Allen, S. J., and R. A. Vincent, Gravity wave activity in the lower atmosphere: Seasonal and latitudinal variations, *J. Geophys. Res.*, *100*(D1), 1327–1350, 1995.

Andrews, D. G., J. R. Holton, and C. B. Leovy, *Middle Atmosphere Dynamics*, vol. 40 of *International Geophysics Series*. Academic Press Inc. Ltd, London, 1st edn., 1987.

Arakawa, A., and V. Lamb, *Methods in Computational Physics*, vol. 17. Academic Press, 1977.

Bacmeister, J. T., Mountain-wave Drag in the Stratosphere and Mesosphere Inferred from Observed Winds and a Simple Mountain-Wave Parameterization Scheme, *J. Atmos. Sci.*, *50*(3), 377–399, 1993.

Bacmeister, J. T., P. A. Newman, B. L. Gary, and K. R. Chan, An Algorithm for forecasting mountain wave-related turbulence in the stratosphere, *Wea. Forec.*, *9*, 241–253, 1994.

Bossuet, C., M. Deque, and D. Cariolle, Impact of a simple parameterization of convective gravity-wave drag in a stratosphere-troposphere general circulation model and its sensitivity to vertical resolution, *Ann. Geophys.*, *16*, 238,249, 1998.

Butchart, N., S. Clough, T. Palmer, and P. Trevelyan, Simulations of an observed stratospheric warming with quasigeostrophic refractive index as a model diagnostic, *Q. J. R. Meteorol. Soc.*, *108*(457), 475–502, 1982.

Charney, J., and P. Drazin, Propagation of planetary-scale disturbances from the lower into the upper atmosphere., *J. Geophys. Res.*, *66*, 83–109, 1961.

Chun, H.-Y., and J.-J. Baik, Momentum flux by thermally induced internal gravity waves and its approximation for large-scale models, *J. Atmos. Sci.*, *55*, 3299–3310, 1998.

Dewan, E., and R. Good, Saturation and the "universal" spectrum for vertical profiles of horizontal scalar winds in the atmosphere., *J. Geophys. Res.*, *91*, 2742–2748, 1986.

Eliassen, A., and E. Palm, On the transfer of energy in stationary mountain waves, *Geofys. Publ.*, *22*(3), 1–23, 1961.

Fels, S., Radiative-dynamical interactions in the middle atmosphere., *Adv. Geophys.*, *28*, 277–300, 1985.

Fetzer, E. J., and J. C. Gille, Gravity wave variance in LIMS temperatures. part ii: Comparison with the zonal-mean momentum balance, *J. Atmos. Sci.*, *53*(3), 398–410, 1996.

Fleming, E., S. Chandra, J. Barnett, and M. Corey, Zonal mean temperature, pressure, zonal wind and geopotential height as functions of latitude., *Adv. Space Res.*, *10*(12), 11–59, 1990.

Fritts, D. C., A review of gravity wave saturation processes, effects and variability in the middle atmosphere, *Pure Appl. Geophys.*, *130*(2), 343–371, 1989.

Fritts, D. C., and H.-G. Chou, An investigation of the vertical wavenymber and frequency spectra of gravity wave motions in the lower stratosphere, *J. Atmos. Sci.*, *44*(24), 3610–3624, 1987.

Fritts, D. C., and W. Lu, Spectral estimates of gravity wave energy and momentum fluxes. part ii: Parameterization of wave forcing and variability, *J. Atmos. Sci.*, *50*, 3695–3713, 1993.

Fritts, D. C., and T. E. VanZandt, Spectral estimates of gravity wave energy and momentum fluxes. part i: Energy dissipation, acceleration and constraints, *J. Atmos. Sci.*, *50*(22), 3685–3694, 1993.

Gardner, C., Testing theories of atmospheric gravity wave saturation and dissipation, *J. Atmos. Terr. Phys.*, pp. 1575–89, 1996.

Gardner, C. S., Reply to Hines' comments on "Testing theories of atmospheric gravity wave saturation and dissipation", *J. Atmos. Sol. Terr. Phys.*, *60*, 663–665, 1998.

Gregory, D., G. Shutts, and J. Mitchell, A new gravity-wave scheme incorporating anisotropic orography and low-level wave breaking: Impact upon the climate of the UK Meteorological Office Unified Model, *Q. J. R. Meteorol. Soc.*, *124*, 463–493, 1998.

Hamilton, K., R. Wilson, J. Mahlman, and L. Umscheid., Climatology of the GFDL SKYHI troposphere-stratosphere-mesosphere general circulation model., *J. Atmos. Sci.*, *52*, 5–43, 1995.

Harris, T., and R. Vincent, The quasi-two-day wave observed in the equatorial middle atmosphere, *J. Geophys. Res.*, *98*, 10481–10490, 1993.

Haynes, P., C. Marks, M. McIntyre, T. Shepherd, and K. Shine, On the downward control of extratropical diabatic circulations by eddy-induced mean zonal forces, *J. Atmos. Sci.*, *48*(4), 651–678, 1991.

Hines, C., Comments on the paper by C.S.gardner, "Testing theories of atmospheric gravity wave saturation and dissipation", *J. Atmos. Sol. Terr. Phys.*, *60*, 655–662, 1998.

Hines, C. O., A Modeling of Atmospheric Gravity Waves and Wave Drag Generated by Isotropic and Anisotropic Terrain, *J. Atmos. Sci.*, *45*(2), 309–322, 1988.

Hines, C. O., The saturation of gravity waves in the middle atmosphere. part i: Critique of linear-instability theory, *J. Atmos. Sci.*, *48*(11), 1348–1359, 1991a.

Hines, C. O., The saturation of gravity waves in the middle atmosphere. part ii: Development of doppler-spread theory, *J. Atmos. Sci.*, *48*(11), 1360–1379, 1991b.

Hines, C. O., The saturation of gravity waves in the middle atmosphere. part iii: Formation of the turbopause and of turbulent layers beneath it, *J. Atmos. Sci.*, *48*(11), 1380–1385, 1991c.

Hines, C. O., The saturation of gravity waves in the middle atmosphere. part iv: Cutoff of the incident wave spectrum, *J. Atmos. Sci.*, *50*(18), 3045–3060, 1993.

Hines, C. O., Doppler-spread parameterization of gravity-wave momentum deposition in the middle atmosphere. part i: Basic formulation, *J. Atmos. Sol. Terr. Phys.*, *59*(4), 371–386, 1997a.

Hines, C. O., Doppler-spread parameterization of gravity-wave momentum deposition in the middle atmosphere. part ii: Broad and quasi monochromatic spectra, and implementation, *J. Atmos. Sol. Terr. Phys.*, *59*(4), 387–400, 1997b.

Holton, J. R., The generation of mesospheric planetary waves by zonally asymmetric gravity wave breaking, *J. Atmos. Sci.*, *41*(23), 3427–3430, 1984.

Holton, J. R., *An Introduction to Dynamic Meteorology*, vol. 48 of *International Geophysics Series*. Academic Press, London, 3 edn., 1992.

Lawrence, B. N., Some aspects of the sensitivity of stratospheric climate to model lid height, *J. Geophys. Res.*, *102*(D20), 23805–23811, 1997.

Lawrence, B. N., A gravity wave induced quasi-biennial oscillation in a three dimensional mechanistic model, *Q. J. R. Meteorol. Soc.*, *127*, 2005–2021, 2001.

Leovy, C., Simple models of thermally driven mesospheric circulation, *J. Atmos. Sci.*, *21*, 327–341, 1964.

Lin, B., The behaviour of winter stationary planetary waves forced by topography and diabatic heating, *J. Atmos. Sci.*, *39*, 1206–1226, 1982.

Lindzen, R., Turbulence and stress owing to gravity wave and tidal breakdown, *J. Geophys. Res.*, *86*(C10), 9707–9714, 1981.

Manzini, E., and N. McFarlane, The effect of varying the source spectrum of a gravity wave parameterization in a middle atmosphere general circulation model, *J. Geophys. Res.*, *103*(D24), 31523–31539, 1998.

Matsuno, T., Vertical propagation of stationary planetary waves in the winter northern hemisphere, *J. Atmos. Sci.*, *27*, 871–883, 1970.

Mayr, H., J. Mengel, C. Hines, K. Chan, N. Arnold, C. Reddy, and H. Porter, The gravity wave doppler theory applied in a numerical spectral model of the middle atmosphere 2. equatorial oscillations, *J. Geophys. Res.*, *102*(D22), 26093–26105, 1997.

Mayr, H., J. Mengel, and K. Chan, Equatorial oscillations maintained by gravity waves as described with the doppler spread parameterization: I. numerical experiments, *J. Atmos. Sol. Terr. Phys.*, *60*(2), 181–199, 1998a.

Mayr, H., R. Hartle, and K. Chan, Equatorial oscillations maintained by gravity waves as described with the doppler spread parameterization: Ii. heuristic analysis, *J. Atmos. Sol. Terr. Phys.*, *60*(2), 201–213, 1998b.

Mayr, H., J. Mengel, C. Reddy, K. Chan, and H. Porter, Variability of the equatorial oscillations induced by gravity wave filtering, *Geophys. Res. Lett.*, *25*(14), 2629–2632, 1998c.

McFarlane, N., The effect of orographically excited gravity wave drag on the general circulation of the lower stratosphere and troposphere, *J. Atmos. Sci.*, *44*(14), 1775–1880, 1987.

Medvedev, A., and G. Klaassen, Vertical evolution of gravity wave spectra and the parameterization of associated wave drag, *J. Geophys. Res.*, *100*(D12), 25841–25853, 1995.

Norton, W., and J. Thuburn, The two-day wave in a middle atmosphere GCM, *J. Geophys. Res.*, *23*, 2113–2116, 1996.

Osprey, S., and B. Lawrence, A possible mechanism for in situ forcing of planetary waves in the summer extratropical mesosphere., *Geophys. Res. Lett.*, *28*(7), 1183–1186, 2001.

Palmer, T., G. Shutts, and R. Swinbank, Alleviation of a systematic westerly bias in general circulation and numerical weather prediction models through an orographic gravity drag parameterization, *Q. J. R. Meteorol. Soc.*, *112*, 1001–1039, 1986.

Pierrehumbert, R., An essay on the parameterization of orographic gravity wave drag., in *ECMWF Seminar/Workshop Report: Observation, Theory and modelling of Orographic Effects.*, pp. 251–282. 1987.

Randal, W., Observations of the two-day wave in the NMC stratospheric analysis, *J. Atmos. Sci.*, *51*, 306–313, 1994.

Randel, W., The seasonal evolution of planetary waves in the southern hemisphere stratosphere and troposphere., *Q. J. R. Meteorol. Soc.*, *114*, 1385–1409, 1988.

Schoeberl, M., and M. Geller, A calculation of the structure of stationary planetary waves in winter, *J. Atmos. Sci.*, *34*, 1235–1255, 1977.

Shapiro, R., Smoothing, filtering and boundary effects., *Rev. Space Physics*, *8*, 359–387, 1970.

Shapiro, R., The use of linear filtering as a parameterization of atmospheric diffusion., *J. Atmos. Sci.*, *28*, 523–531, 1971.

Shine, K., Midrad: a middle atmosphere radiation scheme., Tech. rep., Department of Atmospheric, Oceanic and Planetary Physics, University of Oxford, Clarendon Laboratory, Parks Road, Oxford, UK, 1988.

Slingo, J., M. Blackburn, A. Betts, R. Brugge, K. Hodges, B. Hoskins, M. Miller, L. Steenman-Clark, and J. Thuburn, Mean climate and transience in the tropics of the ugamp gcm: Sensitivity to convective parametrization., *Q. J. R. Meteorol. Soc.*, *120*, 881–922, 1994.

Smith, A. K., Longitudinal variations in mesospheric winds: Evidence for gravity wave filtering by planetary waves, *J. Atmos. Sci.*, *53*(8), 1156–1173, 1996.

Smith, A. K., Stationary planetary waves in upper mesospheric winds, *J. Atmos. Sci.*, *54*, 2129–2145, 1997.

Smith, S. A., D. C. Fritts, and T. E. VanZandt, Evidence for a saturated spectrum of atmospheric gravity waves, *J. Atmos. Sci.*, *44*(10), 1404–1410, 1987.

Swinbank, R., and A. O'Neill, Stratosphere-troposphere data assimilation system, *Mon. Wea. Rev.*, *122*, 686–702, 1994.

Tsuda, T., T. Inoue, D. Fritts, T. VanZandt, S. Kato, T. Sato, and S. Fukao, Mst radar observations of a saturated gravity wave spectrum, *J. Atmos. Sci.*, *46*(15), 2440–2447, 1989.

Vincent, R., S. Allen, and S. Eckermann, Gravity wave parameters in the lower stratosphere, in *Gravity Wave Processes and Their Parameterization in Global Climate Models.*, edited by K. Hamilton, vol. 50 of *NATO ASI Ser I*, pp. 7–25. 1997.

Wang, D., W.E.Ward, G. Shepherd, and D.-L. Wu, Stationary planetary waves inferred from windii wind data taken within altitudes 90-120 km during 1991-96, *jas*, *57*, 1906–1918, 2000.

Warner, C., and M. McIntyre, An ultra-simple spectral parameterization for non-orographic gravity waves., 1999.

Webster, S., Unified model documentation paper: Gravity wave drag, Tech. Rep. 22, Climate Research Division, Meteorological Office, London Road, Bracknell, Berkshire, UK, 1997.

Weinstock, J., Saturated and unsaturated spectra of gravity waves and scale dependent diffusion., *J. Atmos. Sci.*, *47*, 2211–2225, 1990.

Wu, D., and J. Waters, Gravity wave temperature variances seen by the uars mls, *Geophys. Res. Lett.*, *23*(23), 3289–3292, 1996a.

Wu, D., and J. Waters, Satellite observations of atmospheric variances: A possible indication of gravity waves, *Geophys. Res. Lett.*, *23*(24), 3631–3634, 1996b.